Development of Modeling and Simulation for Magnetic Particle Inspection using Finite Elements

by

Jun-Youl Lee

A thesis submitted to the graduate faculty

in partial fulfillment of the requirements for the degree of

MASTER OF SCIENCE

Major: Electrical and Computer Engineering

Program of Study Committee:

David Jiles, Major Professor
John Bowler
Bulent S. Biner

Iowa State University

Ames, Iowa

2003

Graduate College

Iowa State University

This is to certify that the master dissertation of

Jun-Youl Lee

has met the dissertation requirements of Iowa State University

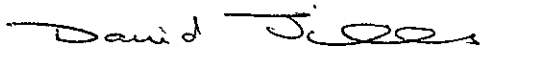

Major Professor

For the Major Program

TABLE OF CONTENTS

LIST OF FIGURES

LIST OF TABLES

ABSTRACT

Magnetic particle inspection (MPI) is a widely used nondestructive inspection method for aerospace applications essentially limited to experiment-based approaches. The analysis of MPI characteristics that affect sensitivity and reliability contributes not only reductions in inspection design cost and time but also improvement of analysis of experimental data. Magnetic particles are easily attracted toward a high magnetic field gradient. Selection of a magnetic field source, which produces a magnetic field gradient large enough to detect a defect in a test sample or component, is an important factor in magnetic particle inspection.

In this work a finite element method (FEM) has been employed for numerical calculation of the MPI simulation technique. The FEM method is known to be suitable for complicated geometries such as defects in samples. This thesis describes the research that is aimed at providing a quantitative scientific basis for magnetic particle inspection. A new FEM solver for MPI simulation has been developed in this research for not only nonlinear reversible permeability materials but also irreversible hysteresis materials that are described by the Jiles-Atherton model. The material is assumed to have isotropic ferromagnetic properties in this research (i.e., the magnetic properties of the material are identical in all directions in a single crystal). In the research, with a direct current field mode, an MPI situation has been simulated to measure the estimated volume of magnetic particles around defect sites before and after removing any external current fields. Currently, this new MPI simulation package is limited to solving problems with the single current source from either a solenoid or an axial directional current rod.

CHAPTER 1.

INTRODUCTION

A number of nondestructive evaluation (NDE) techniques have been developed for evaluating defects, such as surface discontinuities, voids, surface flaws, and cracks on the surface or in the body of materials. Properly applied NDE techniques will prevent operational failures of the mechanical parts by locating critical defects. Metallic materials are widely evaluated in NDE applications due to their common usage in industry. Different NDE techniques should be used depending on whether the metallic materials are magnetic or non-magnetic. For magnetic metallic materials like steel, techniques such as eddy currents [1,2], magnetic flux leakage [3,4], magnetic Barkhausen noise [5,6], and magnetic particle inspection [7,8] can be employed. Among these techniques, the magnetic particle inspection (MPI) and the magnetic flux leakage (MFL) are popular due to their inexpensive and simple procedures. Both techniques depend on the distortion of magnetic flux lines caused by a defect on the surface or sub-surface of a ferromagnetic material. The difference between the techniques is the method of observing this distortion. The MPI technique uses fine magnetic particles, dry iron powder or wet magnetic particles suspended in a liquid medium, to identify the defect while the MFL technique employs a magnetometer to measure the magnetic leakage field occurring around the defect. The indication of magnetic particles on a test sample makes the MPI technique suitable for samples with large surface areas while the MFL technique may be appropriate for detecting defects in the areas where access would be difficult for visualization such as inside surfaces of pipelines.

The magnetic field generator and the magnetic particles are essential components of the MPI method. The magnetic field strength should be large enough to magnetize the sample so that the magnetic particles can interact with the leakage fields. The magnetic force, which drags the magnetic particles to the defect sites, is proportional to the product of the magnetic field and the magnetic field gradient. The distortion of the magnetic field is greatest when the direction of the magnetic field is perpendicular to the plane of a defect, which maximizes the magnitude of the magnetic field gradient. Magnetic fields can be generated

either by a direct contact of current source to the test material using prods, an electromagnet, or by using current coils such as a solenoid or a yoke. The magnetic properties of the magnetic particles are an important factor in MPI testing. A simple analytical model for the calculation of the magnetic leakage field of surface-breaking cracks and an estimation of the magnetic force on the magnetic particle were studied under the assumption of constant permeability [9]. Computational advances enabled the numerical simulations of MPI problems for a complicated geometry [10]. In this thesis we report the use of the finite element method (FEM) with nonlinear and hysteretic magnetization modeling in order to give realistic numerical simulations of MPI for defects with various sizes. The simulated results can provide indications of the expected behavior of magnetic particles around a defect and can therefore be used to devise improved inspection procedures.

1.1. Research Objective

An MPI simulation problem is usually determined by three categories of problem characteristics: i) the definition of permeability functions of test materials, ii) the dimension and coordinate system of a spatial space of a test environment, and iii) source field conditions of either electric current field or permanent magnetostatic field. A new MPI simulation package has been developed for solving the following 12 (=3×2×2) problem categories:

Table 1. Possible MPI problem categories for a new MPI simulation package

Definition of permeability of test materials	Dimension or coordinate of a spatial space	Source current field from either a solenoid or a straight-line coil
Linear (constant permeability)	2-D planar (XY plane)	Magnetostatic (DC mode)
User-defined nonlinear (variable permeability)	Axisymmetric (RZ plane)	Quasi-magnetostatic (AC mode)
Hysteresis (J-A model)		

The following concepts describe how to simulate magnetic particle inspection: (1) spraying magnetic particles over the surface of test objects, (2) for nonlinear permeability materials, making the program compute the magnetic force to pull the magnetic particles against their gravity while the current field exists, and (3) for hysteresis materials, making the program compute the magnetic force needed to retain the magnetic particles after the current field is removed, and computing the demagnetization condition of materials.

The objective of this thesis is to develop a software package for the use of the finite element method (FEM) with nonlinear and hysteretic magnetization modeling in order to give realistic numerical simulations of MPI tests. The simulated results of an MPI test can provide indications of the expected behavior of magnetic particles around a defect and can therefore be used to devise improved inspection procedures. The simulation package can also be applied for both MFL and MPI tests. For purposes of a nondestructive test, one can simulate a test material without any defect to obtain MFL signals or magnetic particle volumes at the beginning, and then simulate the test material with additional artificial defects in order to find the difference of MFL signals or magnetic particle volumes between the situations with and without defects. Therefore, the important issue in NDE applications is to find the relationship between a particular geometry of a defect and the difference of either MFL signals or magnetic particle volumes. This issue is one of the most important objectives in this thesis.

In this thesis, a comparison is made between an output of our MPI simulation package and an analytical formula for its verification. Because of the limited availability of either analytical results or commercial software package concerning hysteresis in materials, it is very difficult to compare these results to any others. The best appropriate validation of these results should be accompanied with the comparison of experimental tests.

1.2. Thesis Organization

Chapter 1 presents the basic introduction of Maxwell's equations, magnetic modeling for simple 2-D planar problems with both magnetostatic and quasi-magnetostatic cases, and finite element modeling for these Maxwell problems. The method for solving 2-D Maxwell

problems using FEM also has been introduced. In general the solution from a 2-D Maxwell problem can support directly the analysis of magnetic flux leakage test. However, there require more modules or processes for a test of magnetic particle inspection. One of the most important objectives of this thesis is to provide these modules and procedures for simpler and easier analysis of MPI. Additionally it is available to provide some sensitivity analysis for an MPI test as a part of NDE applications.

Chapter 2 presents an MPI simulation for a simple geometry like axisymmetric coordinate. A new MPI algorithm is introduced here for any nonlinear permeability materials. Before the introduction of this new algorithm, some verification tests have been preceded for both linear and nonlinear permeability cases. The new MPI algorithm with FEM provided the sensitivity analysis of different sizes of defects on a test material.

Chapter 3 introduces the Jiles-Atherton hysteresis model, and the algorithm of incorporating the hysteresis characteristics with our FEM programming. For the simulation of hysteresis materials, a simple 2-D planar coordinate is employed. Our 2-D hysteresis modeling is currently limited to the case of magnetization that is parallel to its magnetic field intensity. Suppose a 180° domain-wall area between two domains did not align parallel and anti-parallel to a magnetic field, but the angle between this domain wall and the magnetic field is deterministic. Then, the recently implemented MPI simulation must be modified some computation modules. Chapter 3 suggests how to extent in this case.

Finally, chapter 4 summarizes all research works and suggests the future works for more realistic modeling of isotropic hysteresis materials. Appendix A shows the symbols and their descriptions defined in this thesis. Appendix B introduces how to build an FEM problem from simple Maxwell's equations. Several publications for NDE applications are attached at Appendix C.

1.3. Magnetic Flux Leakage

Magnetic Flux Leakage (MFL) is used to test magnetically permeability materials such as steels. Due to the relatively high permeability of carbon steel, eddy current penetration is severely limited, and subsurface and far surface defects are usually not

detectable with the method. On the other hand MFL has been used successfully for many years for inspection of high permeability materials in the wire rope, petrochemical, power industries [3,4], and gas transmission pipeline [11].

Abrupt boundary changes due to metal losses or cracks can produce a magnetic flux leakage field that rises above the inside and outside surface of the tube as shown in Figure 1 [11]. Inside the magnetic flux leakage probe head are detection coils, in which a voltage is produced as they pass through a magnetic field. A Hall effect sensor is used to detect changes in the flux density produced by the magnet [9]. Figure 1 shows the device for an MFL test to detect flaws making abrupt wall-thickness changes. However, with damage such as gradual wall-loss or -bulges, a leakage field would not be produced.

The inspection results are in the form of voltage pulses. These are compared to the indications produced by milled notches in a calibration reference standard of the same diameter, wall thickness and alloy composition. The severity of damage is determined by the response as compared to the response of the simulated defects on the calibration reference standard [12]. However, the response caused by natural damage may differ from the response caused by artificial notches and grooves.

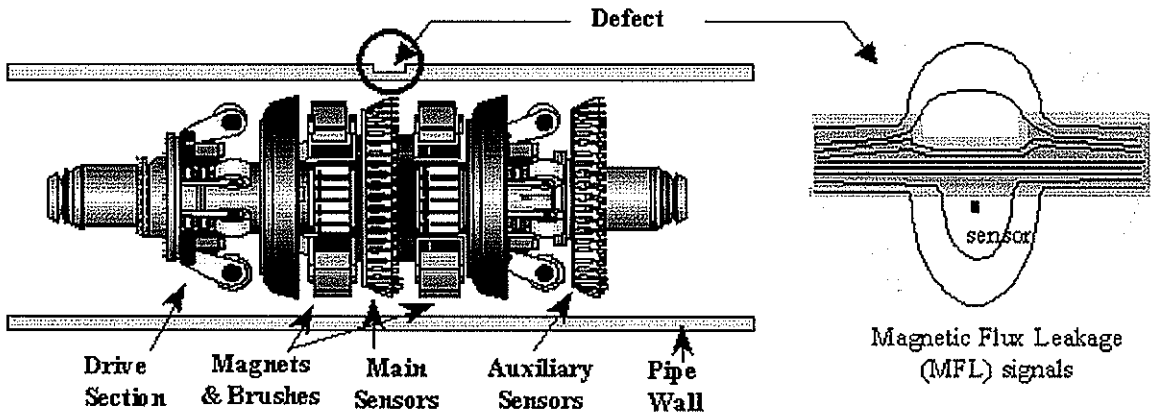

Figure 1. Magnetic Flux Leakage (MFL) Test

1.4. Introduction to Magnetic Particle Inspection

Magnetic Particle Inspection (MPI) is an NDE technique that relies on local or complete magnetization of the component or surface being interrogated [7,8,13]. It can only be applied to ferromagnetic parts. When a crack is present on the surface, then some magnetic flux will leak out from the sides of the crack where the magnetic flux is in a suitable direction. Small magnetic particles, if they are allowed to flow over the magnetized surface, can be attracted to this flux leakage. If it is possible to make them easily detectable by visual inspection, the concentration of particles will enhance the appearance of any cracks. Frequently, the particles are suspended in a liquid medium to enhance fluidity, and in many cases, they are colored to enhance contrast [14].

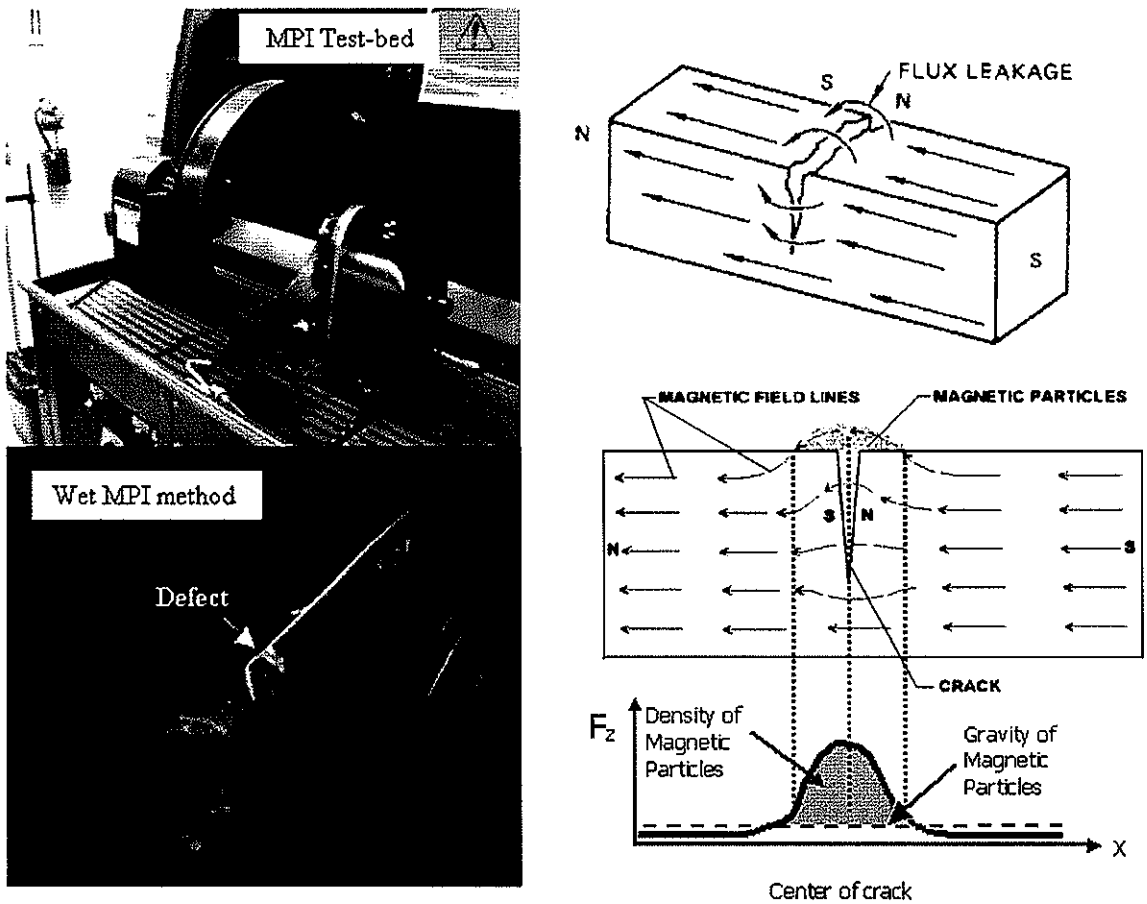

Figure 2. Actual experimental MPI test

For most sensitive applications, fluorescent-coated particles are used, and inspection is carried out under an ultraviolet light. This enhances the detection even more. The integrity of the inspection relies on the operator to induce an adequate magnetic flux in the surface being tested, the lighting conditions, contrast media and orientation of the defects relative to the induced flux. The operator must also inspect the surface to detect any defects.

The technique uses the principle that magnetic lines of force will be distorted by the presence of a flaw in a manner that will reveal its presence. The flaw is located from the flux leakage, following the application of fine magnetic particles, to the area under examination. Surface irregularities and scratches can give misleading indications. Therefore it is necessary to ensure careful preparation of the surface before magnetic particle testing is undertaken.

The set up for an MPI test is shown in Figure 2. After the magnetization of material wet magnetic particles will stick around the crack. Figure 2 shows the cross section of crack area. If the magnetization force is greater than any other force that tries to remove magnetic particles away from the crack, the particles will stick around the crack [9,15,16].

1.5. Maxwell's Equations on Magnetics

The equations of the electromagnetic field can be written as follows [17]:

$$\nabla \times \mathbf{H} = \mathbf{J} + \frac{\partial \mathbf{D}}{\partial t}, \qquad \text{(Ampere's Law)} \qquad (1.1a)$$

$$\nabla \times \mathbf{E} = -\frac{\partial \mathbf{B}}{\partial t}, \qquad \text{(Faraday's Law)} \qquad (1.1b)$$

where **B** is magnetic flux density induction, **E** is electric field intensity, **D** is electric flux density, **J** is current density including induced current field density , and **H** is magnetic field intensity.

Useful alternative Maxwell's point-wise partial differential equations (PDE) are volumetric forms obtained by integrating equations in equations (1.1a) and (1.1b) over space. Applying the "curl" theorem to the resulting integrals of $\nabla \times E$ and $\nabla \times H$ yields the vector integral equations

$$-\int_{\Omega}\frac{\partial \mathbf{B}}{\partial t}d\Omega=\int_{\Sigma}n\times\mathbf{E}d\Sigma,\quad \int_{\Omega}(\frac{\partial \mathbf{D}}{\partial t}+\mathbf{J})d\Omega=\int_{\Sigma}n\times\mathbf{H}d\Sigma \tag{1.2}$$

where Ω is the volume of integration, Σ is its surface, and n is the outward unit normal vector to Σ [18, 19, 20].

To make Maxwell's equations determinate for $\boldsymbol{B}$, $\boldsymbol{E}$, $\boldsymbol{D}$, $\boldsymbol{J}$, and $\boldsymbol{H}$, constitutive relations must be defined. In nearly all cases linear relations are used whereby,

$$\nabla\cdot\mathbf{B}=0, \tag{1.3a}$$

$$\nabla\cdot\mathbf{D}=\rho, \tag{1.3b}$$

$$\mathbf{J}=\sigma\mathbf{E}, \tag{1.3c}$$

$$\mathbf{B}=\mu\mathbf{H}, \tag{1.3d}$$

$$\mathbf{D}=\varepsilon\mathbf{E}, \tag{1.3e}$$

where the parameters μ, ε, ρ, and σ are *magnetic permeability*, *dielectric permittivity*, *electric charge density* (or *resistivity*), and *conductivity*, respectively [17]. Use of μ in equation (1.3d) implies linearity, but $\boldsymbol{B}(\boldsymbol{H})$ can be nonlinear, irreversible, etc. Provided the medium is isotropic, these parameters are scalars; otherwise they are tensors [17]. However, the magnetic permeability can be any function of magnetic field intensity. It is also assumed that both μ and ε themselves are time-invariant in comparison to the fields. For nonmagnetic materials permeability μ is essentially equal to its vacuum value, μ_0, everywhere. In this thesis magnetic permeability μ can be a constant, a user-defined nonlinear (or piecewise linear) function, or a hysteresis function defined by a model equation such as the Jiles-Atherton model [21,22]. The electric field from the source coil is usually magnetostatic (DC; direct current mode) or quasi-magnetostatic (Eddy current; AC powered current mode). A further assumption in this thesis is that there is no electric free-charge ($\rho=0$), so that

$$\nabla\cdot\mathbf{D}=0 \tag{1.4a}$$

and

$$\nabla\cdot\mathbf{J}=-\frac{\partial\rho}{\partial t}=0. \tag{1.4b}$$

Consequently,

$$\nabla \cdot \frac{\partial \mathbf{D}}{\partial t} = \nabla \cdot \left(\varepsilon \frac{\partial \mathbf{E}}{\partial t} \right) = 0. \tag{1.4c}$$

Equation (1.4c) implies that the time variance of either **D** or **E** can be neglected at the quasi-magnetostatic steady state. That is,

$$\frac{\partial \mathbf{D}}{\partial t} = \left(\varepsilon \frac{\partial \mathbf{E}}{\partial t} \right) = 0. \tag{1.5}$$

The current MPI simulation package has been developed for either magnetostatic or quasi-magnetostatic mode only. Substituting equations (1.3c) and (1.5) into equation (1.1a) gives

$$\nabla \times \mathbf{H} = \sigma \mathbf{E} \tag{1.6}$$

relating the (approximately time-invariant) electric field to the curl of the magnetic field. Consequently, by substituting equation (1.3d) into equation (1.1b), one of Maxwell's partial differential equations is established as follows:

$$-\frac{1}{\mu} \nabla \times \mathbf{E} = \frac{\partial \mathbf{H}}{\partial t} \tag{1.7}$$

relating the time rate of change of the magnetic field to the curl of the electric field. Since ***E*** is the primary field, unknown variables such as ***H*** may be eliminated between the two curl equations in (1.6) and (1.7) and treated as a secondary or derived quantity. Substituting equation (1.6) into the curl of equation (1.7) gives the second order partial differential equation,

$$-\nabla \times \left(\frac{1}{\mu} \nabla \times \mathbf{E} \right) = \sigma \frac{\partial \mathbf{E}}{\partial t}. \tag{1.8}$$

1.5.1. Magnetostatics

"Magnetostatics" implies that the time rate of magnetic field change is very slow or approximately time-invariant. Therefore, the Maxwell's equations for this steady state case are as follows [20]:

$$\nabla \times \mathbf{E} = 0, \tag{1.9a}$$

$$\nabla \cdot \mathbf{B} = 0, \tag{1.9b}$$

$$\nabla \times \mathbf{H} = \mathbf{J}_s, \tag{1.9c}$$

where J_s is the electric current density from a source coil, and the relationship

$$\mathbf{B} = \mu\mathbf{H} \tag{1.10a}$$

or

$$\mathbf{B} = \mu_0(\mathbf{H} + \mathbf{M}). \tag{1.10b}$$

Equation (1.10a) is used for an approximate expression of any function of $\boldsymbol{B}(\boldsymbol{H})$, and (1.10b) is used for the exact expression of $\boldsymbol{B}(\boldsymbol{H})$ when **M** is known and measurable at any time.

For any differentiable vector **v**, it is always true that [23]

$$\nabla \cdot (\nabla \times \mathbf{v}) = 0. \tag{1.11}$$

Since $\nabla \cdot \mathbf{B} = 0$ under all conditions, there exists a *magnetic vector potential* **A** such that

$$\mathbf{B} = \nabla \times \mathbf{A}, \tag{1.12}$$

so that the differentiable vector **A** meets

$$\nabla \cdot (\nabla \times \mathbf{A}) = 0, \tag{1.13}$$

with the same reason of equation (1.11). Substituting equation (1.10a) and (1.12) to equation (1.9b) gives

$$\nabla \times \left(\frac{1}{\mu} \nabla \times \mathbf{A} \right) = \mathbf{J}_s. \tag{1.14}$$

Similarly, substituting equation (1.10b) and (1.12) to equation (1.9b) gives

$$\nabla \times \left(\frac{1}{\mu_0} \nabla \times \mathbf{A} \right) = \mathbf{J}_s + \nabla \times \mathbf{M}. \tag{1.15}$$

The 2D-planar case assumes that the current flows are parallel to the z-axis, so only the z component of **A** is present,

$$\mathbf{A} = (0,0,A)^{\mathrm{T}},\ \mathbf{J}_s = (0,0,J)^{\mathrm{T}}. \tag{1.16}$$

where $A = A(x,y)$, $J = J(x,y)$, and $\mathbf{v}^{\mathrm{T}}$ means the transpose of the vector **v**, so that vectors **A** and $\mathbf{J}_s$ be column vectors . The (x, y, z) coordinate will be mapping to the (r, z, θ) coordinate (however, the Jacobian transform of the Cartesian coordinate into the rotational coordinate will be required for all partial differential equations). Equation (1.14) can be written as [23]

$$-\nabla\cdot\left(\frac{1}{\mu}\nabla\mathbf{A}\right)+\nabla\left(\frac{1}{\mu}\nabla\cdot\mathbf{A}\right)=\mathbf{J}_s, \tag{1.17}$$

and for this 2D case,

$$\nabla\cdot\mathbf{A}=0. \tag{1.18}$$

Therefore, equations (1.14) or (1.15) can be simplified to a scalar elliptic PDE:

$$-\nabla\cdot\left(\frac{1}{\mu}\nabla A\right)=J \tag{1.19}$$

or

$$-\nabla\cdot\left(\frac{1}{\mu_0}\nabla A\right)=J+\mathbf{k}\cdot(\nabla\times\mathbf{M}) \tag{1.20}$$

where **k** is the unit vector along the z direction, which is the same direction of current flow [19]. From equation (1.16), the magnetization **M** is a function of the vector potential with respect to its own material permeability property. For the case of hysteretic magnetic materials, since the relationship between the magnetization and the magnetic vector potential is nonlinear and irreversible (i.e., there is no one-to-one mapping), the solution for this FEM problem can be only solved by some generic ways (i.e., the solver for hysteresis problems converts unknown continuous solution space to a piecewise-linear space and gradually updates vectors **B**, **H**, and **M** for each finite element by minimizing computational errors). Equation (1.20) will be included in our hysteresis FEM algorithm for an MPI simulation test.

For the 2-D planar case, we can compute the magnetic flux density **B** from (1.12) as

$$\mathbf{B}=\left(\frac{\partial A}{\partial y},\quad -\frac{\partial A}{\partial x},\quad 0\right)^T \tag{1.21}$$

and, assuming

$$\mathbf{H}=(1/\mu)\mathbf{B} \tag{1.22}$$

at a particular position of 2-D planar space (remind we are using an FEM computation. i.e., each finite element has unique values of **B**, **H**, and μ, and it is assumed that the value of μ is constant for each finite element), the magnetic field **H** at the particular position is given by

$$\mathbf{H} = \left(\frac{1}{\mu}\frac{\partial A}{\partial y}, \quad -\frac{1}{\mu}\frac{\partial A}{\partial x}, \quad 0 \right)^T. \tag{1.23}$$

The interface condition across spatial subdomain borders between regions of different material properties is that $\mathbf{H}\times\mathbf{n}$ be continuous [18,19,20]. There are three types of boundary conditions for applying FEM: *Dirichlet* boundary condition, *Neumann* boundary condition, and the *mixed* condition of both cases [18, 20]. More detailed description of these boundary conditions will be presented in the next section, The Dirichlet boundary condition specifies the certain value of the magnetostatic potential A on the boundary. The Neumann condition specifies the value of the normal component of

$$\mathbf{n}\cdot\left(\frac{1}{\mu}\nabla A\right) \tag{1.24}$$

on the boundary. This is equivalent to specifying the tangential value of the magnetic field **H** on the boundary. Visualization of the magnetic vector potential **A**, the magnetic field **H**, and the magnetic flux density **B** is also provided in the MPI simulation package.

1.5.2. Quasi-Magnetostatics (Eddy Current Case)

The MPI test may apply an AC (alternating current) power; e.g., for the purpose of the surface test of an experimental object [18]. Suppose electric and magnetic fields vary harmonically in time with low frequency. Let the time-frequency of a source current field be ω. If the current field is homogenously periodic, then the current density of the source coil is

$$J(t) = \mathrm{Re}\{Je^{j\omega t}\}. \tag{1.24}$$

The conductivity σ of an isotropic material is scalar. The homogenous time-frequency of the electric field generated by this current density field is also assumed as the same as ω in equation (1.3c). From equations (1.1b) and (1.12) it is easily derived that

$$\nabla\times\mathbf{E} = -\frac{\partial\mathbf{B}}{\partial t} = -\frac{\partial\nabla\times\mathbf{A}}{\partial t} = -\frac{\partial\nabla\times\mathrm{Re}\{\overline{\mathbf{A}}e^{j\omega t}\}}{\partial t}, \tag{1.25}$$

where $\overline{\mathbf{A}}$ is the maximum magnitude vector of **A**. Assuming that ∇ and $\partial/\partial t$ operators commute, (1.25) can be rewritten as [23]

$$\nabla\times\left(\mathbf{E}+\frac{\partial\mathbf{A}}{\partial t}\right)=0. \tag{1.26}$$

Because $\nabla\times\nabla\phi=0$ for any scalar ϕ [23], we can define an electrical scalar potential φ such that

$$\mathbf{E}=-\frac{\partial\mathbf{A}}{\partial t}-\nabla\varphi=\omega\mathbf{A}-\nabla\varphi. \tag{1.27}$$

Substituting (1.27) to (1.3c),

$$\mathbf{J}=\sigma(\omega\mathbf{A}-\nabla\varphi)=\omega\sigma\mathbf{A}+\mathbf{J}_s \tag{1.28}$$

where $\mathbf{J}_s=-\sigma\nabla\varphi$ is the current density field in the source coil which of course is simply a restatement of the Ohm's law. Substituting (1.28) to (1.6), we have

$$\nabla\times\mathbf{H}=\mathbf{J}_s+\omega\sigma\mathbf{A}. \tag{1.29}$$

From (1,12), (1.22) and (1.29) finally we have

$$\nabla\times\left(\frac{1}{\mu}\nabla\times\mathbf{A}\right)-\omega\sigma\,\mathbf{A}=\mathbf{J}_s \tag{1.30}$$

at a particular position of 2-D planar or axisymmetric spatial space. By the condition of (1.18) and the corresponding result of (1.17), Equation (1.30) becomes

$$-\nabla\cdot\left(\frac{1}{\mu}\nabla\mathbf{A}\right)-\omega\sigma\,\mathbf{A}=\mathbf{J}_s. \tag{1.31}$$

Suppose an MPI environment is 2-D planar, such that the time-harmonic current field in the source coil is defined as $\mathbf{J_s}$ = (0,0,J) Re{$e^{j\omega t}$}. Then the magnetic vector potential **A** can be defined as

$$\mathbf{A}=(0,0,\overline{A})\,\mathrm{Re}\{e^{j\omega t}\}. \tag{1.32}$$

Then, equation (1.28) can be easily derived as an elliptic PDE equation as following

$$-\nabla\cdot\left(\frac{1}{\mu}\nabla\overline{A}\right)-\omega\sigma\,\overline{A}=J \tag{1.33}$$

or

$$-\nabla\cdot\left(\frac{1}{\mu_0}\nabla\overline{A}\right)-\omega\sigma\,\overline{A}=J+\mathbf{k}\cdot(\nabla\times\mathbf{M}) \tag{1.34}$$

where **k** is the same direction of current flow and **M** is the magnetization, which is a function of the vector potential **A**.

1.5. Finite Element Modeling in Magnetics

Solving Maxwell's electric and magnetic problems at all points in space yields complex and large systems of equations. In general a finite element method approximates an original physics problem by a discrete piecewise linear system. The discrete problem is then solved locally at each time step by summing nodal contributions from nearest neighbors and integrating each node independently using a "leapfrog" scheme. Finite elements are suited to structurally complex models, but increase the floating-point operation count. However, the dominance of finite elements in many scientific fields such as thermal, structures, fluids, and electromagnetics is due to geometric adaptability and modeling ease.

The basic characteristics of finite element modeling (FEM) are as follows:

- Finite Element Analysis is a generic method for simulating a physical system (geometry and loading environment) by a mathematical approximation of the real system.
- The simulated physical system is constructed using discrete interrelated building blocks called "elements".
- The field equations are solved for locations defined by the elements.
- FEM deals with complex boundaries well and gives answers to "real world" structural problems.

Figure 3 shows an example of how to mesh 3-dimensional objects into finite elements. The *Delaunay refinement method* is the most popular ways to guarantee suitable meshes [24,25]. If a finite element generated by a particular mesh generation algorithm has very acute angle between two edges, then the element may result in an inadequate or distorted physical approximation, because any value from physics is assumed to be the same in this element (i.e., the values have been averaged across this element). Since many excellent

commercial mesh generation utilities are currently available, the description of mesh generation will be omitted from this thesis.

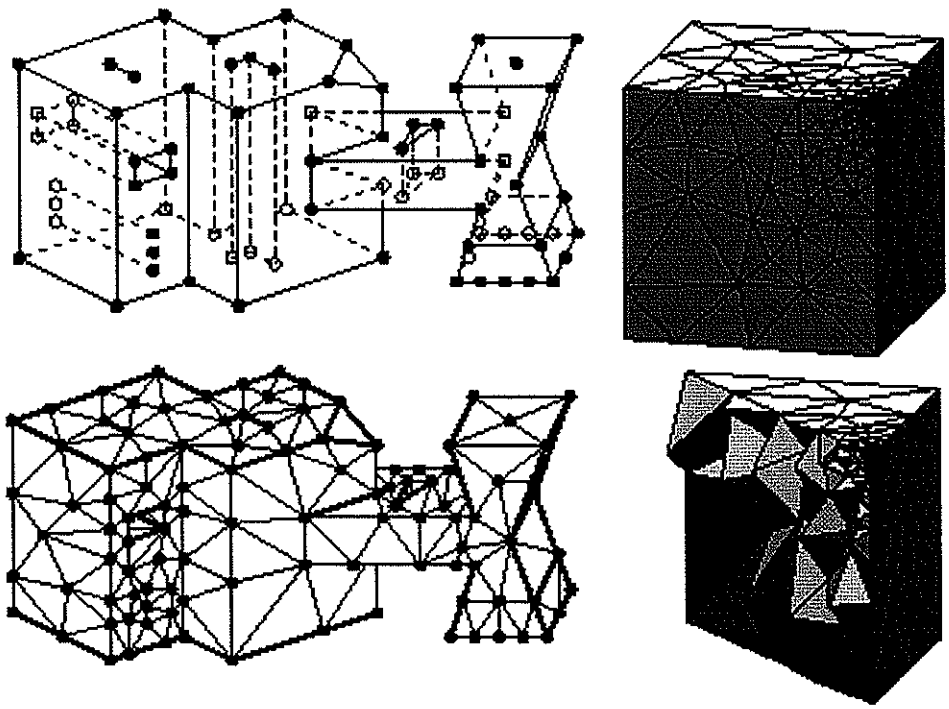

Figure 3. Finite Element Method: Delaunay Refinement Method [25]

1.5.1. Elliptic Partial Derivative Equation (PDE)

The basic equation of the standard scalar elliptic PDE is

$$-\nabla \cdot (s\nabla u) + mu = f \qquad \text{in } \Omega, \tag{1.35}$$

where Ω is a bounded spatial domain [20]. The parameters s, m, and f are given as scalar values, and the unknown variable u are (complex-valued) scalar defined on the spatial domain Ω. A nonlinear solver is also available in our MPI simulation package for the following nonlinear elliptic PDE:

$$-\nabla \cdot (s(u)\nabla u) + m(u)u = f(u), \tag{1.36}$$

where s, m, and f are time-invariant functions of the unknown solution u [20].

The Maxwell's equations for 2-D planar or axisymmetric problems form elliptic PDE models. Very restricted conditions of 3-D Cartesian environment may be able to maintain this elliptic PDE modeling: it depends on whether the equation (1.14) remains true or not. For our MPI simulation environment, the parameter $m(u)$ in equation (1.34) is defined as a scalar constant, but $s(u)$ and $f(u)$ can be nonlinear functions of u. Table 2 shows the relationship between elliptic PDE models and MPI problems supported by our simulation package.

The boundary conditions specify a combination of u and its normal derivative on the boundary [18,19,20]:

- *Dirichlet:* $hu = r$ on the boundary $\partial\Omega$.
- *Neumann:* $\vec{n} \cdot (s\nabla u) = g$ on $\partial\Omega$.
- *Mixed:* A combination of Dirichlet and Neumann, i.e., $\vec{n} \cdot (s\nabla u) + qu = g$ on $\partial\Omega$.

Here, $\vec{n}$ is the outward unit normal vector to the surface. The parameters of boundary conditions (h, r, g, and q) can be constants or functions defined on $\partial\Omega$ (Recall s is the same value as shown in equation (1.33)). Dirichlet conditions are also called essential boundary conditions and restrict the trial space. The most common use of Dirichlet boundary conditions from a magnetic problem is that the magnetic vector potential is defined as zero along a boundary, so that any magnetic flux leakage cannot cross the boundary. It is also known as a closed boundary condition.

Table 2. Relationship between elliptic PDE models and MPI problems

Parameters/Variable of Elliptic PDE Models	Magnetostatics for planar or axisymmetric problems	AC Power Electromagnetics for planar or axisymmetric one
Variable, u	Magnetic vector potential, A	Magnetic vector potential, A
$s(u)$	$1/\mu(\|\nabla A\|)$ or $1/\mu_0$	$1/\mu(\|\nabla A\|)$ or $1/\mu_0$
$m(u)$	0	$j\omega\sigma - \omega^2\varepsilon$ or $j\omega\sigma$
$f(u)$	J or $J + \mathbf{k} \cdot (\nabla \times \mathbf{M})$	J or $J + \mathbf{k} \cdot (\nabla \times \mathbf{M})$

The computational effort to solve an FEM problem is increased by the number of finite elements and mesh vertices. Therefore, the smaller the number of finite element is, the less time-consuming is the computation. There are two ways of reducing the number of finite elements: (1) to use course meshes of test objects, and (2) to reduce the size of a background space. The first case may be not preferable because of its large approximation error. For the second choice with Dirichlet boundary conditions (i.e., the size of a spatial domain space is not relatively big enough to test objects), the solution from the closed boundary condition may yield unrealistic results since the magnetic flux lines around the spatial domain surface could be significantly distorted by these Dirichlet boundary conditions [18,20]. It implies that the internal magnetic flux lines are also influenced by these boundary conditions simultaneously. Therefore, it is required to take a large enough region of the domain space in order that the solution may approximately converge to the real physical result. However, it may require utilization of large computational resources.

Neumann boundary conditions are also called natural conditions and arise as necessary conditions for a solution [18,19,20]. This boundary condition specifies the normal derivative of a vector potential along the boundary. The most common and simple definition of Neumann conditions of a magnetic FEM problem is that $\vec{n} \cdot \nabla A = 0$ along a boundary; i.e., each position at the boundary always keep the direction of magnetic flux leakage to be normal to the boundary. This is in general unrealistic, but this sort of boundary condition is consistent with an interface with extremely high-permeability metals.

The 'mixed' boundary condition is most often used in eddy current problems on interfaces with bodies with small skin-depth eddy currents. The selection of adequate boundary conditions is dependent on the geometric conditions of the source fields, test objects, and the size and shape of a spatial domain space [18,20].

The implementation of FEM can be summarized in the following way: *Project the weak form of the differential equation onto a finite-dimensional function space* [20]. For the weak form of the differential equation, "mixed" boundary conditions are assumed to apply on the whole boundary. In the simple case of a unit matrix h, setting $g = qr$ and then letting yields the Dirichlet condition because division with a very large q cancels the normal

derivative terms. The actual implementation is different, since the above procedure may create conditioning problems.

Assume that u is a solution of the differential equation. Multiply the equation with an arbitrary *test function* v and integrate on Ω [20]:

$$\int_{\Omega}\{-(\nabla\cdot(s\nabla u))v+muv\}dx=\int_{\Omega}fvdx,\ for\ all\ v. \tag{1.37}$$

Then, the partial integration (Green's formula) yields:

$$\int_{\Omega}\{(s\nabla u)\cdot\nabla v+muv\}dx-\int_{\partial\Omega}\vec{n}\cdot(s\nabla u)vds=\int_{\Omega}fvdx,\ for\ all\ v. \tag{1.38}$$

The boundary integral can be replaced by the boundary condition:

$$\int_{\Omega}\{(s\nabla u)\cdot\nabla v+muv\}dx-\int_{\partial\Omega}(-qu+g)vds=\int_{\Omega}fvdx,\ for\ all\ v. \tag{1.39}$$

Replace the original problem with: Find u such that

$$\int_{\Omega}\{(s\nabla u)\cdot\nabla v+muv-fv\}dx-\int_{\partial\Omega}(-qu+g)vds=0,\ for\ all\ v. \tag{1.40}$$

This equation is called the weak form of the differential equation. Obviously, any solution of the differential equation, including these assumed limitations, is a solution of the restricted variant problem family. The reverse is true under some restrictions on the domain and on the coefficient functions.

The solution u and the test functions v belong to some function space V. The next step is to choose an N_p-dimensional V_{N_p}, which is a subset of the global space V. '*Project the weak form of the PDE onto a finite-dimensional function space*' simply means requesting u and v to lie in V_{N_p} rather than V [20]. The solution of the finite dimensional problem turns out to be the element of that lies closest to the weak solution when measured in the energy norm shown in equation (1.40). Convergence is guaranteed if the space V_{N_p} tends to V as $N_p\rightarrow\infty$ [19]. Since the differential operator is linear, we demand that the weak form of equation is satisfied for N_p test-functions $\phi_i\in V_{N_p}$ that form a basis [20], i.e.,

$$\int_{\Omega}\{(s\nabla u)\cdot\nabla\phi_i+mu\phi_i-f\phi_i\}dx-\int_{\partial\Omega}(-qu+g)\phi_i ds=0,\ for\ i=1,2,...,N_p. \tag{1.41}$$

Expand u in the same basis of V_{N_p}

$$u(x) = \sum_{j=1}^{N_p} U_j \phi_j(x), \tag{1.42}$$

and obtain the system of equations [20]

$$\begin{aligned} \sum_{j=1}^{N_p} U_j \left[\int_\Omega \left\{ \left(s \nabla \phi_j \right) \cdot \nabla \phi_i + m \phi_j \phi_i \right\} dx + \int_{\partial\Omega} q \phi_j \phi_i ds \right] \\ = \int_\Omega f \phi_i dx + \int_{\partial\Omega} g \phi_i ds, \; for \; i = 1,2,...,N_p. \end{aligned} \tag{1.43}$$

Use the following notations:

- $K_{ij} = \int_\Omega \left(s \nabla \phi_j \right) \cdot \nabla \phi_i \, dx$ (Stiffness matrix)
- $M_{ij} = \int_\Omega m \phi_j \phi_i dx$ (Mass matrix)
- $Q_{ij} = \int_{\partial\Omega} q \phi_j \phi_i ds$ (Boundary conditions)`
- $F_i = \int_\Omega f \phi_i dx$ (Field sources)
- $G_i = \int_{\partial\Omega} g \phi_i ds$ (Boundary field sources)

Then, equation (1.30) can be rewritten as the system in the form [20]

$$(\mathrm{K} + \mathrm{M} + \mathrm{Q})\ \mathrm{U} = (\mathrm{F} + \mathrm{G}), \tag{1.44}$$

where K, M, and Q are N_p-by-N_p matrices, and F and G are N_p-vectors. For the case of Maxwell' equations (self-adjoint and elliptic PDE problem), the matrix $(K+M+Q)$ becomes symmetric and positive definite, and equation (1.41) is also formulated as a minimization problem. Appendix B describes on how to assembling Maxwell's equations to FEM.

The approximate solution to the elliptic PDE is found in four steps:

1. Describe the geometry of the domain Ω and the boundary conditions.
2. Build triangular (for 2-D problems) or tetrahedral (for 3-D problems) meshes on the spatial domain Ω. A mesh is described by three matrices of fixed format that contains

information about the mesh points, the boundary segments, and the triangles/tetrahedrons.

3. Transform the PDE and the boundary conditions into discrete mesh segments to obtain a linear system $(K + M + Q)\ U = (F + G)$. The unknown vector u contains the values of the approximate solution at the mesh points, the matrix $(K + M + Q)$ is assembled from the coefficients c, a, h, and q and the right-hand side $(F + G)$ contains, essentially, averages of f around each mesh point and contributions from g.
4. Once the matrices $(K + M + Q)$ and $(F + G)$ are assembled, the solver is prepared for solving the linear or nonlinear (even, hysteresis) system and post-processing the solution.

CHAPTER 2.

SENSITIVITY ANALYSIS IN SIMPLE GEOMETRICAL SITUATIONS

2.1. Axisymmetric FEM and its Verification

2.1.1. Verification with a Solenoid Model

There is no general analytic formula for the magnetic field of a cylindrical solenoid at a general point in space. Equation (2.1) gives the strength of the magnetic field on the long, central axis of a solenoid, oriented as shown in Figure 4 [26].

$$H = \left(\frac{N}{L}i\right)\left[\frac{(L+2a)}{2\left\{D^2+(L+2a)^2\right\}^{1/2}} + \frac{(L-2a)}{2\left\{D^2+(L-2a)^2\right\}^{1/2}}\right] \tag{2.1}$$

When considering the center point ($a = 0$), the field is

$$H = \left(\frac{N}{L}i\right)\left[\frac{L}{\left(D^2+L^2\right)^{1/2}}\right] \tag{2.2}$$

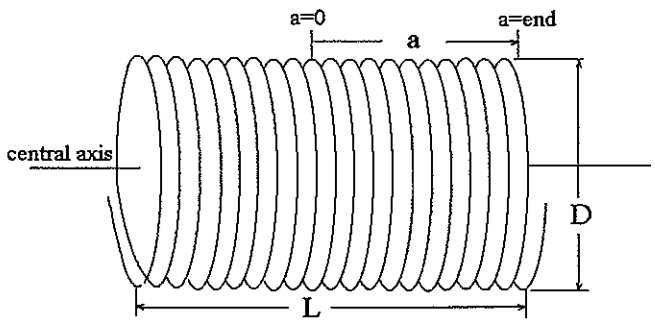

Figure 4. A solenoid with length L, diameter D, number of turns N, and current i

For a long solenoid, where $L>>D$ and $\left(D^2+L^2\right)^{1/2} \approx L$, then

$$H = \frac{N}{L}i = ni, \tag{2.3}$$

where n is the number of turns per unit length (turns/m).

We designed two shapes of solenoids for the verification of the solenoid model with the same current field conditions: i=1.00 A and N=1000 turns. We have

(a) a solenoid with D=2.54 cm, L=12.7 cm (L >> D), and

(b) a solenoid with D=12.0 cm, L=1.0 cm (L << D).

For the case (a), the magnetic field intensity H at the center of the solenoid is 7,721 A/m from above equation. For the case (b), the magnetic field intensity H at the center is 8,305 A/m. Our simulation package created the contour lines of magnetic flux as shown in Figure 5. Figure 5(a) showed the magnetic field is almost parallel inside of this solenoid coil when L is much larger than D, but Figure 5(b) with (D >> L) did not show this. Figure 6 also shows the magnetic fields along the axial direction for both solenoid models. The average errors for both models between our simulation results and the results from the above analytical form are 21.0 A/m and 28.5 A/m, respectively. Especially, the average relative errors around the solenoid coils are both less than 1.3 %.

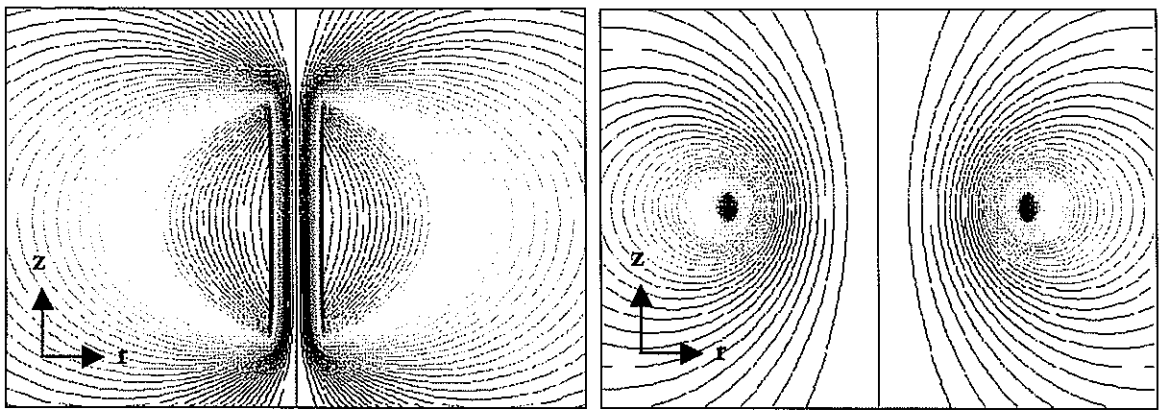

(a) (b)

Figure 5. Contour lines of magnetic flux for two solenoid models with current i =1A, N=1000 turns: (a) D=2.54cm and L=12.7cm, (b) D=12cm and L=1cm

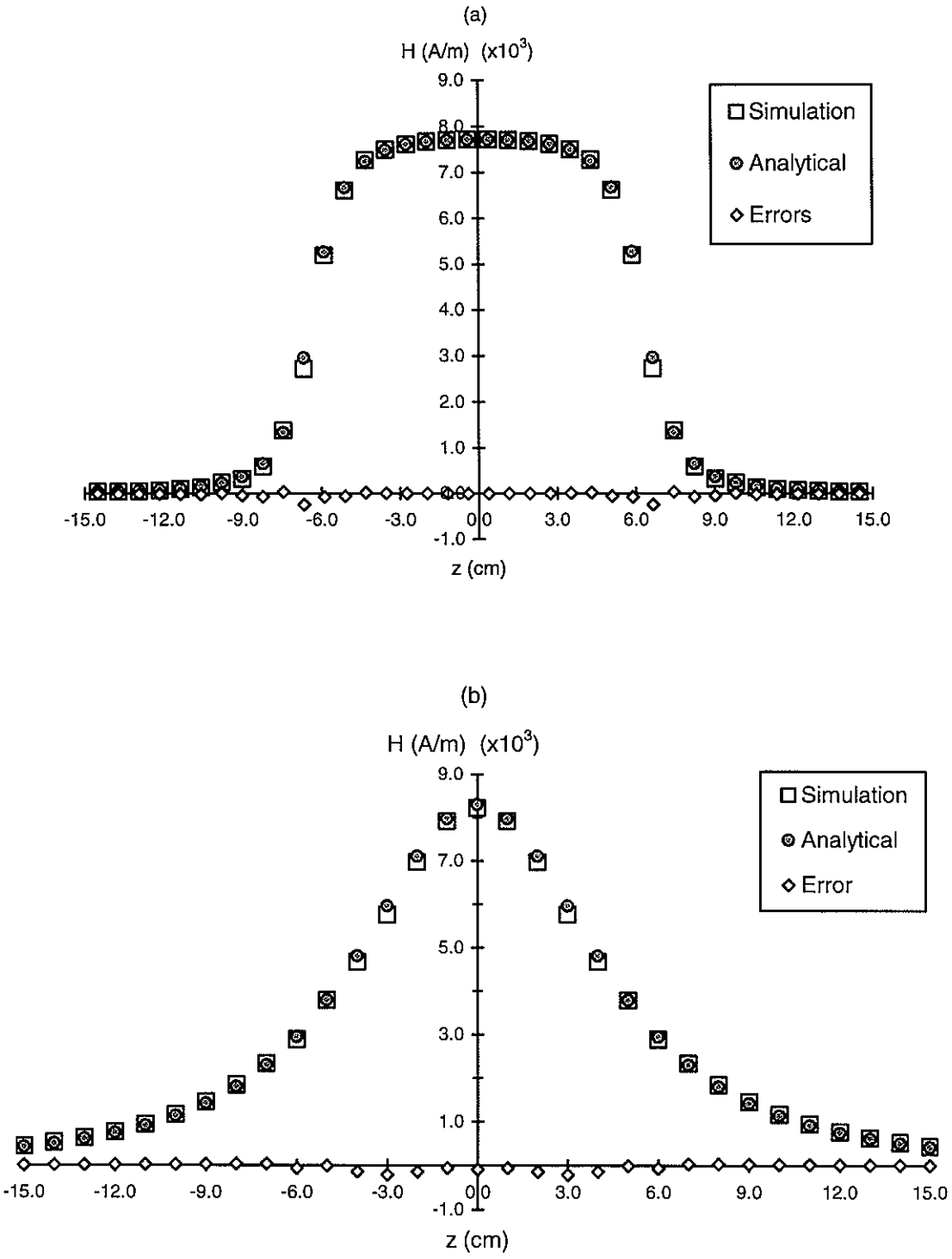

Figure 6. Comparison between simulation and analytical results: (a) the dimension of background space is 10cm x 20cm, (b) the dimension of background space is 45cm x 30cm

2.1.2. Verification of a Nonlinear Permeability Test

An axisymmetric problem was tested for the verification of a nonlinear permeability material with the geometric layout of both a steel object and a solenoid coil as shown in Figure 7(a). The permeability of this steel was experimentally measured as shown in Figure 7(b). The spatial size of the FEM background space was chosen as 15cm (r-axis: 0 cm to 15 cm) by 20cm (z-axis: -10 cm to 10 cm).

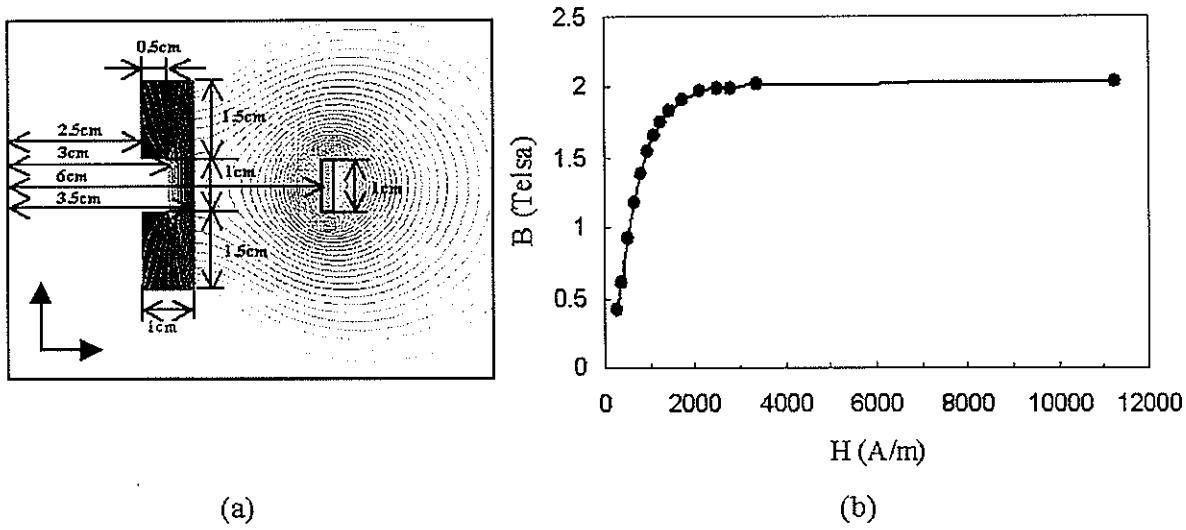

Figure 7. Simulation test settings for a steel sample: (a) the geometries of both a test material and a solenoid source coil (the size of background space was chosen as 10 cm width by 20 cm length), and (b) the permeability of this material

This problem was tested with both our MPI simulation package (named 'MPI.SIM' in Figure 9) and the ANSOFT commercial package [27]. Figure 8 shows the resulting contour plots of equivalent magnetic flux density fields from both programs; they are almost identical: our simulation package gives more detailed magnetic flux contour lines. Figure 9 shows the results of magnetic flux density fields (B-fields) from both packages. Three positions at the r-axis (radial) along the axial direction (z-axis) were chosen for reading B-fields: (1) the center line of the z-axis (r = 0 cm), (2) the inner position at r = 2 cm, and (3) the outer position at r = 4 cm. The results from both packages are almost identical around the defect hole of the test material. However, the difference in calculated B-fields at r = 4cm and

z = 0 cm between both packages may be beyond the acceptable tolerance limit. This was caused by both poor quality of an FEM approximation and the errors from cubic-spline interpolation of the graph.

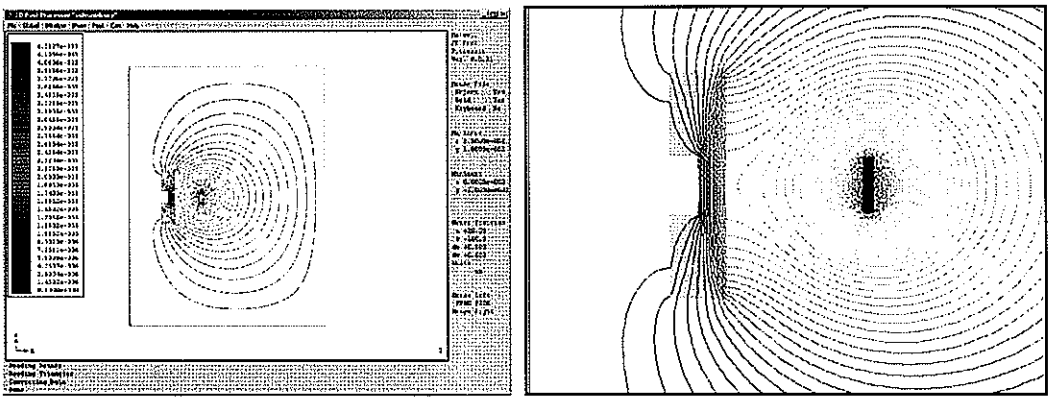

Figure 8. Contour lines of equivalent magnetic flux: (a) ANSOFT and (b) Our MPI Simulation

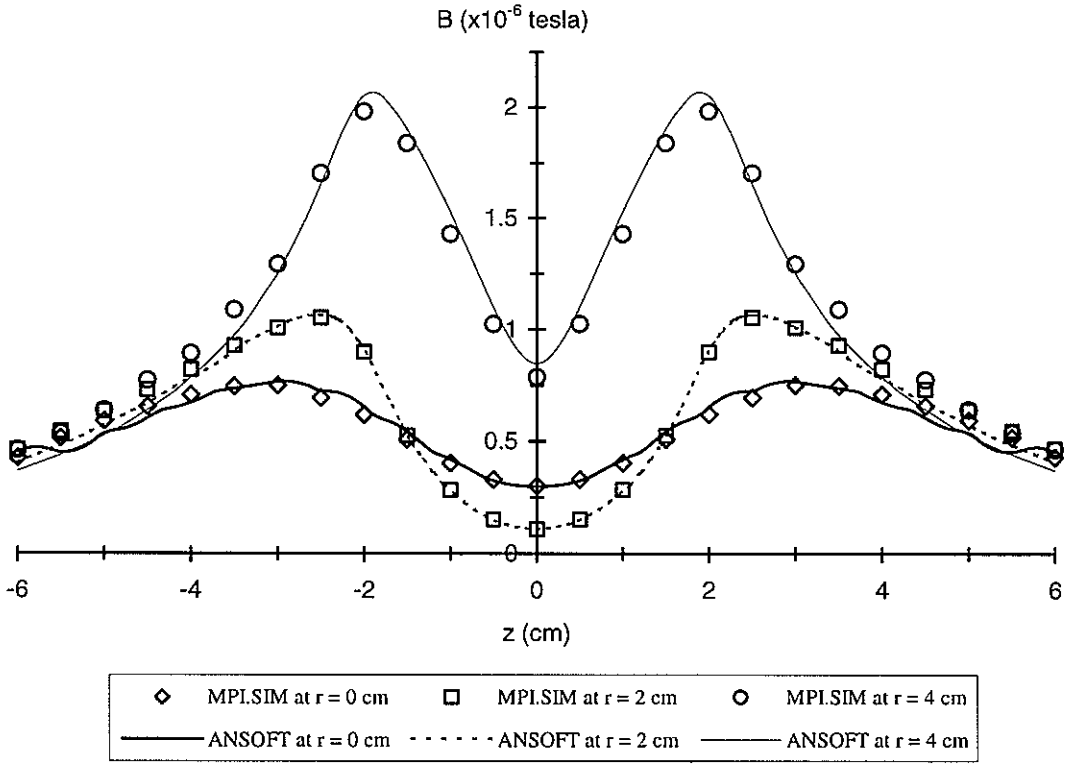

Figure 9. The results of magnetic flux density fields from both our MPI Simulation package and ANSOFT

As shown in Figure 9, there are some irregular curvatures of B-fields at z-axis (r = 0 cm) from the ASNOFT results. This also resulted from poor quality of mesh generation results in the ANSOFT. If more refinement processes of mesh generation provided by ANSOFT were applied, these unexpected curvatures could be easily removed.

2.2. Model Design for MPI-Simulation Environment

We simulated a test sample in the shape of a cylindrical tube by solving Maxwell's equations in a cylindrical coordinate system (r, θ, z). Figure 11 shows the geometry of the solenoid MPI simulation used in the FEM calculations. For axisymmetric geometry, the equation for Ampére's law under DC conditions [28] is

$$\frac{1}{\mu}\left(\frac{\partial^2 \overline{A}}{\partial r^2}+\frac{1}{r}\frac{\partial \overline{A}}{\partial r}+\frac{\partial^2 \overline{A}}{\partial z^2}-\frac{\overline{A}}{r^2}\right)=-\overline{J}_S \tag{2.4}$$

where $\overline{J}_s$ and $\overline{A}$ are the source current density and the vector potential respectively. Asymptotic boundary conditions were applied on the outer surface of the spatial domain. Using the Ritz method [28] one can show that the solution of Equation (2.4) is equivalent to minimizing the energy function W described as:

$$W = 2\pi \iint_{\Omega}\left\{\frac{1}{2\mu}\left(\left|\frac{\partial \overline{A}}{\partial z}\right|^2+\left|\frac{\partial \overline{A}}{\partial r}+\frac{\overline{A}}{r}\right|^2\right)-\overline{J}_s\cdot\overline{A}\right\}rdrdz\ . \tag{2.5}$$

From the vector potential $\overline{A}$ obtained by equation (2.5), the magnetic flux density [28] is computed as follows

$$\vec{B}=\left(-\frac{\partial \overline{A}}{\partial z},0,\frac{\partial \overline{A}}{\partial r}+\frac{\overline{A}}{r}\right)^T. \tag{2.6}$$

Since we are using an FEM computation (i.e., each finite element has unique values of **B**, **H**, and μ), it is assumed that the value of μ is constant for each finite element. Therefore, the magnetic field intensity $\vec{H}$ and the magnetic field gradient components (both $\partial\vec{H}/\partial r$ and $\partial\vec{H}/\partial z$) for each finite element can be easily computed.

For the simulation of a sample using the finite element method (FEM), we modeled a test for investigating the behavior of magnetic particles when a magnetic field was applied using a solenoid. The test sample was assumed to be cylindrical in shape and the shape of the defect on the surface was in the form of a groove. The cross section of the cylindrical sample and the defect is shown in Figure 10. The length and wall thickness of the sample were chosen to be 16 cm and 1 cm, respectively. The defect is located at the center of the sample. The defect size was varied during simulation tests. The distance between the outer boundary and the test sample was set to be sufficiently large to satisfy boundary conditions. Asymptotic boundary conditions were applied to the outer surface.

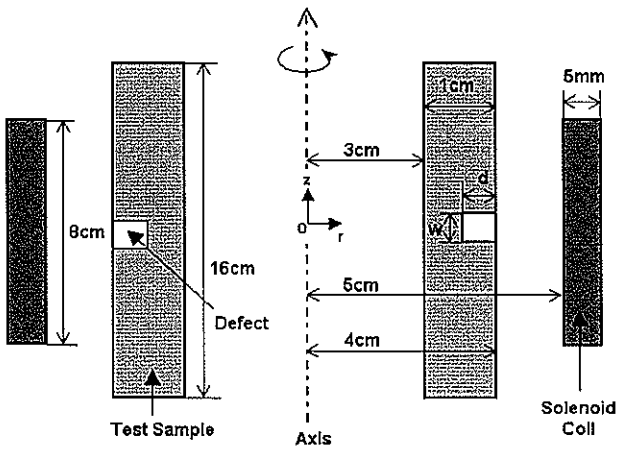

Figure 10. The geometry of simulated test sample with axial symmetry: The defect sizes used in the calculation were depth, d = 3, 5, 7, or 9 mm and width, w = 1, 2, 3, or 5 mm

2.2.1. Simulation of Magnetic Flux Leakage Field

The permeability of the test sample has a nonlinear behavior as shown in Figure 8(b). The magnetic force per unit volume of magnetic particles to retain them is proportional to the product of, the susceptibility of magnetic particles, external magnetic field and the field gradient [21,22]. Therefore, the distribution of the magnetic field gradient around a defect is an important factor in magnetic particle inspection. The gradient of magnetic flux density along the radial direction versus depth (*d* in Figure 10) and width (*w* in Figure 10) are shown in Figure 11.

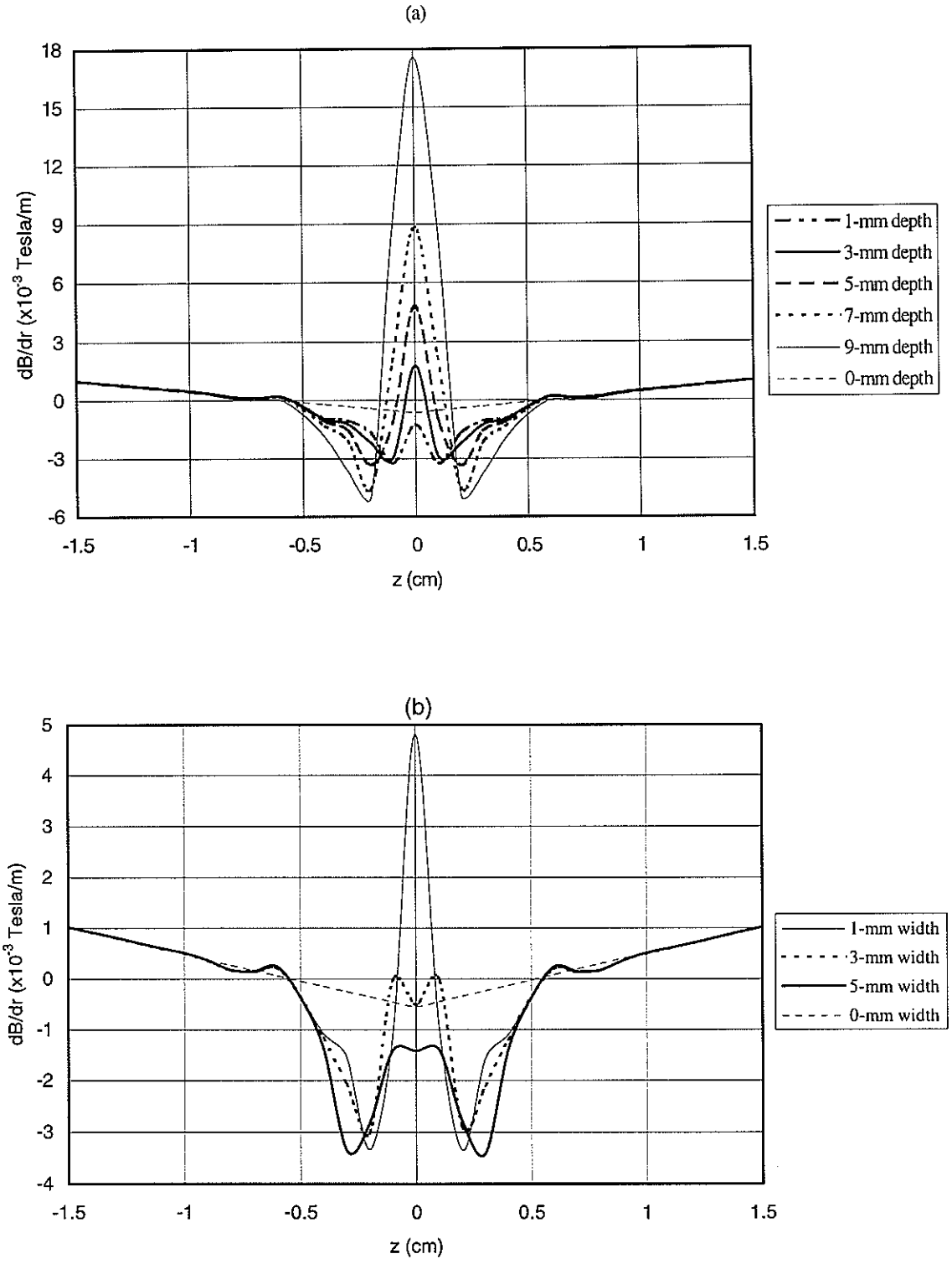

Figure 11. The gradients of magnetic flux density along the radial direction (dB/dr) from 2.0 MA/m^2 current density: (a) $\partial B/\partial r$ vs. defect depths (defect width=1mm), and (b) $\partial B/\partial r$ vs. defect widths (defect depth=5mm)

In the absence of defects the calculations suggested that the magnetic flux density B under a solenoid current field increases linearly from the center of the z-axis to the outside of the cylinder. However, the change of B-field along the radial direction (dB / dr) is higher at the center of the defect than outside of the defect. This result is crucial for the magnetic flux leakage (MFL) test. According to our calculations, as the depth of the defect increases as shown in Figure 11(a), the magnitude of the magnetic field gradient should increase. The peak-to-peak value of magnetic field gradient decreased as the width of the defect increased as shown in Figure 11(b). However, it is very difficult to find the relationship between the peak-to-peak values of magnetic flux leakage and the defect widths since the peak-to-peak values is much less sensitive to the defect width than to defect depths in general.

2.2.2. Magnetic Force on a Magnetic Particle

For magnetic particles to adhere to a defect, the magnetic force generated by an applied current source should be large enough to attract magnetic particles to the defect. Magnetic force on a saturated magnetic particle can be described by the equation

$$F_m \propto -\vec{\nabla}\left(\vec{H}\cdot\vec{M}\right) = -K\vec{\nabla}\left(\vec{H}\cdot\vec{H}\right) \tag{2.6}$$

where $\vec{M}$ is the magnetization vector of the magnetic particle, and K is a constant which contains information on the magnetic property of the magnetic particle such as magnetic susceptibility and its volume.

For the cylindrical coordinate system, the magnetic field vector $\vec{H}$ can be decomposed into a radial component H_r and an axial component H_z. From equation (2.6), the magnetic force components along the r- and z-directions can be written as:

$$\begin{aligned} F_r &= -K\left(H_r\frac{\partial H_r}{\partial r} + H_z\frac{\partial H_z}{\partial r}\right), \\ F_z &= -K\left(H_z\frac{\partial H_z}{\partial z} + H_r\frac{\partial H_r}{\partial z}\right) \end{aligned} \tag{2.7}$$

The quantities $A_r = F_r / K$ and $A_z = F_z / K$ are proportional to the magnetic force components.

An MPI simulation test was set up as shown in Figure 10. The defect size was assigned as 1-mm width and 5-mm depth. The applied current density was 2.0 MA/m^2. Figure 12(a) shows the nonlinear permeability of the test material obtained by experimental test, and Figure 12(b) shows the susceptibility of the magnetic particles, calculated from the measurement results in Figure 13(a).

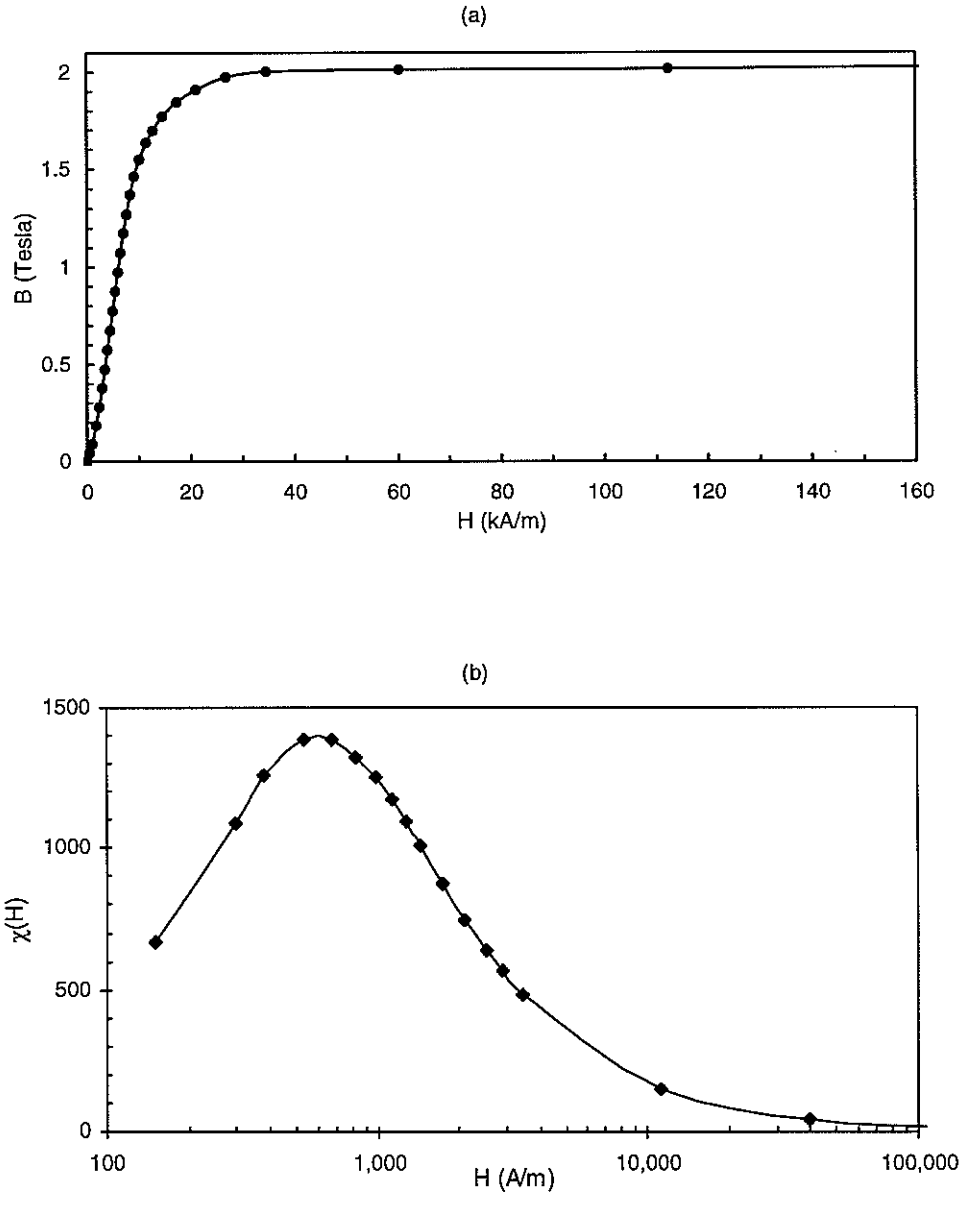

Figure 12. Set up test materials: (a) permeability of the test material, and (b) the susceptibility of the magnetic particles

When the length of a test material is several times larger than its diameter, a longitudinal magnetic field can be relatively easily established in the material. When the orientation of a defect is perpendicular to the direction of magnetic field, one can detect leakage fields at the center of the flaw. The material should be placed longitudinally in the concentrated magnetic field that fills the center of a solenoid. Liquid magnetic particle ink is the most appropriate way for this MPI test environment. We assumed the liquid magnetic ink was sprayed uniformly onto the surface of material while a DC current is activating as shown in Figure 13. Also, we assumed the test material slowly rotated 360 degree while the material was being sprayed, so that the gravitation at force on the magnetic particles can remove some magnetic particles that have weaker magnetic force that this gravitational force in the radial direction. It will only allow the detection of significant sizes of flaws that may have stronger magnetic attraction force on the magnetic particles than the force of gravitation.

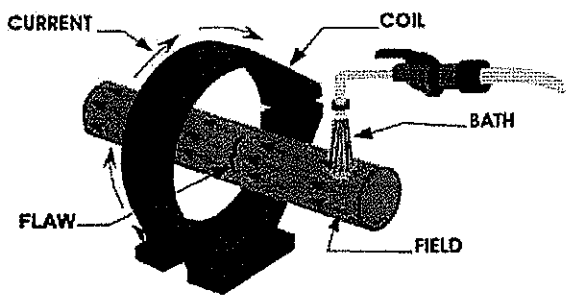

Figure 13. MPI test using a solenoid[1]

The values of $\mu_0 A_z$ and $\mu_0 A_r$ are plotted in Figure 14. The applied current density is here 2.0 MA/m^2. The black dotted line shown in Figure 14(a) indicates the values of $\mu_0 A_z$ without any defect in the test material. When a test material is been rotating while it is being strayed, the axial component of magnetic force at the surface of the material is perpendicular to the gravitational force of magnetic particles, but the radial component of it is opposite to the gravitation. Therefore, the values of radial force $\mu_0 A_r$ are more important for MPI for than the axial force $\mu_0 A_z$.

[1] This Figure is provided by the NDT Resource Center. For more details, see the following web page: http://www.ndt-ed.org/EducationResources/CommunityCollege/MagParticle/Physics/Magnetization.htm.

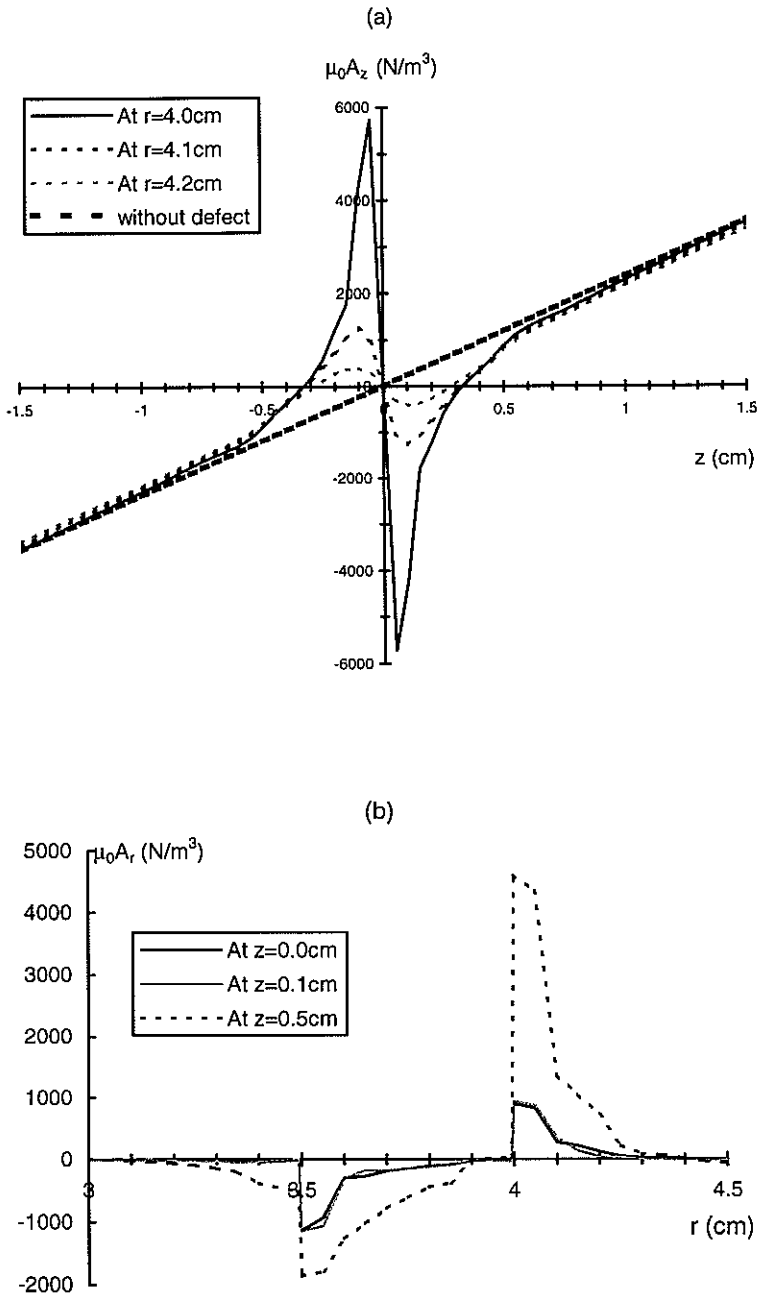

Figure 14. Magnetic force per unit volume on magnetic particles (without consideration of their susceptibility): (a) $\mu_0 A_z$ along the axial direction, where the centers of a defect (with 1-mm width) and the coil rod are located at z=0, and (b) $\mu_0 A_r$ along the radial direction, where the defect starts from r=3.5 cm and ends at r=4.0 cm

Both black solid lines and gray dotted lines shown in Figure 14(a) represent the values of $\mu_0 A_z$ when the measuring points from the radial axis (r-axis) are at r = 4 cm (the

outer surface of the test object), 4.1 cm (1-mm off the surface), and 4.2 cm (2-mm off the surface), respectively. The force on the magnetic particles was decreased from the end of the test object. The force almost disappeared around 0.3 cm of r-axis. Then, force extremely increased up to the boundary of defect hole around the center axis (i.e., z-axis) and suddenly decreased to the center of z-axis. As shown in Figure 14(a), the strength of force depends on the offset distance from the surface of the test material, the depth of defect, and the magnetic field strength. Therefore, this axial component of magnetic force $\mu_0 A_z$ explains how magnetic particles will be moved on the surface of the test material and a defect site. However, this axial component of magnetic force cannot keep magnetic particles from gravitational force.

Figure 14(b) shows the values of $\mu_0 A_r$, the radial component of relevant magnetic force, by which the particles are attracted along the radial direction. There are two positions of magnetic particle stacks: at the bottom of the defect and at the top of it. The black solid line in Figure 14(b) represents the values of $\mu_0 A_r$ at the center line of defect hole (z=0cm). The force at the surface of the defect hole (the black dotted line) shows stronger than that at the center line (the gray solid line). This results in the effect of extremely strong magnetic fields inside of the test material. Figure 15 shows the contour lines of magnetic flux around a defect site. As shown in Figure 15, the magnetic potential energy is a maximum at the bottom of the defect, and there are some leakage fields at the top of it, so that the particles may be retained there. The values of $\mu_0 A_r$ are more important than $\mu_0 A_z$, because this component opposes the gravitational force. Figure 16 shows a three-dimensional plot of the values of $\mu_0 A_r$. Because of the average computation for each finite element in Figure 16, the values of $\mu_0 A_r$ at the center line are the same with those at the surface, to the contrary of Figure 14(b). The reason why the relative forces at the surface of defect hole is less than those at the center line is the susceptibility of magnetic particles.

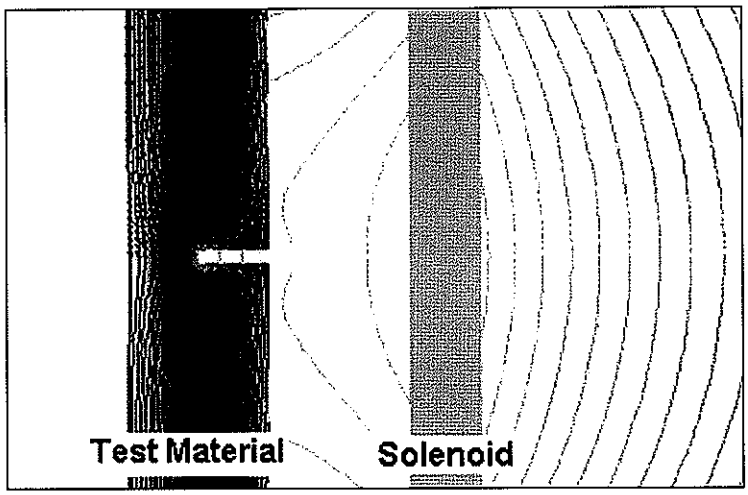

Figure 15. Magnetic flux contour lines around a defect of 5-mm depth by 1-mm width: the current density was 2.0 MA/m^2 from the source solenoid

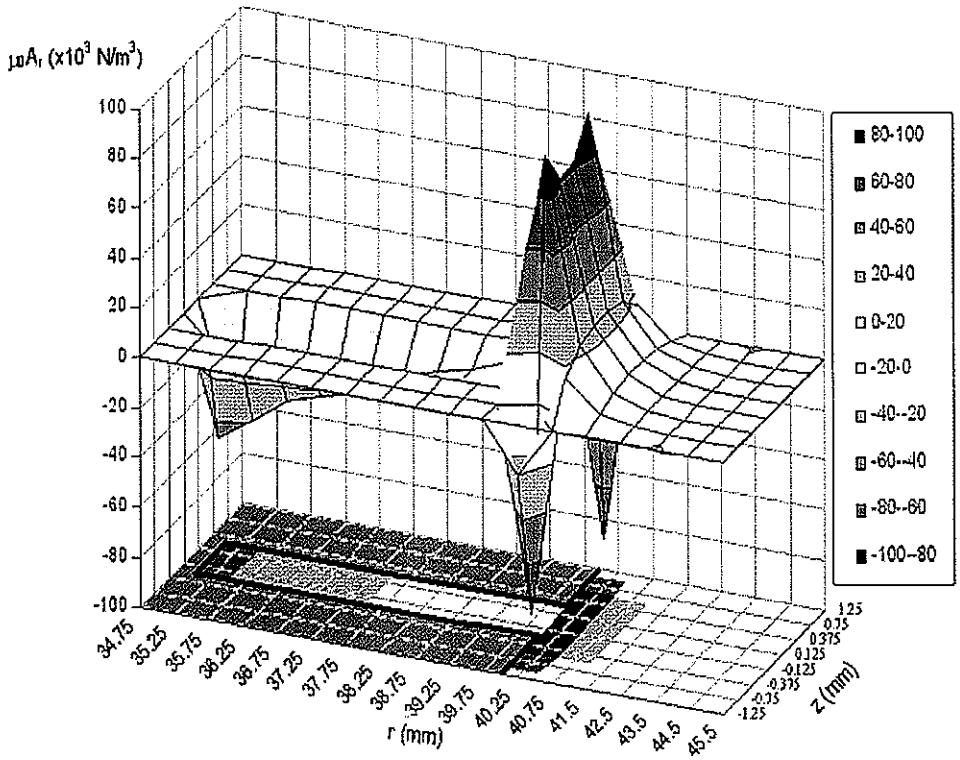

Figure 16. Relative magnetic force ($\mu_0 A_r$) per unit volume of particles along the radial direction

2.3. MPI-FEM Algorithm

Schwartzender has pointed out that the modeling of MPI is complex problem involving magnetic force, gravitational force, viscous force, and interactive force between magnetic particles [9,29]. In this thesis, for a simple MPI simulation, the gravitational force was considered as the resistance against the magnetic force that makes magnetic particles retained in the defect site. The mass density ρ of liquid magnetic particles (iron oxides) is about 5000 kg/m^3. Let g be the gravitational constant (9.80 m/sec^2), and ρ_w be the water density (=1000 kg/m^3). Suppose the volume V_{MP} of magnetic particles is retained inside of the defect. Then gravitational force F_g of these particles is computed as

$$F_g = (\rho - \rho_w)\, g\, V_{MP}. \tag{2.8}$$

Suppose the magnetic field is measured as $\vec{H}$ at the center of the magnetic particle cluster. Let the susceptibility of these particles be known as $\chi(H)$. Then, the magnetostatic energy is given by

$$\begin{aligned} W_M &= \mu_0 V_{MP} \int_0^{\vec{H}} M(\vec{H}) \cdot d\vec{H} \\ &= \mu_0 V_{MP} \int_0^{\vec{H}} \chi(\tilde{H})\, \tilde{H} \cdot d\tilde{H}. \end{aligned} \tag{2.9}$$

The magnetic forces on the magnetic particles are given by [12]

$$\begin{aligned} F_r &= -\frac{\partial W_M}{\partial r} = -\mu_0 V_{MP} \frac{\partial \vec{H}}{\partial r} \frac{\partial}{\partial \vec{H}} \int_0^{\vec{H}} \chi(|\tilde{H}|)\, \tilde{H} \cdot d\tilde{H} \\ &= -\mu_0 \chi(|\vec{H}|) V_{MP} \vec{H} \cdot \partial \vec{H} / \partial r = \mu_0 \chi(|\vec{H}|) V_{MP} A_r, \end{aligned} \tag{2.10}$$

and similarly

$$F_z = \mu_0 \chi(|\vec{H}|) V_{MP} A_z. \tag{2.11}$$

From our axisymmetric modeling, since F_z is perpendicular to the gravitational force, F_r is the only signifiant force against F_g. If F_r is greater than F_g, the magnetic volume V_{MP} will be retained in the defect site. From the equations (2.8) and (2.10), a new MPI-test function is defined as

$$T_{MPI}(\vec{H}, A_r) = \begin{cases} 1, & R(\vec{H}, A_r) \geq 1 \\ 0, & R(\vec{H}, A_r) < 1 \end{cases}, \tag{2.12}$$

where

$$R(\vec{H}, A_r) = \left| \frac{F_r}{F_g} \right| = \frac{\mu_0 \chi(|\vec{H}|) |A_r|}{(\rho - \rho_w) g}. \tag{2.13}$$

This MPI-test function $T_{MPI}(\vec{H}, A_r)$ represents the possibility that a single magnetic particle is retained around a defect site or a particular position with the condition of a magnetic field $\vec{H}$ and its gradient ($\partial H_r / \partial r$, $\partial H_z / \partial r$) along the radial direction in the real situation.

For the purpose of FEM numerical calculations it was assumed that the magnetic field intensity H and the susceptibility $\chi(H)$ of magnetic particles are constant in the area of each finite element. This means that all values of magnetic properties for each finite element are averaged. The value of $R(\vec{H}, A_r)$ for each finite element represents the average value of force ratio in this element. Therefore, if it is very close to unity, but less than one, the real value of $R(\vec{H}, A_r)$ at some points in this finite element may be greater than one because magnetic fields strengths are different at any point in a real environment. For example, suppose the value of $R(\vec{H}, A_r)$ is 0.5 for an arbitrary finite element. If this finite element can be split as two elements so that the value of $R(\vec{H}, A_r)$ at the one element is more than 1, and the value at the other element is less than 1. Because of the unknown function of $R(\vec{H}, A_r)$, it is impossible to estimate the volume ratio between two finite elements. However, by assuming the uniform distribution of magnetic particles in these finite elements, it is more reasonable to say that the element, at which the value of $R(\vec{H}, A_r)$ is more than 1, has the half volume of the original finite element. Similarly suppose the value of $R(\vec{H}, A_r)$ is 0.8 for an arbitrary finite element. Then this element can be evenly split to ten small finite elements. The probability that eight small elements among ten elements have the value of $R(\vec{H}, A_r)$ more than 1 is more possible than any other cases (i.e., the probability that any number of less than or more than eight elements among them have the value of $R(\vec{H}, A_r)$ more than 1)

according to the assumption of uniform distribution (this is the same concept of maximum likelihood of an unknown probability function in statistics [29]). For better approximate of the estimate volume of magnetic particles, the probability function of detecting magnetic particles around a defect site at the steady state is defined as

$$P_{MPI}(\vec{H}, A_r) = \begin{cases} 1 & R(\vec{H}, A_r) \geq 1, \\ R(\vec{H}, A_r) & 0.5 \leq R(\vec{H}, A_r) < 1, \\ 0 & R(\vec{H}, A_r) < 0.5. \end{cases} \tag{2.14}$$

Equation (2.14) is employed in our MPI simulation tool only for a heuristic approximation of estimate volume of magnetic particles. It is obvious that the estimate magnetic particles V_{MPI} is located in the range of

$$V_i \cdot I(R(\vec{H}, A_r) \geq 1) \leq V_{MPI} \leq \sum_{E_i \in \{air\}} V_i \cdot I(R(\vec{H}, A_r) > 0). \tag{2.15}$$

where $I(x)$ is the unity function that it has unity only when x is true; otherwise zero. In this thesis it is assumed that the approximate volume of magnetic particles at the steady state is

$$V_{MPI} \cong \sum_{E_i \in \{air\}} V_i \cdot P_{MPI}(i). \tag{2.16}$$

The following algorithm for this thesis, denoted the MPI-FEM algorithm, has been developed. It can be extended to any three dimensional problems in general. However, it is more suitable for applying to a DC mode than to an AC mode to simulate an MPI test. In this thesis any AC-mode problem has not been tested and evaluated. The relationship between eddy currents on the behaviors of magnetic particles is beyond scope of the present research.

2.3.1. MPI-FEM Algorithm

(STEP 0) Preparing for an MPI simulation: There are three initial steps for starting an MPI simulation:

- Preparing for PDE input parameters: One must prepare for either user-defined B-H curves (for permeability) for all test materials (in the case of nonlinear PDE problems) or user-defined Jiles-Atherton hysteresis parameters for

hysteretic magnetic materials), a user-defined susceptibility table for magnetic particles with respect to magnetic fields, and a source current density.

- Preparing for FEM information: One must prepare for all geometries of test materials, a source coil, a background space, and the boundary conditions of the background. Also, one must prepare for mesh information including meshed finite elements, vertex information of the elements, and neighborhood for each element.
- Preparing for MPI information: One must prepare for the gravitational information of magnetic particles such as the mass density of a magnetic particle liquid (the default is 5,000 kg/m^3), and a scale parameter γ(the default is zero) in (2.10).

(STEP 1) Solve the current Maxwell problem constructed as the form of equation (1.44).

(STEP 2) For each finite element in the air (the material properties of each finite element consist of user-defined material, magnetic particles, source coil, and air), compute $T_{MPI}(\vec{H}, A_r)$. Note that the material properties in a defect are treated as the same as the air.

(STEP 3) If the values of $T_{MPI}(\vec{H}, A_r)$ for all finite elements in the air are zero, go to (STEP 5) for exiting the loop.

(STEP 4) If $T_{MPI}(\vec{H}, A_r) = 1$ at any finite element in the air, replace the material property of this element with magnetic particles from the air. Reconstruct a new FEM problem as shown in (1.44). Then, go to (STEP 1).

(STEP 5) (Termination) Let E_i be the ith finite element, which is located in the air, and $P_{MPI}(i)$ be the probability of magnetic particles to be retained in E_i computed from (STEP 2). For the estimation of the magnetic particle volume in a defect site, process the appropriate step among the following cases.

- For an axisymmetric case: Let (x_i, y_i) be the center position of E_i, and Δ_i be the size of its area. Then, the volume (V_{MPI}) of retained magnetic particles around the defect site is computed as

$$V_{MPI} = 2\pi \sum_{E_i \in \{air\}} x_i \Delta_i \cdot P_{MPI}(i). \tag{2.17}$$

- For a 2-D planar case: Let Δ_i be the area of E_i. Then, the volume per a unit thickness of the test material (A_{MPI}; i.e., the cross-sectional area) of retained magnetic particles around the defect site is computed as

$$A_{MPI} = \sum_{E_i \in \{air\}} \Delta_i \cdot P_{MPI}(i). \tag{2.18}$$

- For a 3-D case: Let V_i be the volume of E_i. Then, the volume of retained magnetic particles around the defect site is computed as

$$V_{MPI} = \sum_{E_i \in \{air\}} V_i \cdot P_{MPI}(i). \tag{2.19}$$

For computing A_r in $P_{MPI}(\vec{H}, A_r)$ in (STEP 2), the FEM computation of magnetic field gradients is essential. Suppose that there are three finite elements (a, b, and c) in the air as shown in Figure 17(a). Let $A(r_1, z_1)$, $B(r_2, z_2)$, and $C(r_1, z_1)$ be the center of these elements

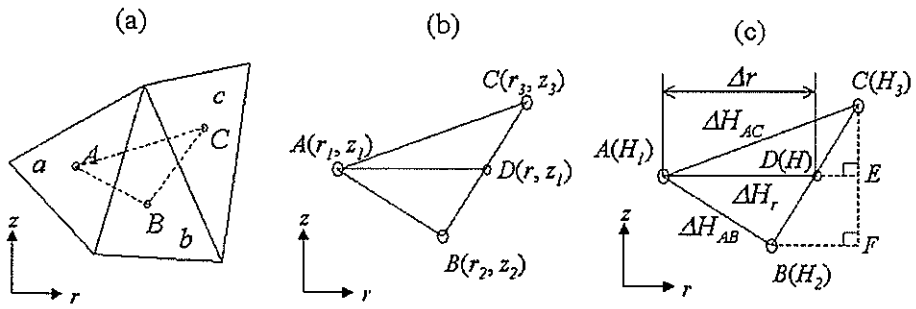

Figure 17. Computing the magnetic field gradient along the radial direction at the center A of the element a: (a) three finite elements, a, b, and c, (b) the center points of them, A, B, and C, and (c) the differences of magnetic fields (ΔH_r) and distance (Δr) of two points A and D

Let D(r, z) be the point on the line BC such that the vector AD should be parallel to the r-axis as shown in Figure 17(b). Then, the position of $D(r, z)$ is computed as

$$D(r,z) = D\left(r_3 - (r_3 - r_2)\left(\frac{z_3 - z_1}{z_3 - z_2}\right), \quad z_1 \right) \tag{2.20}$$

Let E and F be the cross-sections of the two parallel lines to the r-axis passing through either point D or B and the perpendicular line to the r-axis passing through the point C, respectively. Let H_1, H_2, H_3, and H be any arbitrary physical values at A, B, C, and D, respectively. As shown in Figure 17(c), it is obvious that the distances of the line CE and CF are respectively (z_3-z_1) and (z_3-z_2), and the differences in physical values of vectors DC and EC are respectively (H_3-H) and (H_3-H_2). From two triangles CDE and CBF, H is easily computed as

$$H_3 - H = (H_3 - H_2)\left(\frac{z_3 - z_1}{z_3 - z_2}\right) \tag{2.21}$$

Let H_A (H_{ar}, H_{az}), H_B (H_{br}, H_{bz}), H_C (H_{cr}, H_{cz}), and H_D (H_{dr}, H_{dz}) be the magnetic fields at the points A, B, C, and D, respectively. Then, the difference ΔH_{AD} of magnetic fields of the vectors AD is (H_{dr}-H_{ar}, H_{dz}-H_{az}). Also, the differences ΔH_{BC} and ΔH_{DC} of magnetic fields of the vectors BC and DC are respectively (H_{cr}-H_{br}, H_{cz}-H_{bz}) and (H_{cr}-H_{dr}, H_{cz}-H_{dz}). Since these are the values of (H_3-H_2) and (H_3-H) in Equation (2.21), the components of ΔH_{AD} = (H_{dr}-H_{ar}, H_{dz}-H_{az}) are computed as

$$\begin{aligned} (H_{dr} - H_{ar}) &= (H_{cr} - H_{ar}) - (H_{cr} - H_{br})\left(\frac{z_3 - z_1}{z_3 - z_2}\right) \\ (H_{dz} - H_{az}) &= (H_{cz} - H_{az}) - (H_{cz} - H_{bz})\left(\frac{z_3 - z_1}{z_3 - z_2}\right) \end{aligned} \tag{2.22}$$

Therefore, since $\Delta H_r \equiv \Delta H_{AD}$ and Δr is the distance of the line segment AD, the magnetic field gradient at the point A can be approximately computed as $\Delta H_r / \Delta r$, where

$$\Delta r = (r_3 - r_1) - (r_3 - r_2)\left(\frac{z_3 - z_1}{z_3 - z_2}\right). \tag{2.23}$$

2.3.2. Example: MPI test for a defect with 2-mm width and 5-mm depth

To demonstrate this MPI-FEM algorithm, an example is provided in this thesis. Suppose that the geometric conditions for an MPI problem were the same as shown in Figure 11. As boundary conditions, the Dirichlet condition (any vector potential A = 0 at the boundary) was also chosen. The applied current density (as a DC mode) was set up as 100 kA/m^2 (2 MA/ m^2 is too large for simulating an MPI test). The permeability of the test materials and the susceptibility of the magnetic particles are assumed to be the same as shown in Figure 12.

Figure 18 shows the results of $R(\vec{H}, A_r)$ of each finite element in the air for each loop of the MPI-FEM algorithm. For this problem, total three iterations were consumed. Black dots in Figure 18 represent finite element mesh areas of which values of $R(\vec{H}, A_r)$ are greater than two, dark gray dots for the values of greater than 1.0 but less than 2.0, and light gray dots for the values of less than 1.0, but greater than 0.5, respectively. Therefore, the black and dark gray dots represent the mesh areas that are 100 % filled by magnetic particles, and light gray dots represent those that are partially filled.

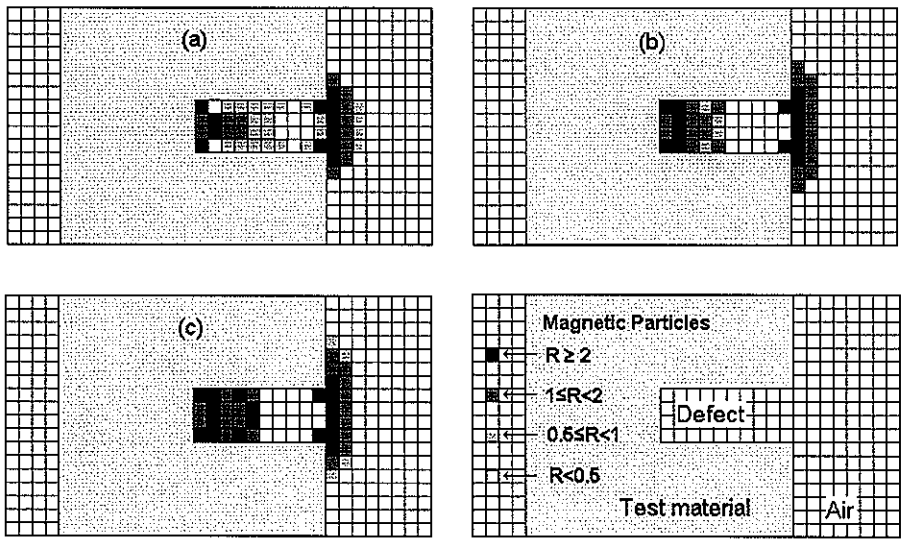

Figure 18. Three iterations of MPI-FEM algorithm for the simulation of an MPI test: (a) to (c) represent the iteration number of the MPI-FEM algorithm. Block dots have the values of $R(\vec{H}, A_r)$ greater than or equal to 2.0, dark gray dots have the values greater than or equal to 1.0 but less than 2.0, and light gray dots have the values less than 1.0, but greater than or equal to 0.5. The size of this defect was 5-mm depth and 2-mm width, and the applied current density was 100 kA/m^2.

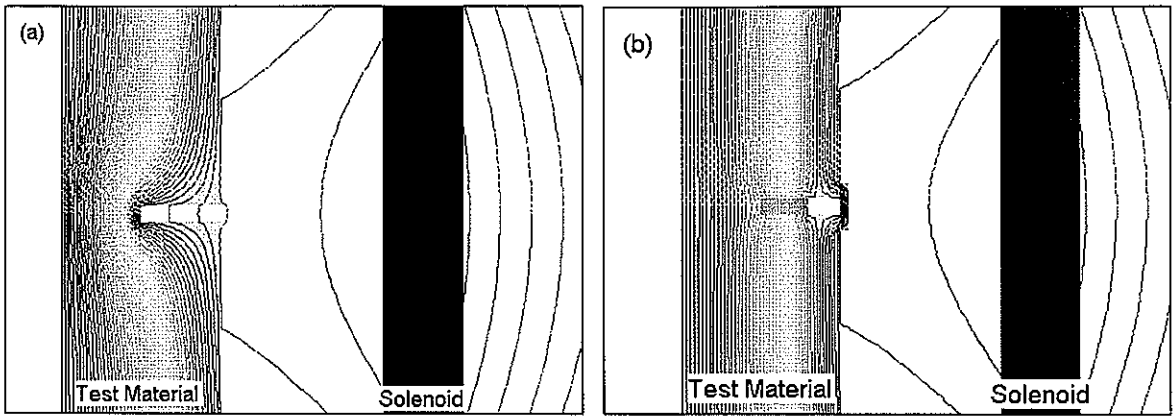

Figure 19. Magnetic flux lines from example: (a) before magnetic particles are retained, and (b) after they are finally retained

After some magnetic particles were retained in position for each loop step shown in Figure 18, a new calculation was made. This MPI-FEM procedure is a generic algorithm for the consideration of an effect of the existence of magnetic particles from the previous history. The total volume of magnetic particles was 2,662 mm^3 at the final step for this problem.

Figure 19(a) shows the magnetic flux contour lines without the effect of magnetic particles, and Figure 19(b) shows the flux lines after magnetic particles are retained. In the absence of magnetic particles there were some magnetic flux leakage fields around the defect as shown in Figure 19(a). However, the magnetic particles absorbed all magnetic flux leakage fields as shown in Figure 19(b).

2.4. Sensitivity Analysis of Simulations for MPI using FEM

Several sizes of defect geometry were simulated using a solenoid as a magnetic field source as shown in Figure 11. Table 3 shows the estimated volume of retained magnetic particles around a defect with respect to its various sizes from our MPI simulation package. The distributions of retained magnetic particles for different size of defects are also shown in Figure 20. The volume (V_{defect}) of defect size with the depth d and width w can be computed for this axisymmetric case shown in Figure 11 as following:

$$V_{defect} = 2\pi w \int_{40-d}^{40} r dr = \pi w d(80+d)\ (mm^3). \tag{2.24}$$

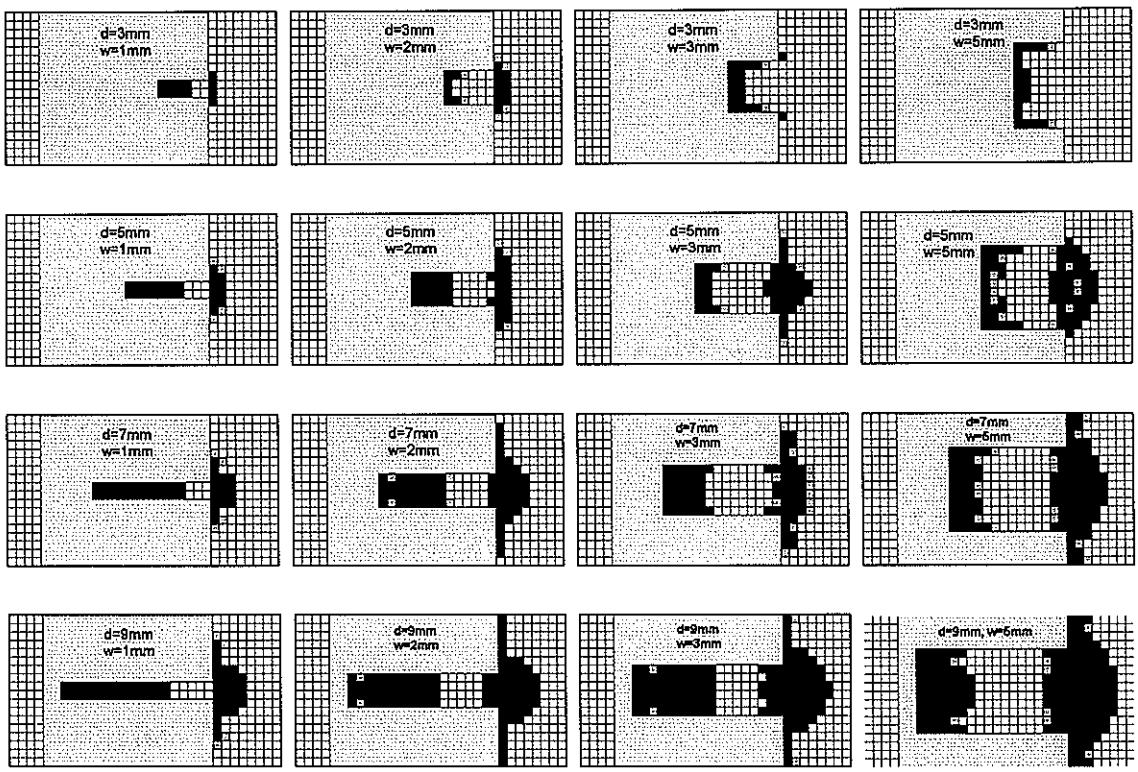

Figure 20. The results of calculations for 16 different defect sizes from our MPI Simulation package: For each result, d means the depth of a defect, and w means its width. Black and gray colors represent the density of magnetic particles. Black dots indicate that magnetic particles are 100 % filled in those positions. Gray dots indicate the particles are partially filled in those areas.

Table 4 shows the defect volume (V_{defect}) with different sizes according to Equation (2.24). For finding the relationship between a simulated MPI result and the shape of a defect, we introduce an MPI volume ratio (φ_{MPI}), such that

$$\varphi_{MPI} = \frac{V_{MPI}}{V_{defect}}. \tag{2.25}$$

Figure 21 shows the above volume ratios. For a fixed size of a defect width, the MPI volume ratio increased as the size of a defect depth increased as shown in Figure 21(a). On the other hand, the volume ratio decreased as the size of defect width increased with a fixed size of defect depth as shown in Figure 21(b). When the size of a defect width is extremely large compared with defect depth (namely, if the thickness of a pipeline is changed), retained magnetic particles will be found at the border of the thickness change. This is very similar to the result of the defect of 3-mm depth and 5-mm width as shown in Figure 20.

Table 3. Simulation results for different size of defects with the current density 100 kA/m^2 (unit: mm^3)

Retained volumes of magnetic particles around a defect site		Defect width			
		1 mm	2 mm	3 mm	5 mm
Defect depth	3 mm	730	1,220	1,212	1,320
	5 mm	1,534	2,738	3,217	4552
	7 mm	2,548	4,582	5,886	9023
	9 mm	3,606	6,807	8,807	13,672

Table 4. The defect volume (V_{defect}) with different sizes

Defect volume (mm^3)		Defect width			
		1 mm	2 mm	3 mm	5 mm
Defect depth	3 mm	782	1,565	2,347	3,911
	5 mm	1,335	2,738	4,006	6,676
	7 mm	1,913	3,827	5,740	9,566
	9 mm	2,516	5,033	7,549	12,582

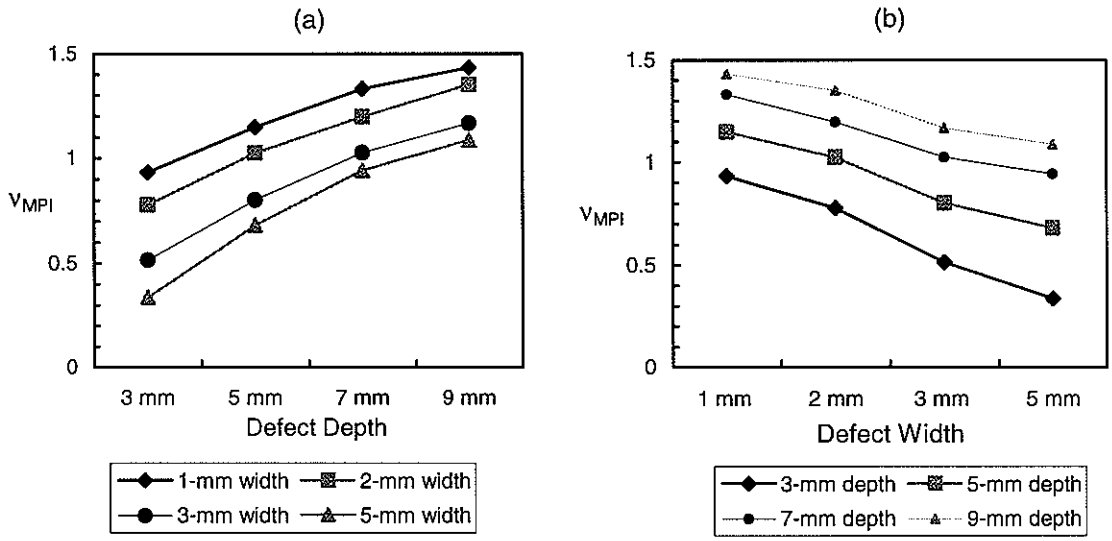

Figure 21. Sensitivity analysis showing accumulation of magnetic particles with (a) varying defect depths and (b) varying defect widths

An important result is that MPI is more sensitive to the narrower and deeper defects than to wider and shallower ones, and is not simply sensitive to the "size" of flaw. For example, the defect with 9 mm depth and 1 mm width has much larger amount (3,606 mm^3) of retained magnetic particles than the defect with 3 mm depth and 5 mm width (1,320 mm^3), even though the defect volume (V_{defect}) of the narrower one is less than the wider one. Figure 21 explains that the estimated volume of retained magnetic particles is more sensitive to the defect depth than the defect width. If the defect becomes wider, the distribution of retained magnetic particles will be found on the surface of the defect as shown in Figure 20. On the other hand, if the defect depth is deeper, retained magnetic particles are found at not only the bottom of defect but also the top of it. The bridges of retained magnetic particles as shown in Figure 20 are weakened as the defect width is increased. However, defect depth makes them stronger and thicker.

When one processes a numerical simulation for an MPI test, there is very important design for appropriate simulation: any test material must be located far from a source solenoid; otherwise, a simulation result may show some magnetic particles makes some bridge between a defect site and the solenoid, because of very strong magnetic field gradient between the test material and the solenoid.

2.5. Summary

Using the finite element method, the magnetic flux density, the magnetic field gradient, and the magnetic force on magnetic particles at the site of a defect were calculated. The calculation showed that the magnetic flux leakage field at the defect created a magnetic force, which attracted and retained the magnetic particles at the defect location. The magnetic particle inspection technique is more sensitive to the defect geometry than the magnetic flux leakage measurement technique, from which method it is difficult to predict the geometry of a defect. Reduction of the inspection design cost, time, and improvement of analysis of experimental data can be achieved by the use of FEM simulations combined with careful incorporation of MPI parameters such as magnetic field source, magnitude of the applied current, defect size, position of defect, and magnetic properties of both test sample and magnetic particles.

In situations of general axisymmetric problems, since the geometry of a solenoid system and the positioning of a (given) test material are fixed at the beginning of an MPI test, the only control parameter for the MPI test is the current density of DC mode. Because of the assumption that there is no hysteresis in the ferromagnetic materials, an MPI simulation must be processed while a current density still exists. In the situation after the power is turned off, the magnetic field and magnetization in the test material is automatically reduced to zero according to the assumption. However, in real situations of ferromagnetic materials, there exists hysteresis of the materials, which results in a finite remanent magnetization even in the absence of an applied field [21,22]. Then, there exists some relationship between defect geometry and the properties of hysteresis in the field of MPI applications. The next chapter will discuss the effect of hysteresis on an MPI test.

CHAPTER 3.

HYSTERESIS ANALYSIS ON SIMPLE GEOMETRY PROBLEMS

When a ferromagnetic material is magnetized in one direction, its magnetization will not relax back to zero when the imposed magnetic field is removed. It must be driven back to zero by a coercive field in the opposite direction. If an alternating magnetic field is applied to the material, its magnetization will trace out a loop called a hysteresis loop as shown in Figure 22(a). The lack of reversibility of the magnetization curve is called hysteresis and it is related to the existence of magnetic domains in the material. Once the magnetic domains are reoriented, it takes some dissipation of energy to turn them back again to the original direction. This property of ferromagnetic materials is useful as a magnetic "memory". Some compositions of ferromagnetic materials will retain high levels of an imposed magnetization even in the presence of large opposite fields and are useful as "permanent magnets". A good permanent magnet should produce a high magnetic field with a low mass, and should be stable against the influences, which would demagnetize it. The desirable properties of such magnets are typically stated in terms of the *remanence* and *coercivity* of the magnet materials as shown in Figure 22(b).

Ferromagnetic materials in which the magnetization can be reversed by a small opposing field are said to be *magnetically soft. Magnetically soft* materials are used for the cores of transformers to reduce the energy losses associated with the reversing fields of the AC currents. The *magnetically soft* materials may have high permeability but small coercivity, and therefore have very narrow hysteresis loops as shown in Figure 23. On the contrary, the materials with low permeability and high coercivity from which permanent magnets are made are sometimes said to be *magnetically hard.* A *magnetically hard* material can generate a useful flux in the air gap of a device without external sources.

(a)

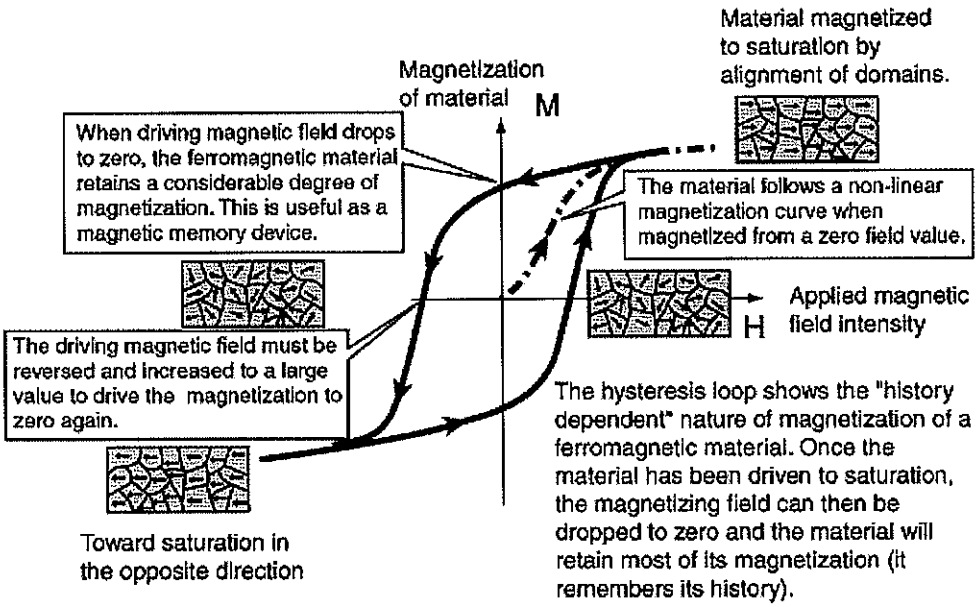

(b)

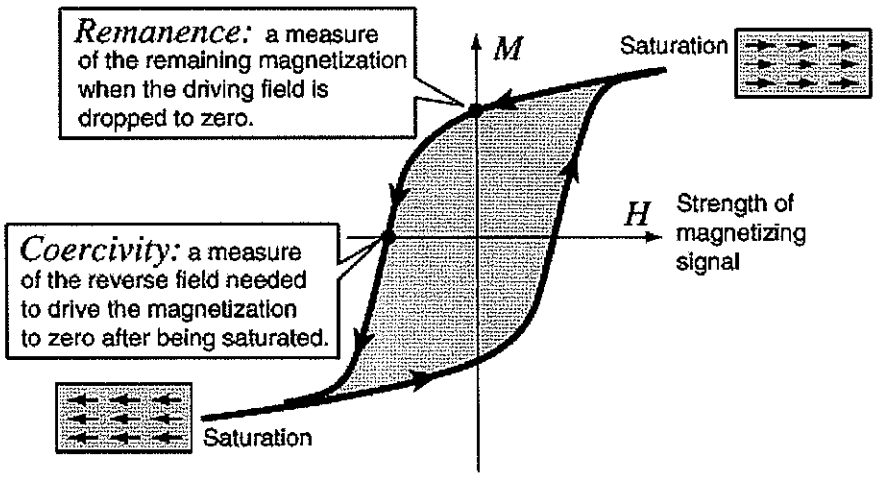

Figure 22. Hysteresis loop[2]: (a) the characteristics of a hysteresis loop, (b) coercivity and remanence in a hysteresis loop [31]

[2] These figures are provided by the web site at http://hyperphysics.phy-astr.gsu.edu/hbase/solids/hyst.html.

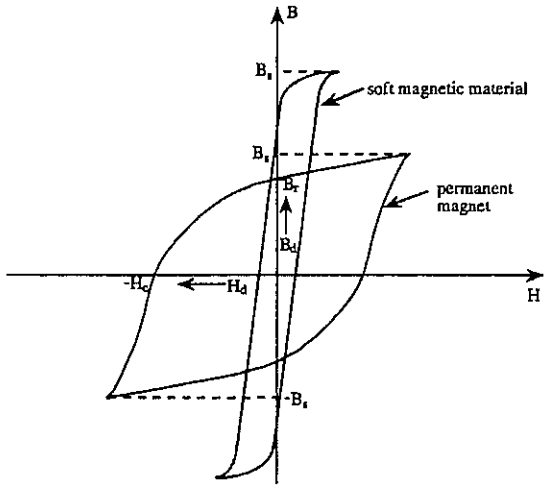

Figure 23. Magnetically soft materials and magnetically hard materials

3.1 Introduction to Hysteresis Modeling

Hysteresis occurs often in nature, arising usually as a result of cooperative behavior of a large number of identical interactive elements [21,22]. The most familiar examples occur in ferromagnetic materials. In recent years the widespread and increasing capability of computers has made the modeling of hysteresis available to a much wider range of investigators and researchers. There are several studies for numerical analysis of hysteresis effects. The most popular models for hysteresis are Jiles-Atherton model [21,22] and Preisach model [32,33]. The Jiles-Atherton model is a statistical and mechanical model [21], which it is more suitable for the ferromagnetism in soft magnetic materials, such as electrical steel.

The Jiles-Atherton model for ferromagnetism is based on domain wall motion, including both bending and translation. The hysteresis-free (anhysteretic) magnetization curve [21] is described by

$$M_{an} = M_s \left(\coth \frac{H_e}{a} - \frac{a}{H_e} \right) \tag{3.1}$$

where M_{an} is anhysteretic magnetization (occurring when domain walls can move completely freely), M_s the fully saturated magnetization (one of parameters in Jiles-Atherton model)

shown in Figure 23, a is the domain density as a parameter of Jiles-Atherton model, and H_e is the effective magnetic field [21] defined as

$$H_e = H + \alpha M_{irr} . \tag{3.2}$$

H is an external magnetic field, M_{irr} is the irreversible component of a bulk magnetization of a material, and α is the coupling between domains (another parameter of Jiles-Atherton model). The anhysteretic magnetization represents the global energy state of the material if the domain walls move completely freely, but domain walls in general are pinned and bent in materials. If the bulk magnetization M is expressed as the sum of an irreversible component M_{irr} (due to domain-wall displacement) and a reversible component M_{rev} (due to domain-wall bending), then

$$M = M_{irr} + M_{rev} , \tag{3.3}$$

another parameter for the Jiles-Atherton model can be introduced by defining

$$M_{rev} = c(M_{an} - M_{irr}) \tag{3.4}$$

where c represents the reversibility of magnetization valued within the range of [0,1]. If $c = 0$, then the magnetization process in this material is completely irreversible [22]. On the other hand, the magnetization of a material can be completely reversible if $c = 1$. The irreversible magnetization changes can be obtained from an energy equation, in which the supplied energy is equal to magnetostatic energy changes and the hysteresis loss [22]

$$\mu_0 \int M_{an} \cdot dH_e = \mu_0 \int M_{irr} \cdot dH_e + \mu_0 \int k \frac{dM_{irr}}{dH_e} \cdot dH_e . \tag{3.5}$$

Consequently

$$M_{an} = M_{irr} + k\delta \frac{dM_{irr}}{dH_e} \tag{3.6}$$

where k the final parameter of the Jiles-Atherton model, which represents the pinning coefficient related to hysteresis loss, and δ is the switching parameter defined as

$$\delta = \begin{cases} +1 & \text{if } dH/dt > 0 \\ -1 & \text{if } dH/dt < 0 \end{cases}. \tag{3.7}$$

From Equation (3.6), the following the irreversible component of susceptibility with respect to an effective magnetic field was adapted for our MPI simulation on hysteresis:

$$\frac{dM_{irr}}{dH_e} = \frac{(M_{an} - M_{irr})}{k\delta}. \tag{3.8}$$

Preisach introduced a model for description of hysteresis [32,33]. This model was built up on some hypotheses concerning the mechanism of magnetization and the model used to describe behavior of magnetic hysteresis loops in ferromagnetic materials. The Preisach model is based on the assumption that a ferromagnetic material may be described by a system, which consists of very large number of elementary interacting fragments (volumes). Each fragment has an elementary rectangular hysteresis loop, which has two parameters: the coercive field of the free fragment h_C, and the interaction field between fragments h_M. It is convenient to introduce the switching field parameters h_A and h_B as

$$h_A = h_M + h_C, \text{ and } h_B = h_M - h_C, \tag{3.9}$$

where h_C is non-negative, so that h_A is always greater than or equal to h_B. The meaning of the switching fields is as follows:

(1) if the external magnetic field is increased to H_1, all fragments whose switching field h_A was lower or equal to the external field ($h_A \le H_1$) would switch their magnetization "up",

(2) if the external magnetic field is decreased to H_2, all fragments whose switching field h_B was higher or equal to the external field ($h_B \ge H_2$) would be switched "down", and

(3) all other fragments remain in their same state.

Let $\gamma(h_A, h_B)H(t)$ define the hysteresis operator which has the value of (+1) when (h_A, h_B) with an external magnetic field $H(t)$ at time t belongs to the case of (1) from the above descriptions, and which has the value of (–1) when (h_A, h_B) with $H(t)$ is in the case of (2). The Preisach function $P(h_A, h_B)$ is defined as a probability distribution function of the elementary fragments (volumes) with the switching fields h_A and h_B in the plane of the

Preisach variables h_A and h_B. According to the classical Preisach model [32,33] the total magnetization of the system with hysteresis is written as

$$M(t) = M_s \iint_{h_A \geq h_B} P(h_A, h_B)\gamma(h_A, h_B)H(t)dh_A dh_B \tag{3.10}$$

where M_s represents the saturated magnetization of specimen.

The Preisach model is more difficult than Jiles-Atherton model to implement a numerical simulation because for every time segment the double integration in Equation (3.10) must be computed for calculating magnetization for each element. Therefore, in this thesis, Jiles-Atherton model was adopted for the FEM implementation on hysteresis effects.

3.2. Application of FEM with Hysteresis

From equation (3.1), it is easily derived that

$$\frac{dM_{an}}{dH_e} = \frac{M_s}{a}\left(1 - \coth^2\frac{H_e}{a} + \left(\frac{a}{H_e}\right)^2\right) \tag{3.11}$$

Denoting B and B_e as magnetic flux density from the external magnetic filed and the bulk magnetization and effective magnetic flux from the effective magnetic field H_e, respectively, has the relationship as follows:

$$B = \mu_0(H + M) \text{ and } B_e = \mu_0 H_e. \tag{3.12}$$

From equations (3.2) and (3.12),

$$B = B_e + \mu_0 M - \alpha\mu_0 M_{irr}, \text{ so that}$$
$$\frac{dB}{dB_e} = 1 + \mu_0\frac{dM}{dB_e} - \alpha\mu_0\frac{dM_{irr}}{dB_e}. \tag{3.13}$$

Form equations (3.3) and (3.4),

$$\frac{dM}{dB_e} = (1-c)\frac{dM_{irr}}{dB_e} + c\frac{dM_{an}}{dB_e}. \tag{3.14}$$

Therefore, from (3.14), the equation (3.13) can be rewritten as

$$\frac{dB}{dB_e} = 1 + \mu_0(1-c-\alpha)\frac{dM_{irr}}{dB_e} + \mu_0 c\frac{dM_{an}}{dB_e}. \tag{3.15}$$

From (3.15) one can compute

$$\frac{dM}{dB_e} = \frac{dM}{dB}\frac{dB}{dB_e} = \frac{dM}{dB}\left\{1 + \mu_0(1-c-\alpha)\frac{dM_{irr}}{dB_e} + \mu_0 c\frac{dM_{an}}{dB_e}\right\} \tag{3.16}$$

For the calculation of the change of bulk magnetization with respect to the change of flux density can be easily derived from equations (3.14) and (3.16) as following

$$\frac{dM}{dB} = \frac{(1-c)\dfrac{dM_{irr}}{dB_e} + c\dfrac{dM_{an}}{dB_e}}{1 + (1-c-\alpha)\mu_0\dfrac{dM_{irr}}{dB_e} + c\mu_0\dfrac{dM_{an}}{dB_e}} \tag{3.17}$$

Since $dB_e/dH_e = \mu_0$, the equation (3.17) can be rewritten as

$$\frac{dM}{dB} = \frac{\dfrac{(1-c)}{\mu_0}\dfrac{dM_{irr}}{dH_e} + \dfrac{c}{\mu_0}\dfrac{dM_{an}}{dH_e}}{1 + (1-c-\alpha)\dfrac{dM_{irr}}{dH_e} + c\dfrac{dM_{an}}{dH_e}}. \tag{3.18}$$

The above equation represents the change of bulk magnetization with respect to the change of magnetic flux density. Since the magnetic flux density can be directly computed from the vector potential, the equation (3.18) is very essential for our MPI simulation algorithm on hysteresis effects.

Now, consider 2-D planar objects for an MPI simulation. Suppose there is a single electric current source, and the direction of current flow is perpendicular to the plane space. A current density is assumed as a function of time. With a small time elapse, the change of current flow only affects the strength of magnetic field, not the direction. When the applied external field is in the opposite direction of the current magnetization, the magnetization direction of a ferromagnetic material will be gradually changed to the opposite direction, so that the directional change of magnetization at each position always lies on individual one-dimensional axis. Therefore, one-dimensional Jiles-Atherton model can be extended to this

simple 2-D case. Once a unit vector of magnetization at each position is found, the strength of magnetization at the position is only updated by the equation (3.18), but the direction does not change at all as shown in Figure 24(a). The present MPI simulation package has been implemented to this situation only. Suppose there are two or more different current sources with individual time functions for the current flow. At any location in space of a problem, the external magnetic field can be changed not only in terms of its strength but also in its direction. In this case it is incorrect to apply the above equations to this situation. Figure 24(b) shows this case.

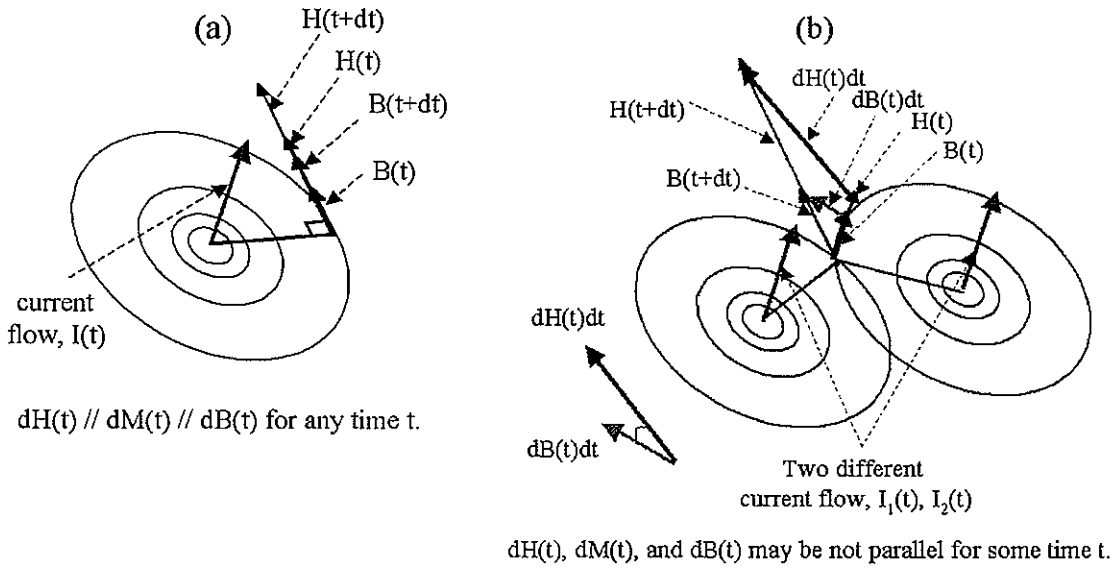

Figure 24. 2-D Maxwell problems with hysteresis effects: (a) a single current source, and (b) two different current sources with time varying

3.2.1. Algorithm for an Isotropic Model with Hysteresis Effects

For the development of an FEM algorithm with hysteresis effects, there are some restrictions to apply such that a test material must be isotropic, there is only a single source current field, and the current field must be either magnetostatic or quasi-magnetostatic. Consider a 2-D planar magnetic problem. Suppose the center of a planar test material is located at the origin of this 2-D Cartesian space, and the current field flows the normal to this plane passing through the origin. Let P(x,y) be an arbitrary position on the surface of this

material. Since the magnetic force to retain magnetic particles is toward the origin, it is important to compute the unit vector (**r**) at the position P(x,y) along the radial direction, which is defined as follows:

$$\mathbf{r} = \left(\frac{x}{\sqrt{x^2 + y^2}}, \frac{y}{\sqrt{x^2 + y^2}} \right)^T \tag{3.19}$$

In the hysteresis modeling, the magnetic force to attract the particles is highly related the overall magnetic field $\boldsymbol{H_{all}}$, which is yielded by not only the external magnetic field $\boldsymbol{H}$ but also the magnetized hysteresis materials, such that they have the following relationship

$$\nabla \times \vec{H}_{all} = \vec{J}_s + \nabla \times \vec{M} \ . \tag{3.20}$$

Therefore, the relative force density to the origin described in section 2.2.2 is redefined here as follows:

$$\begin{aligned} A_r &= \vec{H}_{all} \cdot \frac{\partial \vec{H}_{all}}{\partial r} = \vec{H}_{all} \cdot \left(\frac{\partial \vec{H}_{all}}{\partial x} \frac{\partial x}{\partial r} + \frac{\partial \vec{H}_{all}}{\partial y} \frac{\partial y}{\partial r} \right) \\ &= \vec{H}_{all} \cdot \left(\frac{\partial \vec{H}_{all}}{\partial x} \frac{x}{\sqrt{x^2 + y^2}} + \frac{\partial \vec{H}_{all}}{\partial y} \frac{y}{\sqrt{x^2 + y^2}} \right), \end{aligned} \tag{3.21}$$

where r represent the redial axis starting from the origin. The effective magnetic force to the origin is now defined as

$$F_r = \mu_0 \chi(\left|\vec{H}_e\right|) V_{MP} A_r . \tag{3.22}$$

The definitions of $R(\vec{H}_{all}, A_r)$, $T_{MPI}(\vec{H}_{all}, A_r)$, and $P_{MPI}(\vec{H}_{all}, A_r)$ are the same as mentioned in section 2.2.2.

Each finite element in MPI-FEM modeling with hysteresis contains the information of the direction and magnitude of magnetization, which is obtained by a starting external magnetic field with the initial nonlinear B(H) curve. After obtaining the unit vector of magnetization for each finite element, the MPI-FEM algorithm will update the magnitude of magnetization as the external magnetic field changes.

Technically, our MPI-FEM algorithm does not restrict the type of a wave function of a source current field over time. Figure 25 shows two examples of user-defined current density for the analysis of hysteresis effects. From Figure 25(a), our MPI-FEM algorithm

with hysteresis updates magnetization for each finite element by sampling N times of time intervals $[0, t_1)$, $[t_1', t_2)$, $[t_2, t_3)$, $[t_3', t_4]$, and $[t_4, t_5)$. At time t_i (i=1,2,3,4,5), our MPI simulation package reads the solution of magnetic fields, and MPI results. From Figure 25(b), the MPI simulation package took N time sampling for each time interval $[t_{i-1}, t_i)$ (i=1,2,3,4,5) to update magnetization for each finite element. At the beginning of time interval $[t_0, t_1]$ for both cases in Figure 25, the initial hysteresis loop looks like a nonlinear permeability B(H) curve. Therefore, in this time period, it is unnecessary to update magnetization N times, but it is required to solve the nonlinear problem with the initial nonlinear B(H) curve generated by the Jiles-Atherton model. The following section provides the algorithm for MPI-FEM with hysteresis.

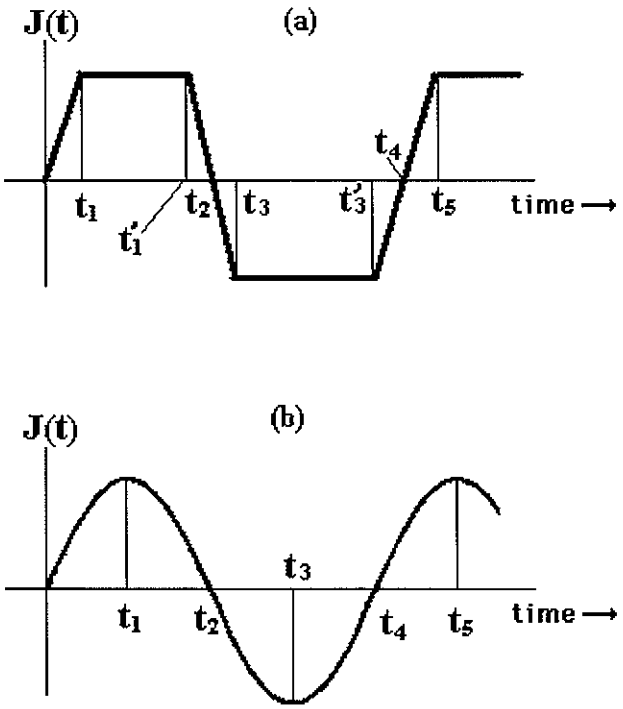

Figure 25. User-defined current density function: (a) for a magnetostatic case (b) for a quasi-magnetostatic case

3.3.2. Algorithm for MPI-FEM with Hysteresis

The following information must be prepared before applying MPI-FEM algorithm for hysteresis:

1. Hysteresis parameters (M_s, a, k, α, c) of the Jiles-Atherton model
2. Maximum current density: J_{max}.
3. Sampling scheme for a user-defined current density function as shown in Figure 25.

PHASE I: NONLINEAR PERMEABILITY REGION

Step 1) Build a B(H) table until it obtains fully saturated B-field for the initial hysteresis loop from the Jiles-Atherton model. Figure 26 shows an example of the initial hysteresis loop (However, the hysteresis shown in Figure 26 does not reached the condition of fully saturated B-field. It requires to generate more until the magnitude of magnetization reaches M_s).

Step 2) $\mathbf{J}(-\Delta t) = \mathbf{J}_{\max} - \Delta\mathbf{J}$. Solve $A(-\Delta t)$ such that $\frac{1}{\mu}\nabla\times\nabla\times\mathbf{A}(-\Delta t) = \mathbf{J}(-\Delta t)$, then

$$\mathbf{B}(-\Delta t) = \nabla\times\mathbf{A}(-\Delta t) \text{ and } \mathbf{M}(-\Delta t) = \mathbf{B}(-\Delta t)(1/\mu_0 - 1/\mu) \text{ for each finite element.}$$

Step 3) $J(0) = J_{max}$. Solve $A(t)$ such that $\frac{1}{\mu}\nabla\times\nabla\times\mathbf{A}(0) = \mathbf{J}(0)$, then for each finite element

$$\mathbf{B}(0) = \nabla\times\mathbf{A}(0),\ \Delta\mathbf{B}(0) = \mathbf{B}(0) - \mathbf{B}(-\Delta t)$$

$$\mathbf{M}(0) = \mathbf{B}(0)(1/\mu_0 - 1/\mu),\ \mathbf{H}(0) = \mathbf{B}(0)/\mu_0 - \mathbf{M}(0),$$

$$M_{an} = M_s\left(\coth\frac{H_e(-\Delta t)}{a} - \frac{a}{H_e(-\Delta t)}\right), \text{ and } M_{irr}(-\Delta t) = \frac{M(-\Delta t) - cM_{an}}{1-c},$$

where

$$H_e(-\Delta t) = H(-\Delta t) + \alpha M(-\Delta t).$$

Step 4) Compute the unit vector (**n**) of **M** for each finite element, and record it into the database of finite element. Save (**A**, **H**, **B**, **M**) for each finite element, and set $t = 0$. M(t) denotes the magnitude of magnetization (i.e., scalar value) in this thesis for convenience.

Step 5) Apply MPI-FEM algorithm described in section 2.3.1. Use the effect magnetic field in Equation (3.2) and the magnetic force in Equation (3.21).

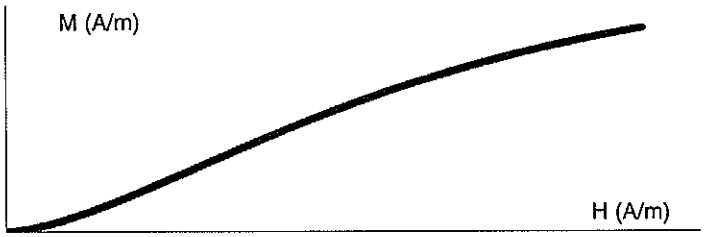

Figure 26. Phase I: the initial hysteresis loop of the Jiles-Atherton Model

PHASE II: THE FIRST ELIMINIATION OF EXTERNAL CURRENT FIELD

Step 1) Set $\delta = -1$ since $dH(t)/dt < 0$. Set $t = 0$.

Step 2) $\mathbf{J}(t+\Delta t) = \mathbf{J}(t) - \Delta\mathbf{J}(t)$. If $\mathbf{J}(t+\Delta t) < 0$, then go to (Step 4). Otherwise, update the magnetization as follows:

$$M(t+\Delta t) = M(t) + (dM/dB)\Delta B(t),$$

where

$$\frac{dM}{dB} = \frac{\frac{(1-c)}{\mu_0}\frac{dM_{irr}}{dH_e} + \frac{c}{\mu_0}\frac{dM_{an}}{dH_e}}{1+(1-c-\alpha)\frac{dM_{irr}}{dH_e} + c\frac{dM_{an}}{dH_e}},$$

$$\frac{dM_{an}}{dH_e} = \frac{M_s}{a}\left(1-\coth^2\frac{H_e(t)}{a} + \left(\frac{a}{H_e(t)}\right)^2\right),$$

$$\frac{dM_{irr}}{dH_e} = \frac{(M_{an} - M_{irr}(t))}{k\delta},$$

$$M_{irr}(t) = \frac{M(t) - cM_{an}}{1-c},$$

$$M_{an} = M_s\left(\coth\frac{H_e(t)}{a} - \frac{a}{H_e(t)}\right), \text{ and}$$

$$H_e(t) = H(t) + \alpha M_{irr}(t-\Delta t).$$

Step 3) Compute $J'(t+\Delta t) = J(t+\Delta t) + \left|\nabla\times\mathbf{M}(t+\Delta t)\right|_z$.

Solve $A(t+\Delta t)$ for a linear PDE problem, $\frac{1}{\mu_0}\nabla\times\nabla\times A(t+1)=J'(t+1)$.

From the vector potential $A(t+\Delta t)$, compute $B(t+\Delta t)$, $\Delta B(t+\Delta t)$, and $H(t+\Delta t)$. Save (**A**, **H**, **B**, **M**), and let $t = t+\Delta t$. For the MPI test, every finite element, which has retained magnetic particles, must be verified by the $T_{MPI}(\vec{H}_{all}, A_r)$ test to keep them. Go to (Step 1).

Step 4) Exit the (Phase II) and go to the (Phase III).

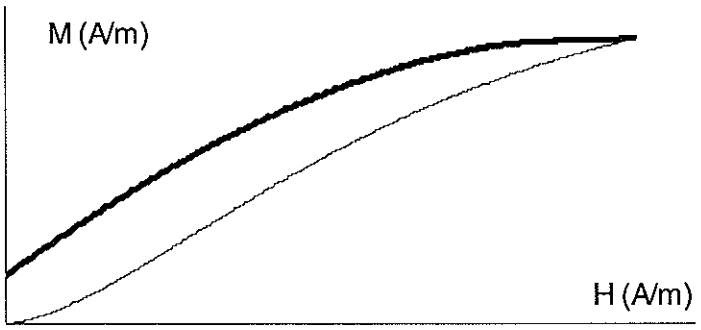

Figure 27. Phase II: the first elimination of external current field

PHASE III: DECREASE EXTERNAL CURRENT FIELD TO NEGATIVE DIRECTION

Step 1) $\mathbf{J}(t+\Delta t)=\mathbf{J}(t)-\Delta\mathbf{J}(t)$. If $\mathbf{J}(t+\Delta t)<0$, then go to (Step 3). Otherwise, update the magnetization as follows:

$$M(t+\Delta t)=M(t)+(dM/dB)\Delta B(t).$$

Step 2) Compute $J'(t+\Delta t)=J(t+\Delta t)+\left|\nabla\times\mathbf{M}(t+\Delta t)\right|_z$.

Solve $A(t+\Delta t)$ for a linear PDE problem, $\frac{1}{\mu_0}\nabla\times\nabla\times A(t+1)=J'(t+1)$.

From the vector potential $A(t+\Delta t)$, compute $B(t+\Delta t)$, $\Delta B(t+\Delta t)$, and $H(t+\Delta t)$. Save (**A**, **H**, **B**, **M**), and let $t = t+\Delta t$. For MPI test, every finite element, which does not have magnetic particles, must be verified by the $T_{MPI}(\vec{H}_{all}, A_r)$ test to retain them. Go to (Step 1).

Step 3) Exit the (Phase III) and go to the (Phase IV).

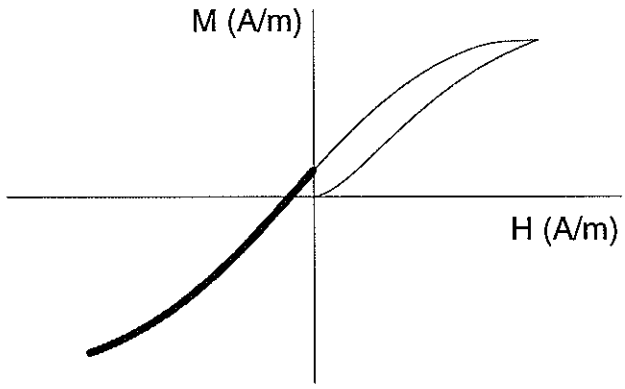

Figure 28. Phase III: decrease external current field to negative direction

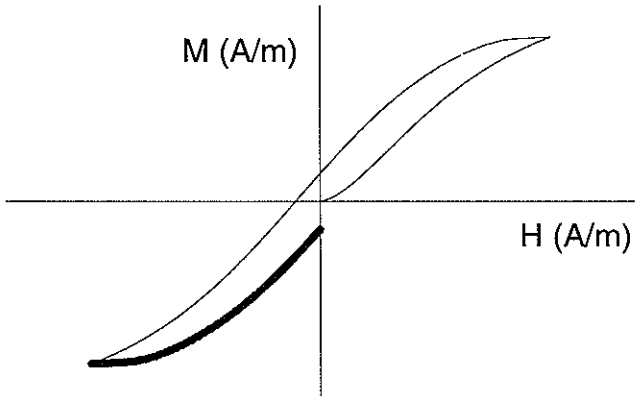

Figure 29. Phase IV: the second elimination of external current field

PHASE IV: THE SECOND ELIMINIATION OF EXTERNAL CURRENT FIELD

Step 1) Set $\delta = +1$ since $dH(t)/dt > 0$.

Step 2) $\mathbf{J}(t+\Delta t) = \mathbf{J}(t) + \Delta\mathbf{J}(t)$. If $\mathbf{J}(t+\Delta t) > 0$, then go to (Step 4). Otherwise, update the magnetization as follows:

$$M(t+\Delta t) = M(t) + (dM/dB)\Delta B(t).$$

Step 3) Compute $J'(t+\Delta t) = J(t+\Delta t) + \left|\nabla \times \mathbf{M}(t+\Delta t)\right|_z$.

Solve $A(t+\Delta t)$ for a linear PDE problem, $\frac{1}{\mu_0}\nabla \times \nabla \times A(t+1) = J'(t+1)$.

From the vector potential $A(t+\Delta t)$, compute $B(t+\Delta t)$, $\Delta B(t+\Delta t)$, and $H(t+\Delta t)$. Save (**A**, **H**, **B**, **M**), and let $t = t+\Delta t$. For the MPI test, every finite element, which has retained magnetic particles, must be verified by the $T_{MPI}(\vec{H}_{all}, A_r)$ test to keep them. Go to (Step 2).

Step 4) Exit the (Phase IV) and go to the (Phase V).

PHASE V: INCREASE EXTERNAL CURRENT FIELD TO POSITIVE DIRECTION

Step 1) $\mathbf{J}(t+\Delta t) = \mathbf{J}(t) + \Delta\mathbf{J}(t)$. If $\mathbf{J}(t+\Delta t) \geq \mathbf{J}_{\max}$, then go to (Step 3). Otherwise, update the magnetization as follows:

$$M(t+\Delta t) = M(t) + (dM/dB)\Delta B(t).$$

Step 2) Compute $J'(t+\Delta t) = J(t+\Delta t) + \left|\nabla \times \mathbf{M}(t+\Delta t)\right|_z$.

Solve $A(t+\Delta t)$ for a linear PDE problem, $\frac{1}{\mu_0}\nabla \times \nabla \times A(t+1) = J'(t+1)$.

From the vector potential $A(t+\Delta t)$, compute $B(t+\Delta t)$, $\Delta B(t+\Delta t)$, and $H(t+\Delta t)$. Save (**A**, **H**, **B**, **M**), and let $t = t+\Delta t$. For MPI test, every finite element, which does not have magnetic particles, must be verified by the $T_{MPI}(\vec{H}_{all}, A_r)$ test to retain them. Go to (Step 1).

Step 3) Terminate the whole procedure of MPI-FEM algorithm with hysteresis.

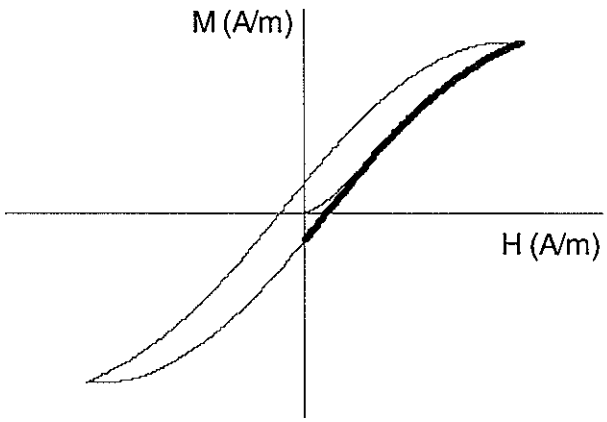

Figure 30. Phase V: increase external current field to positive direction

3.3. Experimental Design for MPI Simulations with Hysteresis

A cylinderal material was used for the test of hysteresis effects as shown in Figure 31. Figure 31 shows the cross sectional view of the cylinder shape of test material that has six different sizes of longitude defects. Since the directions of defects are all parallel to longitude of this test material, the 2-D planar space is adequate for this problem (any magnetic filed generated by a solenoid system cannot detect these defects since the position of defect and the direction of magnetic fields are parallel).

This material has hysteresis properties as shown in Figure 32. The light cross marks in Figure 32 indicate the real experimental data, and black boxes indicate an estimated hysteresis loop from the Jiles-Atherton model. The five parameters for the Jiles-Atherton hysteresis model have been found by trial-and-errors as shown in Figure 32.

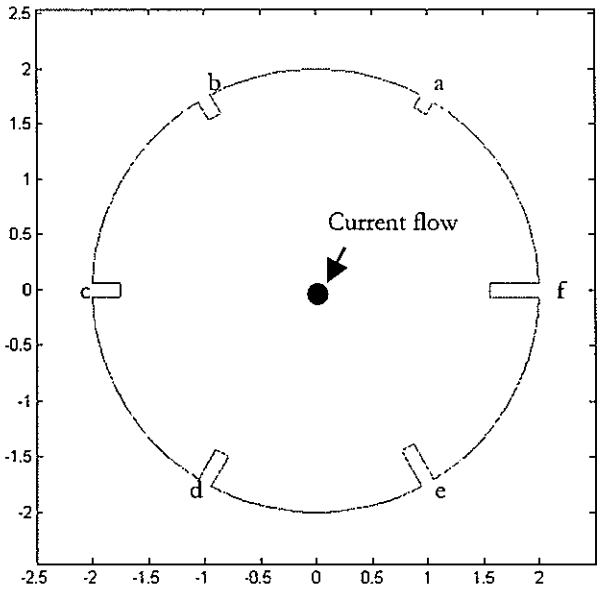

Artificial Defects: a ~ f
a : 1/16" width x 1/16" depth
b : 1/16" width x 2/16" depth
c : 1/16" width x 3/16" depth
d : 1/16" width x 4/16" depth
e : 1/16" width x 5/16" depth
f : 1/16" width x 6/16" depth

Figure 31. Geometry of a test material with six artificial defects: The current flows at the center of this material

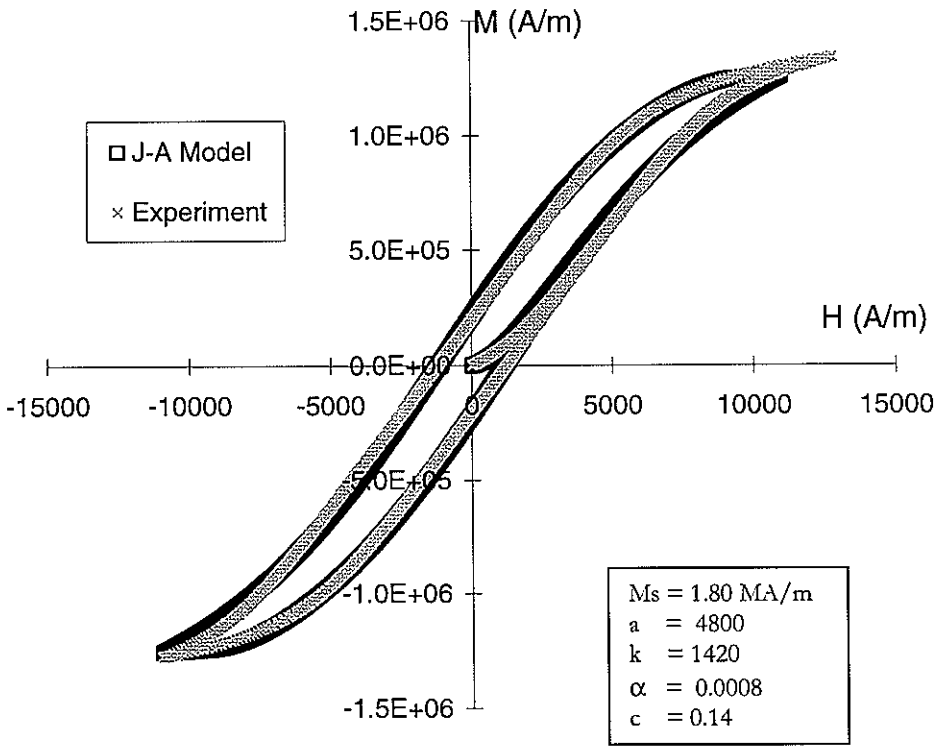

Figure 32. Find the five parameters of the Jiles-Atherton Model from experimental hysteresis loop of the test material as shown in Figure 31

3.4. Simulation Results from MPI-FEM Algorithm with Hysteresis

The applying DC current field has been set up as shown in Figure 25(a). Figure 33 shows the five steps of phases described in section 3.2.2. Figure 33(a) shows the magnetic flux leakage around defect sites. In Figure 33(b) to 33(f), the gray colored meshes indicated retained magnetic particles. Retained Magnetic particles shown in Figure 33(b) to 33(f) were obtained at the end step for each phase procedure of MPI-FEM algorithm (see Figure 26 to 30). For Figure 33(c) and 33(e), there are some magnetic forces due to existing remanent magnetization so that it may keep retained magnetic particles even if the external magnetic fields were removed. At the smallest defect all magnetic particles were removed since the magnetic force for the particles is less than their gravitational forces.

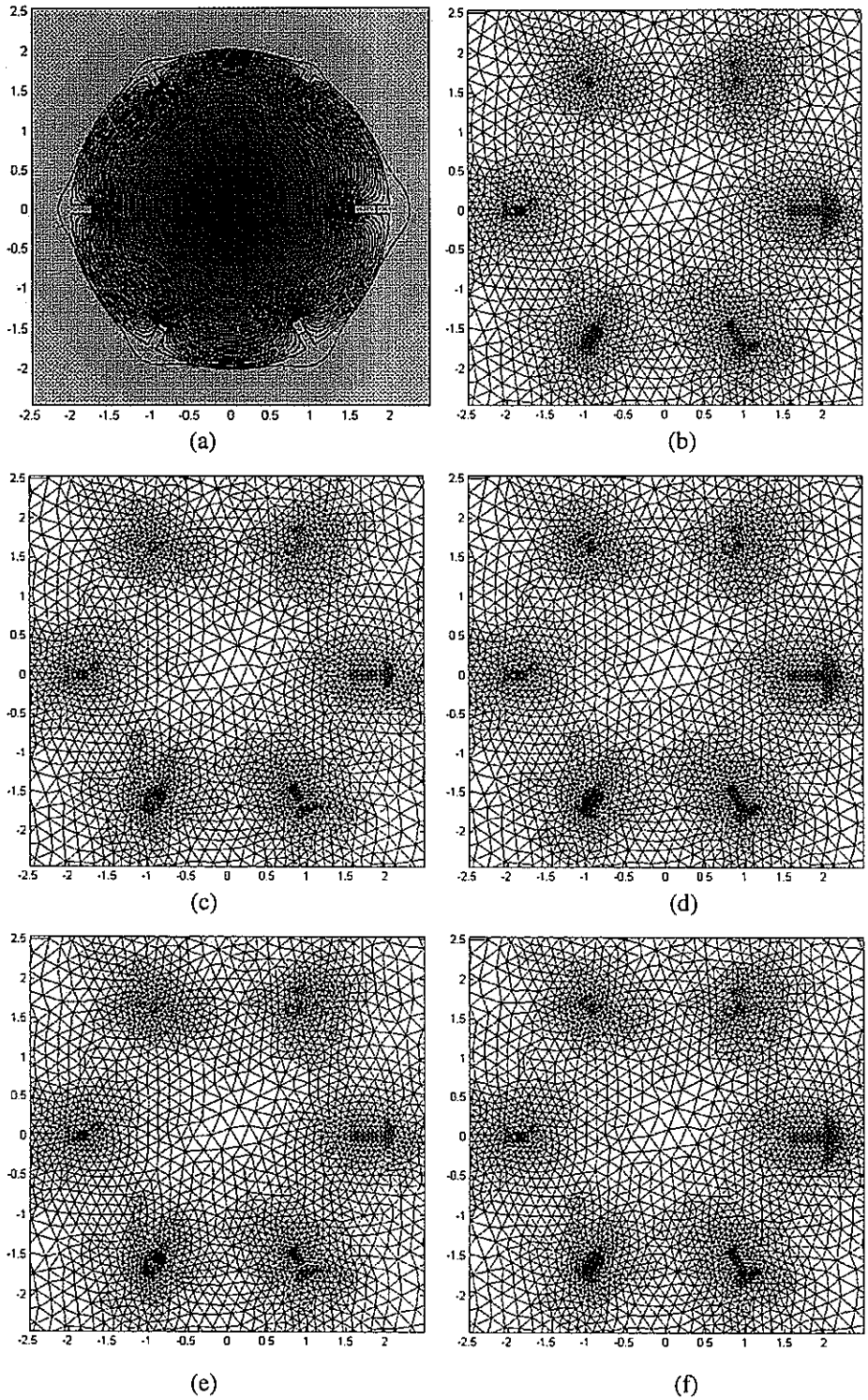

Figure 33. Simulation results of MPI-FEM algorithm with hysteresis effects on DC current fields as shown in Figure 25(a): (a) magnetic flux contour lines without magnetic particles at the initial magnetization, (b) magnetic particles at the initial magnetization, (c) magnetic particles after the first elimination of external fields, (d) magnetic particles after decreasing external fields to the negative direction, (e) magnetic particles after the first elimination of external fields, and (f) magnetic particles after recovering external fields to the original

3.5. Summary

Maxwell 2D problems (for axisymmetric or planar coordinate) have been implemented in this thesis for hysteresis materials with a single DC current source. An MPI-FEM algorithm for hysteresis materials has been developed for the estimation of the volume and distribution of retained magnetic particles around a defect site by magnetic forces against the gravitation of the particles.

The volume of retained magnetic particles depends on not only the current source strength but also the curl of magnetization strength of a hysteretic material. Since these are vectors so that they may have different directions, the distribution of magnetic particles may be influenced by the switching pattern of DC currents or the manipulation of AC power, the hysteresis material properties, and location and geometry of defects.

In this thesis we do not consider about the influence or effective change of temperature caused by hysteresis energy loss. Also we do not consider about multiple field sources to make more complex magnetic flux fields around defect sites to read more informative measures. However, with only single current source field, the MPI simulation problem is very complex to characterize the behavior of magnetic particles. There are a lot of works to identify the relationship between parameters of the Jiles-Atherton hysteresis model and the geometry and position of defects. Since the five parameters of the Jiles-Atherton hysteresis model were obtained by trial-and-errors, a sensitivity analysis of these parameters and MPI simulation results should be significantly considered. Also, the quality of mesh size also affects the estimated volume of magnetic particles. Therefore, these considerations can be further research to improve the reliability of MPI simulation software package.

CHAPTER 4.

CONCLUSION AND DISCUSSION

4.1. Conclusion and Summary

We demonstrated the sensitivity analysis of MPI simulations under the assumption of material properties such as reversible nonlinear permeability or irreversible hysteresis permeability. For the case of reversible nonlinear permeability, the estimated volume of magnetic particles is dependent upon the quality of mesh (i.e., the shapes and sizes of meshes) and the applied current fields. On the contrary, for the case of irreversible hysteresis materials, it depends on not only the above two cases but also the measurement of domain coupling. Even though the importance of the domain coupling property in MPI simulation is very critical, it is very hard to estimate the correct value of this parameter. Therefore, a sensitivity analysis of not only the size of a defect but also the range of domain coupling should be accomplished to characterize the reliability of our MPI simulation package.

Our MPI simulation software package will allow nondestructive test engineers to understand the effect of all parameters in the MPI test as well as allow a user to quickly optimize an inspection while minimizing the need for experiments. The software will also help users control the quality of an MPI test, i.e., sensitivity of magnetic particle clusters vs. defect geometries on a test material. The software package may be used to answer difficult standards related complicated magnetic questions.

4.2. Discussion

Our MPI simulation package was limited to the use of only single current source. If a user wants to use multiple field sources so that it may improve the detectability of very complicate or delicate defects, it is essential to update the current MPI-FEM algorithm with hysteresis effects. Also, the extension of MPI simulations for 3-dimensional objects can be considered as a future works.

Also, the quality of mesh size also affects the estimated volume of magnetic particles. Therefore, it is very simple and possible to find the relationship between the number of meshes and the estimated volume of magnetic particles around a particular geometry of a defect. Then, it will give us some information of the confidential limit or reliability of the estimate volume of retained magnetic particles as a function of the number of meshes or the average size of meshes around a defect site.

There are a lot of future works to determine or predict the relationship between parameters of the Jiles-Atherton hysteresis model and the geometry and position of defects. Since the five parameters of the Jiles-Atherton hysteresis model were obtained by trial-and-errors in real situations, a sensitivity analysis of these parameters and MPI simulation results should be significantly considered to verify our simulation result with respect to real experimental analysis.

REFERENCES

[1] Clark, W. G. and Junker, W. R., "Problems in the eddy current characterization of temper embrittlement," *Material Evaluation,* **43**, 1985, pp. 1546-1552.

[2] R. Grimberg, A. Savin, E. Radu, and S. M. Chifan, "Eddy current sensor for holographic visualization of material discontinuities," *Sensor Actuators A,* **81,** 2000, pp. 251-253.

[3] Hastings, C. H., "Recording magnetic detector locates flaws in ferrous metals," *Product Engineering*, **18**(4), 1947, pp. 110-112.

[4] D. L. Atherton, "Stress-shadow magnetic inspection technique for far-side anomalies in steel pipe," *NDT International*, **16**(3), 1983, p. 145.

[5] Tiitto, S., "On the influence of microstructure on magnetization transitions in steel," *Acta Polytechnica Scand. in Applied Physics Series*, **119**, 1977, p. 80.

[6] O. Sundström and K. Törrönen, "The use of Barkhausen noise analysis in nondestructive testing," *Material Evaluation,* **37**(3), 1979, pp. 51-56.

[7] Betz, C. E., *Principles of Magnetic Particle Testing*, Magnaflux Corporation, Hardwood Heights, Illinois, 1997.

[8] Lovejoy, D., *Magnetic Particle Inspection: A Practical Guide*, Chapman & Hall, London, 1993.

[9] Edwards, C. and Palmer, S. B., "The magnetic leakage field of surface-breaking cracks," *Journal of Physics D: Applied Physics*, **19**, 1986, pp. 657-673.

[10] Z. Zeng, L. Xuan, L. Upda, and S. Upda, "Modeling of current excitation waveforms for magnetic particle inspection," *QNDE*, D. O. Thompson, Ed., Plenum, New York, **21B**, 2002, pp. 1984—1990.

[11] L. Udpa, S. Manadayam, S. Udpa, Y. Sun, and W. Lord, "Developments in gas pipeline inspection technology," *Material Evaluation*, **54**(4), 1996, pp. 467-472.

[12] S. Mandayam, L. Udpa, S. Udpa, and W. Lord, "Invariance transformations for magnetic flux leakage signals," IEEE Transactions on Magnetics, **32**(3), 1996, pp. 1577-1580.

[13] Jiles, D. C., "Review of magnetic methods for nondestructive evaluation (Part 2)," *NDT International,* **23**(2), 1990.

[14] W. A. K. Deutsch, R. Wagner, W. Weber, "Reproducible Production of Magnetic Power Crack Detection Agents," *NDT.net* (*e-Journal of Nondestructive Testing*, www.ndt.net), Vol. 7, No. 3, March 2002.

[15] J. Y. Lee, S. J. Lee, D. C. Jiles, M. Garton, R. Lopez, and L. Brasche, "Development of modeling and simulation for magnetic particle inspection using finite elements," *Review of Quantitative Nondestructive Evaluation*, Ed. by D.O. Thompson and D.E. Chimenti, **22**(915), 2003, under the process.

[16] J. Y. Lee, S. J. Lee, D. C. Jiles, M. Garton, R. Lopez, and L. Brasche, "Sensitivity analysis of simulations for magnetic particle inspection using finite element method," accepted for publication in *IEEE Transations on Magnetics*, 2003.

[17] Flex Support, *Theoretical Description of the EMFlex Finite Element Formulation*, available at URL: *http://www.wai.com/AppliedScience/Software/Emflex/index-em.html*, Weidlinger Associates, Inc., 1991.

[18] D. Meeker, *Finite Element Method Magnetics*, URL: http://femm.berlios.de/, 1999.

[19] P. P. Silvester and R. L. Ferrari, *Finite elements for electrical engineers, 3rd Ed*, Cambridge University Press, 1996.

[20] The MathWorks, Inc., *Partial differential equation toolbox user's guide*, February 1996.

[21] D.C. Jiles and D.L. Atherton, "Theory of Ferromagnetic Hysteresis," *Journal of Magnetism and Magnetic Materials*, **61**, 1986, pp. 48-60.

[22] D. C. Jiles, *Magnetism and Magnetic Materials, 2nd ed.*, Chapman & Hall, New York, 1998.

[23] E. Kreyszig, *Advanced engineering mathematics, Vol. I, 6th Ed.*, John Wiley & Sons, 1986.

[24] J. Ruppert, "A Delaunay refinement algorithm for quality 2-dimensional mesh generation," *Journal of Algorithms*, **18**, 1995, pp. 548-585.

[25] J. Schewchuk, "Tetrahedral mesh generation by Delaunay refinement," *Proceedings of the 14th Annual Symposium on Computational Geometry*, June 1998.

[26] S. J. Lee, J. M. Kenkel, and D. C. Jiles, "Magnetic FEM course modules and demonstrations," *Final Report*, March 2001.

[27] ANSOFT Co., *Advanced multiphysics analysis capability for electromechanical design*, Pittsburgh, PA, March 15, 2001.

[28] Palanisamy, R., *Finite Element Modeling of Eddy Current Nondestructive Testing Phenomena,* Ph.D. Thesis, Colorado State University, 1980.

[29] L. J. Schwarzendruber, *Proceedings of 12th Symposium of Nondestructive Evaluation*, San Antonio, TX, 1979, Ed., W. W. Bradshaw, pp. 150-162.

[30] A. Papoulis, *Probability, Random Variables, and Stochastic Processes, 3rd Ed.*, McGraw-Hill, Inc., 1991.

[31] Hugh D. Young, *University Physics, 8th Ed.*, Addison-Wesley, 1992.

[32] G. Friedman, "Conditions for the representation of vector hysteresis by the vector Preisach model," *Journal of Applied Physics*, **85**(8) 1999, pp. 4379-4381.

[33] I. Tomáš, Ye. Y. Melikhov, J. Kadlecová, O. V. Perevertov, "Preisach model of magnetic hysteresis for ENDE", *Electromagnetic Nondestructive Evaluation (IV)*, S. S. Udpa et al. (Eds.), IOS Press, 2000, pp. 120-126.

APPENDIX A

LIST OF SYMBOLS

Symbol	Quantity	Unit	Conversion
A	Magnetic vector potential	A	
A_r	Product of magnetic field and its gradient along radial direction ($\mathbf{H} \cdot \partial \mathbf{H} / \partial r$)	A^2/m^3	
A_z	Product of magnetic field and its gradient along axial direction ($\mathbf{H} \cdot \partial \mathbf{H} / \partial z$)	A^2/m^3	
a	Domain density in hysteresis equation		
α	Domain coupling in hysteresis equation		
B	Magnetic flux density	Tesla/Gauss	1 tesla = 10^4 gauss
c	Reversibility in hysteresis equation		
χ	Susceptibility of materilas		
D	Electric flux density (or displacement)		
D	Diameter of Solenoid	m	1 m = 1000 mm
d	diameter	mm	1 m = 1000 mm
ε	Permittivity		
ε_0	Permittivity of free space	F/m	8.854×10^{-12}F/m
F_g	Gravitational force	N	

Symbol	Quantity	Unit	Conversion
F_{resist}	Resistance force against magnetic force		
F_r	Magnetic force along radial direction	N	
F_z	Magnetic force along axial direction	N	
$\boldsymbol{H}$	Electric field intensity	(A/m)/Oe	1 Oe = 79.58 A/m
$\boldsymbol{H_c}$	Coercivity	(A/m)/Oe	1 Oe = 79.58 A/m
$\boldsymbol{H_{eff}}$	Effective magnetization	(A/m)/Oe	1 Oe = 79.58 A/m
i	Current	A	Ampere
$\boldsymbol{J}$	Current density	A/m^2	1 A/mm^2=1 MA/m^2
$\boldsymbol{J_s}$	Current density of a source coil	A/m^2	
k	Pinning coefficient in hysteresis equation		
L	Length of solenoid	m	1 m = 1000 mm
M_{an}	Anhysteretic magnetization	(A/m)/Oe	1 Oe = 79.58 A/m
M_s	Saturated Magnetization in hysteresis equation	(A/m)/Oe	1 Oe = 79.58 A/m
N	Number of turns of solenoid coil		
μ	Permeability of materials	tesla·m/A	
μ_0	Permeability of empty space	tesla·m/A	1.257×10^{-6} tesla·m/A

Symbol	Quantity	Unit	Conversion
$\mu_0 A_r$	Force density without consideration of the susceptibility along radial direction	N/m^3	1 N/m^3=1 tesla·A/m
$\mu_0 A_z$	Force density without consideration of the susceptibility along radial direction	N/m^3	1 N/m^3=1 tesla·A/m
ω	Angular frequency	Hz	1Hz = 1cycle/sec
P_{MPI}	Probability of magnetic particle existence		
φ	Magnetic flux	Weber	1 weber = 1 tesla·m^2
ρ	Resistivity (or, electric charge density)		
ρ_m	Mass density of liquid magnetic paricle	kg/m^3	
ρ_w	Mass density of water	kg/m^3	1000 kg/m^3
σ	Conductivity		
V_{MPI}	Volume of retained magnetic particles	mm^3	1 mm^3=10^{-9} m^3
W	Energy	J	
W_M	Magnetostatic energy	J	

APPENDIX B

ASSEMBLING MAXWELL'S EQUATIONS WITH FEM

If $c(x) \geq \delta > 0$, $a(x) \geq 0$ and $q(x) \geq 0$ with $q(x) > 0$ on some part of $\partial\Omega$ [19], then,

$$U^T(K+M+Q)U = \int_\Omega \left(c|\nabla u|^2 + au^2\right)dx + \int_{\partial\Omega} qu^2 ds > 0, \quad if\ U \neq 0, \tag{B.1}$$

where, $U^T(K+M+Q)U$ is the *energy norm*. There are many choices of the test-function spaces. Piecewise linearity on each triangle of the mesh guarantees that the integrals defining the stiffness matrix K exist. Projection onto V_{N_p} is no more than linear interpolation, and the evaluation of the solution inside a triangle is done just in terms of the nodal values. If the mesh is uniformly refined, V_{N_p} approximates the set of smooth functions on Ω.

A suitable basis $\{\phi_i(x)\}$ for V_{N_p} can be selected by setting $\phi_i(x)$ to be the value 1 only where the node is x_i; otherwise, the value 0 is taken at any other nodes except x_i. That is, a suitable basis $\{\phi_i(x)\}$ can be designed for activating only one for each finite element. Then, it yields

$$u(x_i) = \sum_{j=1}^{N_p} U_j \phi_j(x_i) = U_i, \tag{B.2}$$

Finally note that the basis function ϕ_i vanishes on all the triangles that do not contain the node x_i. The immediate consequence is that the integrals appearing in K_{ij}, M_{ij}, Q_{ij}, F_i and G_i only need to be computed on the triangles that contain the node x_i. Also, it means that K_{ij} and M_{ij} are zero unless x_i and x_j are vertices of the same triangle and thus K and M are very sparse matrices. Their sparse structure depends on the ordering of the indices of the mesh points.

The integrals in the FEM matrices are computed by adding the contributions from each triangle to the corresponding entries (i.e., only if the corresponding mesh point is a vertex of the triangle). This process is known as "*assembling*". The assembling routines scan the triangles of the mesh. For each triangle the assembling routines compute the local

matrices[3] and add their components to the correct positions in the sparse matrices or vectors. The integrals are computed using the mid-point rule. This approximation is optimal since it has the same order of accuracy as the piecewise linear interpolation. Consider a triangle given by the nodes P_1, P_2, and P_3 as in Figure B.1.

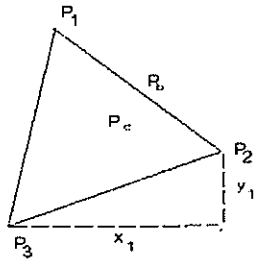

Figure B1. The local triangle $\Delta P_1P_2P_3$

The simplest computations are for the local mass matrix M:

$$m_{ij} = \int_{\Delta P_1P_2P_3} m(P_c)\phi_j(x)\phi_i(x)dx = m(P_c)\frac{area(\Delta P_1P_2P_3)}{12}(1+\delta_{ij}), \tag{B.3}$$

where P_c is the center of mass of $\Delta P_1P_2P_3$, i.e.,

$$P_c = \frac{P_1+P_2+P_3}{3}. \tag{B.4}$$

The contribution to the right-hand side F is just

$$f_i = f(P_c)\frac{area(\Delta P_1P_2P_3)}{3}. \tag{B.5}$$

For the local stiffness matrix we have to evaluate the gradients of the basis functions that do not vanish on $\Delta P_1P_2P_3$. Since the basis functions are linear on the triangle $\Delta P_1P_2P_3$, the gradients are constants. Denote the basis functions ϕ_1, ϕ_2, and ϕ_3 such that $\phi_i(P_i) = 1$. If $P_2–P_3 = [x_1, y_1]^T$ then we have

[3] The local 3-by-3 matrices contain the integrals evaluated only on the current triangle. The coefficients are assumed constant on the triangle and they are evaluated only in the triangle center.

$$\nabla\phi_1 = \frac{1}{2area(\Delta P_1P_2P_3)}\begin{bmatrix} y_1 \\ -x_1 \end{bmatrix}, \tag{B.6}$$

and after integration (taking c as a constant matrix on the triangle)

$$k_{ij} = \frac{1}{4area(\Delta P_1P_2P_3)}\begin{bmatrix} y_1 & -x_1 \end{bmatrix} s(P_c) \begin{bmatrix} y_1 \\ -x_1 \end{bmatrix}. \tag{B.7}$$

If two vertices of the triangle lie on the boundary, they contribute to the line integrals associated to the boundary conditions. If the two boundary points are P_1 and P_2, then we have

$$Q_{ij} = q(P_b)\frac{\|P_1 - P_2\|}{6}(1+\delta_{ij}), \quad i,j,=1,2, \tag{B.8}$$

and

$$G_i = g(P_b)\frac{\|P_1 - P_2\|}{2}, \quad i,j,=1,2, \tag{B.9}$$

where P_b is the mid-point of P_1P_2.

For each triangle the vertices P_m of the local triangle correspond to the indices i_m of the mesh points. The contributions of the individual triangle are added to the matrices such that, e.g.,

$$K_{i_m,i_n}(new) \leftarrow K_{i_m,i_n}(old) + k_{mm}, \quad m,n=1,2,3. \tag{B.10}$$

APPENDIX C.

COPIES OF PUBLICATIONS FROM THIS RESEARCH

J. Y. Lee, S. J. Lee, D. C. Jiles, M. Garton, R. Lopez, and L. Brasche, "Sensitivity analysis of simulations for magnetic particle inspection using finite element method," accepted for publication in *IEEE Transations on Magnetics* (2003).

J. Y. Lee, S. J. Lee, D. C. Jiles, M. Garton, R. Lopez, and L. Brasche, "Development of modeling and simulation for magnetic particle inspection using finite elements," *Review of Quantitative Nondestructive Evaluation*, vol. 22, 915 (2003), ed. by D.O. Thompson and D.E. Chimenti.

These works were supported in part by the Federal Aviation Administration under Contract #DTFA03-98-D-00008, Delivery Order #IA051 at Iowa State University's Center for NDE as part of the Center for Aviation Systems Reliability. J. Y. Lee is with the Electrical and Computer Engineering Department (telephone: 515-294-5385, e-mail: jylee@ iastate.edu), S. J. Lee is with Ames Laboratory, D. C. Jiles is with the Material Science & Engineering Department; M. Garton, R. Lopez, and L. Brasche are with the Center for Aviation Systems Reliability. All are at Iowa State University, Ames, Iowa 50011, USA.

Sensitivity Analysis of Simulations for Magnetic Particle Inspection using Finite Element Method

J. Y. Lee, S. J. Lee, D. C. Jiles, *Fellow, IEEE*

M. Garton, R. Lopez, and L. Brasche

Abstract-- Magnetic particle inspection is widely used for nondestructive evaluation in aerospace applications in which interpretation of inspection results is currently limited to empirical knowledge and experience-based approaches. Advances in computational magnetics, particularly the use of finite element calculations, have enabled realistic numerical simulations of magnetic particle inspection to be undertaken with complicated geometries. In this paper we report a sensitivity analysis using finite element method simulations of magnetic particle inspection for defects with various sizes and geometries. As a result, improved quantitative understanding of the MPI technique and factors that affects its sensitivity and reliability has been achieved. These results can be used to optimize conditions for conducting these inspections and should lead to improvement in analysis and interpretation of experimental results.

Index Terms-- **Finite element method, Magnetic particle inspection, Sensitivity analysis, Nondestructive evaluation.**

INTRODUCTION

A number of nondestructive evaluation (NDE) techniques have been developed for evaluating defects in materials; including surface discontinuities, voids, surface flaws, and cracks on the surface or in the body of materials [1-4]. NDE techniques, when properly applied, prevent unexpected operational failures of the mechanical parts by locating critical defects and allowing remediation before failure occurs. Different NDE techniques should be used depending on whether the materials are magnetic or non-magnetic. For magnetic materials, eddy current [1], magnetic flux leakage [2], magnetic Barkhausen noise [3], and magnetic particle inspection [4] techniques can be employed. Magnetic particle inspection (MPI) is widely used for nondestructive evaluation in aerospace applications, with current inspection methods being essentially limited to empirical or experience-based approaches [4]. Better quantitative understanding of the MPI technique and factors that affect its sensitivity and reliability contribute not only to reductions in inspection cost and time but also to improvement of analysis of experimental data and ultimately to improvements in design.

The magnetic field generator and the magnetic powder particles are essential components of the MPI

Manuscript received December 27, 2002. This work was supported in part by the Federal Aviation Administration under Contract #DTFA03-98-D-00008, Delivery Order #IA051 at Iowa State University's Center for NDE as part of the Center for Aviation Systems Reliability. J. Y. Lee is with the Electrical and Computer Engineering Department (telephone: 515-294-5385, e-mail: jylee@iastate.edu), S. J. Lee is with Ames Laboratory, D. C. Jiles is with the Material Science & Engineering Department; M. Garton, R. Lopez, and L. Brasche are with the Center for Aviation Systems Reliability. All are at Iowa State University, Ames, Iowa 50011, USA.

method. The magnetic force, which causes the magnetic particles to adhere to the defect sites, is proportional to the magnetic field gradient. The distortion of the magnetic field is greatest when the direction of the magnetic field is perpendicular to the axis of a defect, which maximizes the magnitude of the magnetic field gradient. The magnetic properties of the magnetic particles are also critical factors in MPI testing.

Computational advances have allowed numerical simulations of MPI to be performed for complicated geometries [5]. In this paper, we report the use of the finite element method (FEM) numerical simulations of MPI for defects with various sizes. The results provide indications of the expected behavior of magnetic particles around a defect and the viability of magnetic particle inspection under a variety of different conditions.

Finite Element Numerical Simulations

Equations for an Axisymmetric Geometry

We simulated a test sample in the shape of a cylindrical tube by solving Maxwell's equations in a cylindrical coordinate system (r, θ, z). Figure 1 shows the geometry of the solenoidal MPI simulation used in the FEM calculations. For axisymmetric geometry, the equation for Ampére's law under dc conditions is

$$\frac{1}{\mu}\left(\frac{\partial^2 \overline{A}}{\partial r^2}+\frac{1}{r}\frac{\partial \overline{A}}{\partial r}+\frac{\partial^2 \overline{A}}{\partial z^2}-\frac{\overline{A}}{r^2}\right)=-\overline{J}_s\,, \tag{1}$$

where $\overline{J}_s$ and $\overline{\overline{A}}$ are the source current density and the vector potential, respectively. Asymptotic boundary conditions were applied on the outer surface. From the vector potential $\overline{A}$ obtained by equation (1), the magnetic field intensity $\vec{H}$, the magnetic field gradients ($\partial\vec{H}/\partial r$ and $\partial\vec{H}/\partial z$) and the magnetic potential energy W were computed.

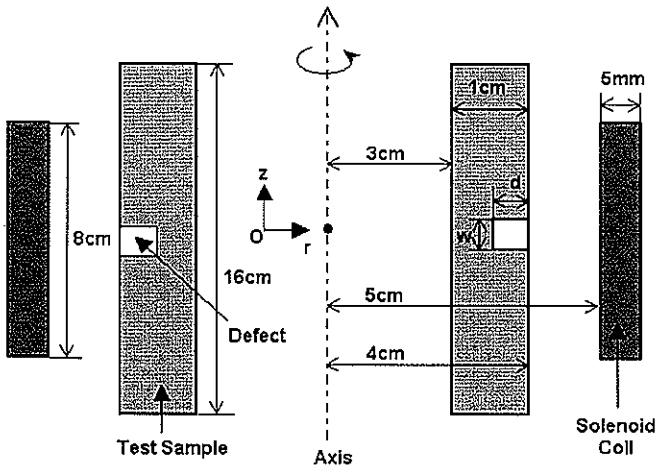

Fig. 1. The geometry of simulated test sample with axial symmetry: The defect sizes used in the calculation were depth (d) = 3, 5, 7, 9 (mm) and width (w) = 1, 2, 3, 5 (mm).

Magnetic Force on a Magnetic Particle

For magnetic particles to adhere to a defect, the magnetic force generated by an applied current source should be large enough to attract and maintain magnetic particles at the defect site. For a cylindrical coordinate system, the magnetic field vector $\vec{H}$ can be decomposed into the radial component, H_r and the component along the axial direction H_z. Magnetic force on a saturated magnetic particle can be described by the equations

$$\begin{aligned} F_r &= -K\left(H_r \frac{\partial H_r}{\partial r} + H_z \frac{\partial H_z}{\partial r} \right) \\ F_z &= -K\left(H_z \frac{\partial H_z}{\partial z} + H_r \frac{\partial H_r}{\partial z} \right) \end{aligned} \tag{2}$$

where K is a constant which contains information on the magnetic properties of the magnetic particle such as magnetic susceptibility and the volume of the magnetic particle. The quantities $A_r = F_r / K$ and $A_z = F_z / K$ are proportional to the magnetic force components.

For purposes of the calculation we assumed that magnetic particles are uniformly sprayed on the surface of the sample. The magnetic energy of a material with nonlinear permeability can be described by the equation

$$W = \int \left(\int_0^{\vec{H}} \vec{B}(\vec{h}) \cdot d\vec{h} \right) dV, \tag{3}$$

where $\vec{B}(\vec{h})$ represents the magnetic flux density as a function of arbitrary magnetic field $\vec{h}$, and $\vec{H}$ is the magnetic field in a small volume dV. For the calculation of energy at the i^{th} element of meshes, it is computed approximately as

$$\begin{aligned} W_i &= \left(\sum_{i=1}^{n_H} \vec{B}(\vec{h}_i) \cdot \Delta\vec{h}_i \right) V_i, \text{ such that} \\ \vec{h}_i &= \sum_{k=1}^{i} \Delta\vec{h}_k \text{ and } \vec{H} = \sum_{k=1}^{n_H} \Delta\vec{h}_k, \end{aligned} \tag{4}$$

where $\vec{H}$ and V_i are the magnetic field and volume of the i^{th} element, and the sum given in (4) is the approximate value of the integral in parentheses in equation (3). The $\vec{B}(\vec{H})$ curve is obtained from user-defined nonlinear permeability data. The radial component of magnetic force makes magnetic particles adhere to the defect site. With a volume V (caused by the radial component of magnetic force) and its susceptibility $\chi(H)$ at the magnetic field H, the radial component of the magnetic force acting on the magnetic particles is given by [6]:

$$\begin{aligned} \mathbf{F}_r &= -dW / dr = -\mu_0 \chi(|\vec{H}|) V \left(H_r \partial H_r / \partial r + H_z \partial H_z / \partial r \right) \\ &= \mu_0 \chi(|\vec{H}|) V A_r. \end{aligned} \tag{5}$$

For purposes of the calculation, it was assumed that the magnetic field intensity H and the susceptibility

$\chi(H)$ of magnetic particles are constant in the area of each finite element. This is of course an unrealistic assumption, but aids tractability of the equations. Therefore, from (5), the volume of magnetic particles in the i^{th} finite element retained inside the defect is given by

$$V_i = \frac{1}{\mu_0 \chi(|\vec{H}|)} \left(\frac{dW/dr}{-A_r} \right) \approx \frac{1}{\mu_0 \chi(|\vec{H}|)} \left(\frac{\Delta W}{\vec{H} \cdot \Delta \vec{H}} \right) \tag{6}$$

where $\Delta \vec{H}$ is the difference vector of $\vec{H}$ and ΔW is the difference scalar of W in the radial direction, respectively.

FEM algorithm for Magnetic Particle Inspection

If R_i be the radius of the center position of the i^{th} finite element in the defect, then the approximated volume of the i^{th} finite element is the product of $2\pi R_i$ and cross-sectional area A_i of the element. Note this is an axially symmetric problem. Therefore, the cross-sectional area of the magnetic particles at the i^{th} finite element from (6) is

$$A_i = \frac{1}{2\pi R_i \mu_0 \chi(|\vec{H}|)} \left(\frac{\Delta W}{\vec{H} \cdot \Delta \vec{H}} \right) \tag{7}$$

For the estimation of the magnetic particle volume at a defect site, the cross-sectional area given in (7) was calculated for each finite element at the defect site. If the cross-sectional area A_i of potential magnetic particle volume is smaller than the mesh area Δ_i, then the simulation algorithm is terminated, and the value of A_i is recorded into the data structure of the i^{th} element. The total sum of recorded areas ($\sum A_i$) provides the estimated volume of accumulated magnetic particles in the defect. If $A_j \geq \Delta_j$ for any finite element j, the magnetic particles fully occupy in the area of the finite element region.

The material properties of some finite elements were then changed and the solutions were recalculated. This simulation loop was repeated until the termination rule was satisfied. This FEM algorithm is a generic programming to update material properties of finite elements by an interaction between the magnetic particles and the updated magnetic field conditions (H, ΔH, and ΔW).

Sensitivity Analysis of FEM Simulations

Several sizes of defect geometry were simulated with a solenoid as a magnetic field source. Figure 2 shows the results of sensitivity analysis with various defect geometries using FEM. The volume of magnetic particles that attach to the defect increases as the depth of the defect increases when the size of defect width is fixed as shown in Fig. 2(a). The stack height of magnetic particles inside the defect site decreases as the width of the defect increases as shown in Fig. 2(b). The most important result is that MPI is more sensitive to sharper and deeper defects than to wider ones, and is not simply sensitive to the size of the flaws.

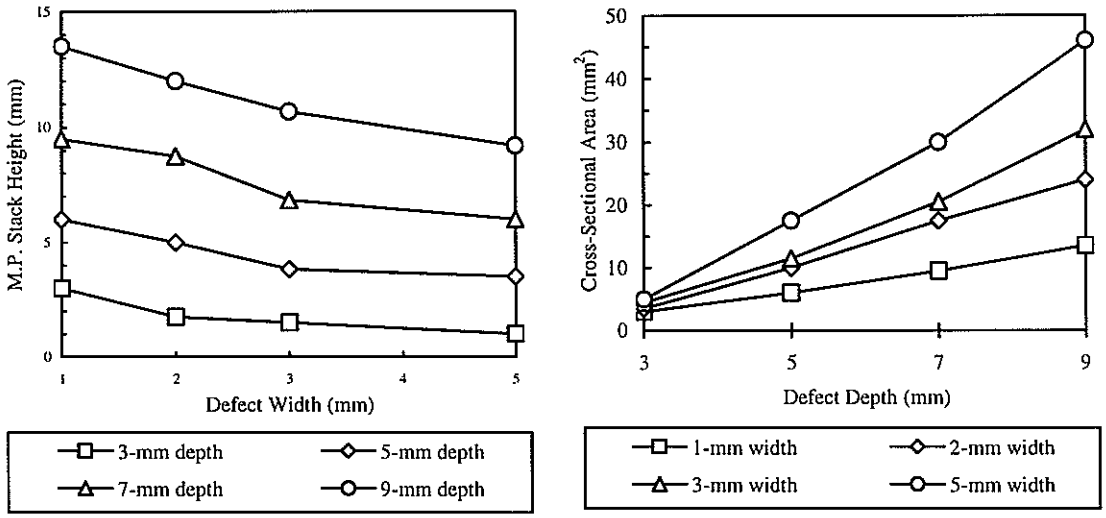

(a) (b)

Fig. 2. Sensitivity analysis showing accumulation of magnetic powder (the applied current density was 100kA/m^2). (a) varying defect depths. (b) varying defect widths.

Conclusion

Using the finite element method, the magnetic flux density, magnetic field gradient, and magnetic forces on magnetic powder particles due to magnetic flux leakage at the site of a defect, were calculated. These were used to determine optimum conditions for detection of different sizes and geometries of defects in materials using magnetic particle inspection.

Reduction of inspection design cost and time, and improvement of analysis of experimental data can be achieved by the use of FEM simulations combined with careful incorporation of model parameters such as magnetic field source, magnitude of the applied current, defect size, position of defect, and magnetic properties of both sample and magnetic particles.

REFERENCES

[1] R. Grimberg, A. Savin, E. Radu, and S. M. Chifan, "Eddy current sensor for holographic visualization of material discontinuities," *Sens. Actuators A,* vol. 81, pp. 251-253, Jan. 2000.

[2] D. L. Atherton, "Stress-shadow magnetic inspection technique for far-side anomalies in steel pipe," *NDT International*, vol. 16, pp. 145-149, Jun. 1983.

[3] O. Sundström and K. Törrönen, "The use of Barkhausen noise analysis in nondestructive testing," *Mater. Eval.*, vol. 37. No. 3, pp. 51-56, Mar. 1979.

[4] D. Lovejoy, Magnetic Particle Inspection, London: Chapman & Hall, 1993.

[5] Z. Zeng, L. Xuan, L. Upda, and S. Upda, "Modeling of current excitation waveforms for magnetic particle inspection," *QNDE*, D. O. Thompson, Ed., Plenum, New York, vol. 615, pp. 1984-1990, May 2002.

[6] D. C. Jiles, *Magnetism and Magnetic Materials, 2nd ed.*, New York, NY: Chapman & Hall, 1998.

DEVELOPMENT OF MODELING AND SIMULATION FOR MAGNETIC PARTICLE INSPECTION USING FINITE ELEMENTS

J. Y. Lee, S. J. Lee, D. C. Jiles, M. Garton, R. Lopez, and L. Brasche
Center for Aviation Systems Reliability, Iowa State University, Ames, Iowa 50011

ABSTRACT Magnetic particle inspection (MPI) is a widely used inspection method for aerospace applications with inspection development essentially limited to empirical knowledge and experience-based approaches. Better quantitative understanding of the MPI technique and factors that affect its sensitivity and reliability would contribute not only to reductions in inspection design cost and time but also improvement of analysis of experimental data. We employed a finite element method (FEM) for numerical calculation because this is known to be suitable for complicated geometric objects such as the part shapes encountered in aviation components and defects of concern. Magnetic particles are usually soft magnetic materials and sensitive to the magnetic field distribution around them. They are easily attracted toward a high magnetic field gradient. Selection of magnetic field source, which produces a magnetic field gradient large enough to detect a small defect in the sample, is an important factor in magnetic particle inspection. The magnetic field gradient and magnetic force at the sites of defects having different widths and depths have been calculated. The simulated results can be used to assist in understanding the behavior of magnetic particles around a defect.

INTRODUCTION

A number of nondestructive evaluation (NDE) techniques have been developed for evaluating defects; surface discontinuities, voids, surface flaws, and cracks on the surface or in the body of materials [1-8]. Properly applied NDE techniques will prevent operational failures of the mechanical parts by locating critical defects. Metallic materials are widely evaluated in NDE applications due to their common usage in industry. Different NDE techniques should be used depending on whether the metallic materials are magnetic or non-magnetic. For magnetic metallic materials such as steel, eddy current [1,2], magnetic flux leakage [3,4], magnetic Barkhausen noise [5,6], and magnetic particle inspection [7,8] techniques can be employed. Among these techniques, the magnetic particle inspection (MPI) and the magnetic flux leakage (MFL) are popular due to their inexpensive and simple procedures. Both techniques depend on the distortion of magnetic flux lines caused by a defect on the surface or sub-surface of a ferromagnetic material. The difference between the techniques is the method of detecting defects. The MPI technique uses fine magnetic particles, dry iron powder or wet magnetic particles suspended in a liquid medium, to identify the defect while the MFL technique employs a magnetometer to measure the magnetic leakage field occurring around the defect. Easy distribution of magnetic particles on a test sample makes the MPI technique suitable for samples with large surface areas while the MFL technique may be appropriate for detecting defects in the areas where access would be difficult for visualization such as inside surfaces of pipelines.

The magnetic field generator and the magnetic particles are essential components of the MPI method. The magnetic field strength should be large enough to magnetize the sample so that the magnetic particles can interact with the leakage fields. The magnetic force, which drags the magnetic particles to the defect sites, is proportional to the product of the magnetic field and the magnetic field gradient. The distortion of the magnetic field is greatest when the direction of the magnetic field is perpendicular to the axis of a defect, which maximizes the magnitude of the magnetic field gradient. Magnetic fields can be generated either by a direct contact of current source to the test material using prods (not recommended for aerospace components) or by using current coils such as a solenoid or a yoke. The magnetic properties of the magnetic particles are a very important factor in MPI testing. A simple analytical model for the calculation of the magnetic leakage field of surface-breaking cracks and an estimation of the magnetic force on the magnetic particle were studied with an assumption of constant permeability [9]. Computational advances enabled the numerical simulations of MPI for a complicated geometry [10]. In this paper we report the use of the finite element method (FEM) numerical simulations of MPI for defects with various sizes. The simulated results can provide indications of the expected behavior of magnetic particles around a defect.

FINITE ELEMENT NUMERICAL SIMULATIONS

Equations for an Axisymmetric Geometry

We simulated a test sample in the shape of a cylindrical tube by solving Maxwell's equations in a cylindrical coordinate system (r, θ, z). For axisymmetric geometry, the Maxwell's equation for Ampére's law under DC mode is as follows:

$$\frac{1}{\mu}\left(\frac{\partial^2 \overline{A}}{\partial r^2}+\frac{1}{r}\frac{\partial \overline{A}}{\partial r}+\frac{\partial^2 \overline{A}}{\partial z^2}-\frac{\overline{A}}{r^2}\right)=-\overline{J}_S \tag{1}$$

where $\overline{J}_S$ and $\overline{A}$ are the source current density and the vector potential respectively. Asymptotic boundary conditions are applied on the outer surface of the domain. Using the Ritz method one can show that the solution of the Maxwell Equation (1) is equivalent to minimizing the energy function described as [11]:

$$F=\iint_R\left\{\frac{1}{2\mu}\left(\left|\frac{\partial \overline{A}}{\partial z}\right|^2+\left|\frac{\partial \overline{A}}{\partial r}+\frac{\overline{A}}{r}\right|^2\right)-\overline{J}_s\cdot\overline{A}\right\}rdrdz\ . \tag{2}$$

Using the vector potential $\overline{A}$ obtained from Equation (2), the magnetic flux density B, the magnetic field intensity H, the magnetic field gradient dB/dr, and the magnetic potential energy W were computed.

Simulation of Magnetic Flux Leakage Field

For the simulation of a sample using the finite element method (FEM), we modeled a test for investigating the behavior of magnetic particles when a solenoidal current field is applied. The test sample was assumed to be cylindrical in shape and the shape of the defect on the surface in the form of a groove. The cross section of the cylindrical sample and the defect is shown in Figure 1.

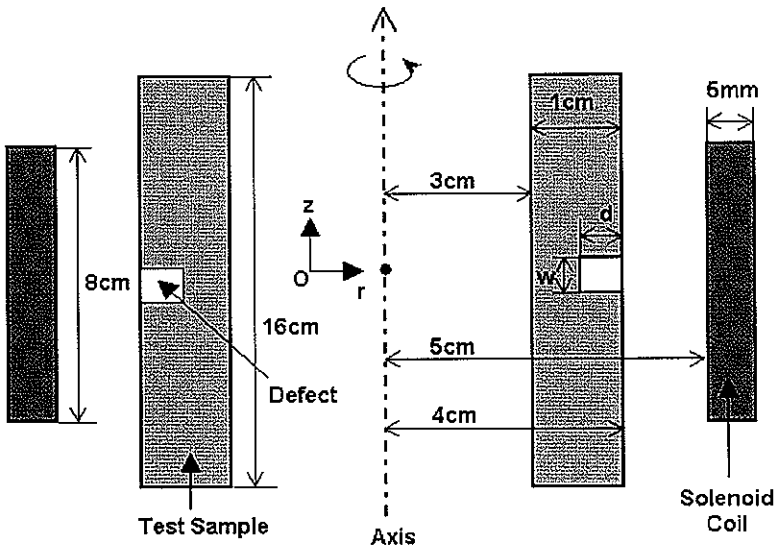

FIGURE 1. The geometry of simulated test sample with axial symmetry: The defect sizes used in the calculation were depth (d) = 1, 3, 5, 7, 9 (mm) and width (w) = 1, 3, 5 (mm).

The length and wall thickness of the sample were chosen to be 16 cm and 1 cm, respectively. The defect is located at the center of the sample. The defect size was varied during the batch of simulation tests. The distance between the outer boundary and the test sample was set to be sufficiently large to satisfy boundary conditions. Asymptotic boundary conditions were applied to the outer surface. The B-H curve of the test sample showed a nonlinear behavior as shown in Figure 2. The magnetic force that attracts magnetic particles is proportional to the magnitude of the magnetic field gradient [12]. Therefore, the distribution of the magnetic field gradient around a defect is an important factor in magnetic particle inspection. The magnetic field gradient versus depth (*d* in Figure 1) and width (*w* in Figure 1) are shown in Figure 3.

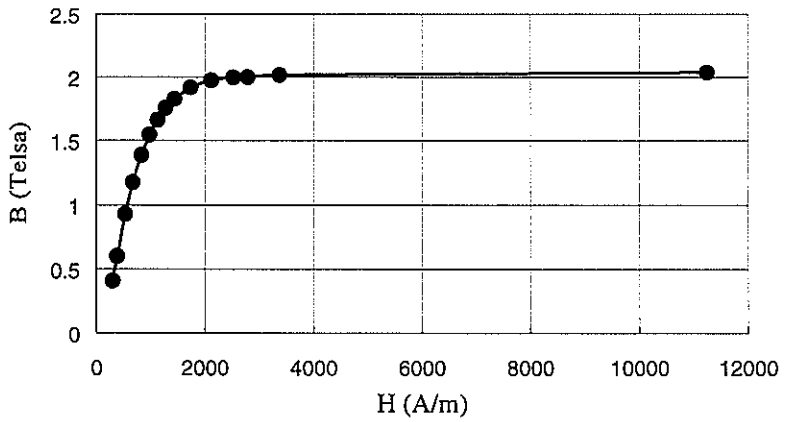

FIGURE 2. The B-H curve of the testing sample.

In the absence of defects the calculations suggested that the magnetic flux density B under a solenoidal current field increases linearly as a probe moves from the center of the z-axis to the outside of the cylinder. However, the change of B-field along the radial direction (dB / dr) is higher at the center of the defect than outside of the defect. This result is crucial for the magnetic flux leakage (MFL) test. According to our calculations, as the depth of the defect increases as shown in Figure 3(a), the magnitude of the magnetic field gradient should increase. The peak-to-peak value of magnetic field gradient decreased as the width of the defect increased as shown in Figure 3(b). This implies that the magnetic force should become weaker as the defect becomes wider.

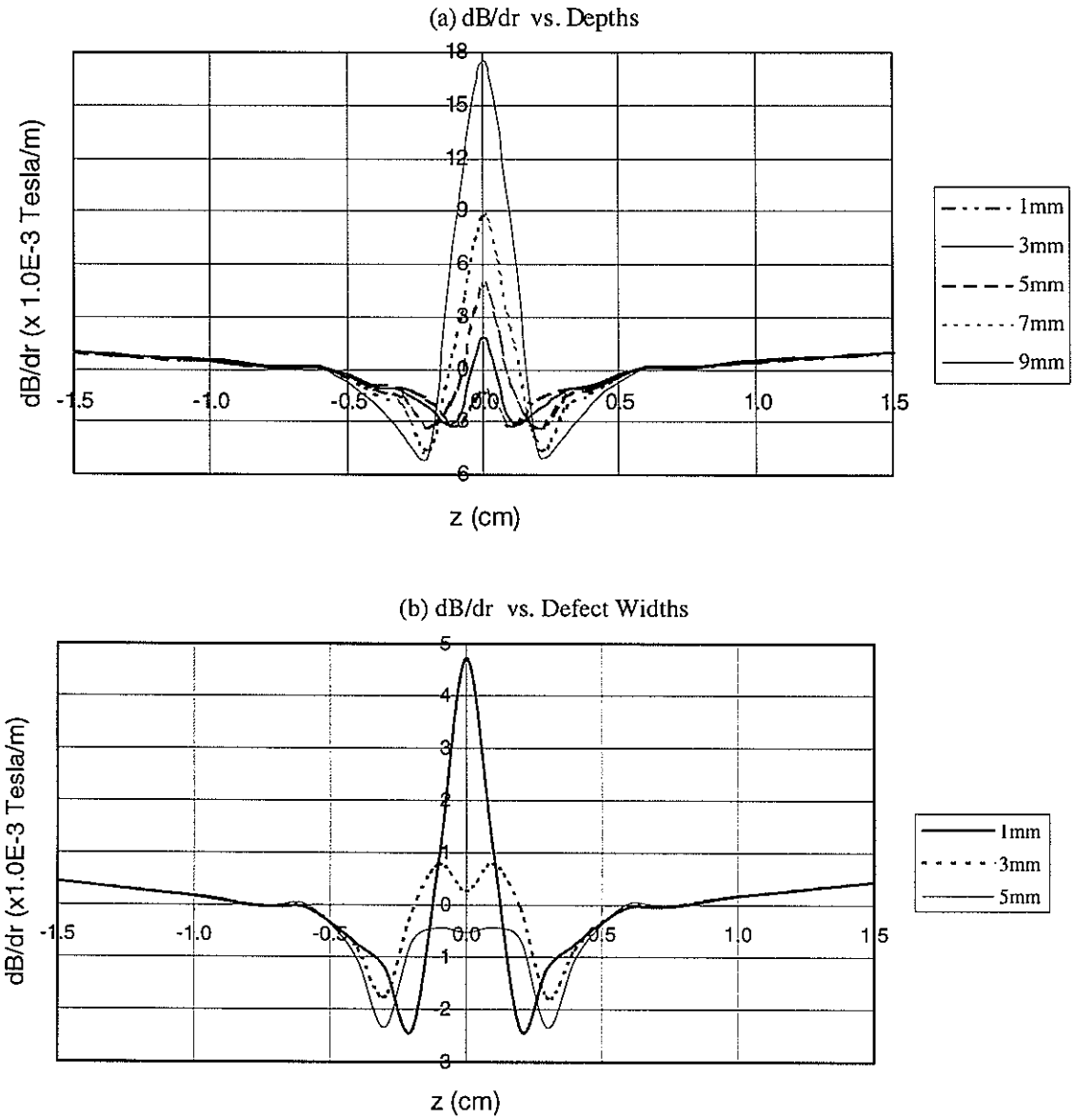

FIGURE 3. Simulation of magnetic field gradient (dB/dr); (a) dB/dr vs. defect depths (defect width=1mm, current density=2.0A/mm^2), (b) dB/dr vs. defect widths (defect depth=5mm, current density=1.0A/mm^2).

Magnetic Force on a Magnetic Particle

For magnetic particles to adhere to a defect, the magnetic force generated by an applied current source should be large enough to drag magnetic particles into the defect. Magnetic force on a saturated magnetic particle can be described by the equation

$$F_m \propto -\vec{\nabla}\left(\vec{H}\cdot\vec{M}\right) = -K\vec{\nabla}\left(\vec{H}\cdot\vec{H}\right) \tag{3}$$

where $\vec{M}$ is the magnetization vector of the magnetic particle, and K is a constant which contains information of the magnetic property of the magnetic particle such as magnetic susceptibility and the volume of the magnetic particle.

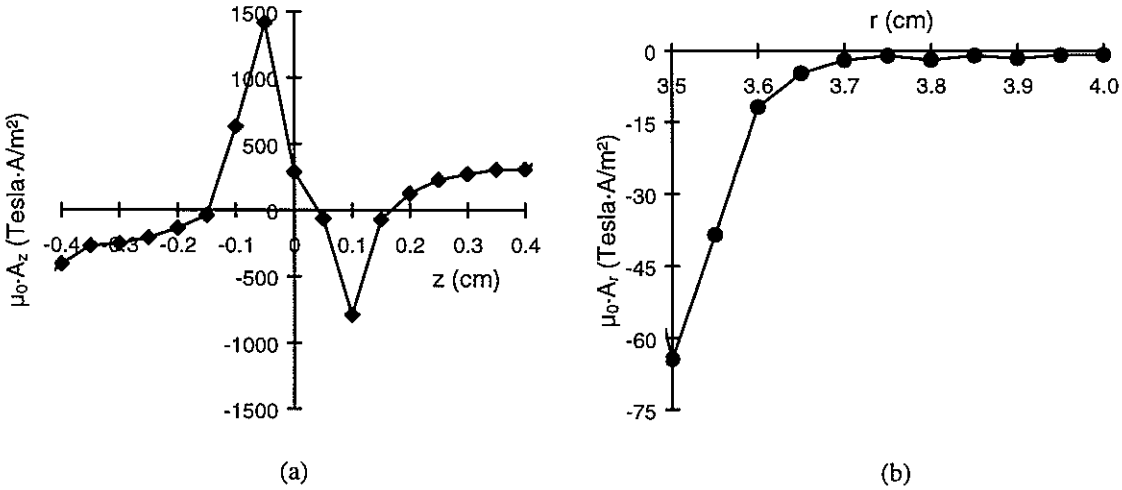

FIGURE 4. Proportional quantities to magnetic force component (a) along z direction and (b) along radial direction.

For the cylindrical coordinate system, the magnetic field vector $\vec{H}$ can be decomposed into the radial component, H_r and the component along the z direction H_z. From Equation (3), the magnetic force components along the r- and z- directions can be written as:

$$\begin{aligned} F_r &= -K'\left(H_r\frac{\partial H_r}{\partial r} + H_z\frac{\partial H_z}{\partial r}\right) \\ F_z &= -K'\left(H_z\frac{\partial H_z}{\partial z} + H_r\frac{\partial H_r}{\partial z}\right) \end{aligned} \tag{4}$$

where $K'=2K$. The quantities $A_r = F_r / K'$ and $A_z = F_z / K'$, which are proportional to the magnetic force components, can provide some information on the behavior of a magnetic particle around a defect.

The values of A_z and A_r are plotted in Figure 4. The geometry of the sample for this simulation was the same as shown in Figure 1. The size of a defect was assigned as 1-mm width and 5-mm depth. The applied current density is 2×10^{-6}A/m^2. Figure 4(a) shows that the magnetic leakage field from the defect induces a magnetic force that

makes the magnetic particle around the defect region move to the center of the defect. If there is no defect in the test material, the magnetic field from the solenoid coil will make the magnetic particle pull out of the center position of the z-axis. Figure 4(b) shows that the quantity proportional to the radial component of magnetic force increases as the magnetic particle moves toward the bottom of the defect. It suggests how the magnetic force attracts and retains magnetic particles at the defect against their weight.

FEM algorithm for Magnetic Particle Inspection

The next step is the description of physical behavior of the magnetic particles at the defect. We assume that the magnetic particles are uniformly sprayed on the surface of a sample. The magnetic energy of a material with nonlinear permeability can be described as

$$W = \iint \left(\int_0^H B(h)dh \right) dV, \tag{5}$$

where $B(h)$ represents the magnetic flux density as a function of magnetic field h, and H is the magnetic field in a small volume dV. For the calculation of energy at the i^{th} element of meshes, it is computed approximately as

$$W_i = \left(\sum_{i=1}^{n_H} B(h_i)\Delta h_i \right) V_i, \text{ such that } h_i = \sum_{k=1}^{i} \Delta h_k \text{ and } H = \sum_{k=1}^{n_H} \Delta h_k, \tag{6}$$

where H and V_i are the magnetic field and volume of the i^{th} element, and the sum given in Equation (6) is the approximate value of the integral in the parenthesis of the Equation (5). The $B(H)$ curve is obtained from the user-defined nonlinear permeability data. The magnetic force on the magnetic particles with a volume V and a susceptibility $\chi(H)$ at magnetic field of H, is given by [12]:

$$F_r = -dW/dr = -\mu_0 \chi(H) V \left(H_r dH_r/dr + H_z dH_z/dr \right) = \mu_0 \chi(H) V \cdot A_r. \tag{7}$$

Figure 5 shows a simulation result of magnetic potential energy and the corresponding magnetic force. The light bars in Figure 5(b) represent the magnetic forces at the bottom surface of defect holes and the dark bars in Figure 5(b) show the forces at 1 mm above the flaw bottoms. The solid lines are the logarithmic interpolation curves of magnetic energy and forces, respectively. The magnetic forces are proportional to the magnetic potential energy as shown in Figure 5.

We assumed that the magnetic field intensity H and the susceptibility $\chi(H)$ of magnetic particles are constant in the area of each finite element. Therefore, from Equation (7), the volume of magnetic particles in the i^{th} finite element retained inside the defect is given by

$$V_i = \frac{1}{\mu_0 \chi(H)} \left(\frac{dW/dr}{-A_r} \right) \approx \frac{1}{\mu_0 \chi(H)} \left(\frac{\Delta W}{H_r \Delta H_r + H_z \Delta H_z} \right) \equiv \frac{1}{\mu_0 \chi(H)} \cdot \frac{\Delta W}{\vec{H} \cdot \Delta \vec{H}}. \tag{8}$$

Let R_i be the radius of the center position of the i^{th} finite element in the defect. Then, the approximated volume of the i^{th} finite element is the product of $2\pi R_i$ and the cross-sectional area A_i of the element. Note this is an axially symmetric problem. It is assumed that the wet magnetic particles are uniformly distributed on the surface of the test material. Therefore, the magnetic particles are uniformly accumulated inside the defect region. From Equation (8), the cross-sectional area of the magnetic particles at the i^{th} finite element is

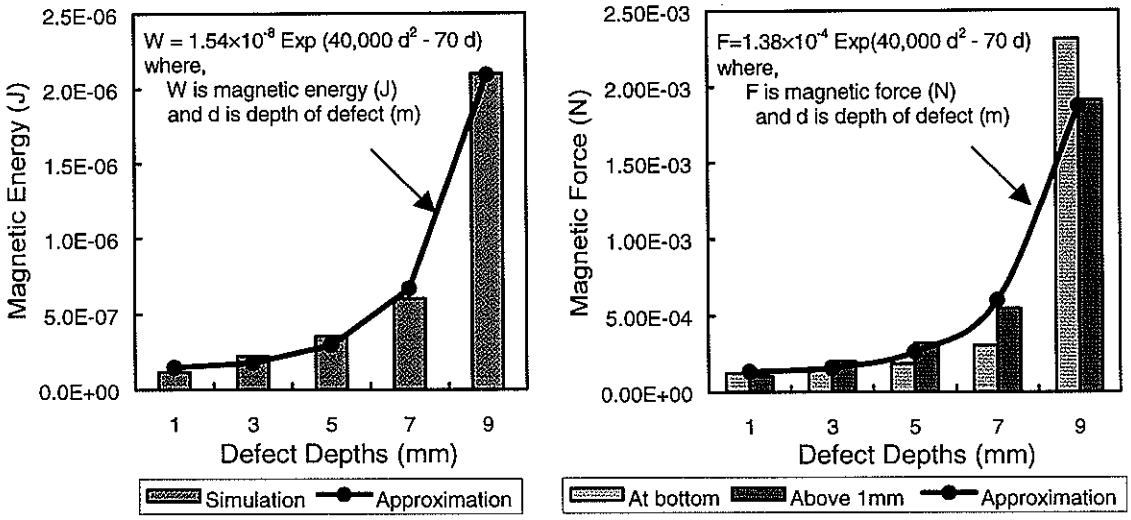

(a) (b)

FIGURE 5. Simulation of Magnetic Particle Inspection; (a) magnetic potential energy at the bottom of defect and (b) magnetic force around the bottom of defect.

$$A_i = \frac{1}{2\pi R_i \mu_0 \chi(H)} \cdot \frac{\Delta W}{\vec{H} \cdot \Delta \vec{H}}. \tag{9}$$

For the estimation of the magnetic particle volume in the defect region, the cross-sectional area given by Equation (9) was calculated for each finite element in the defect region. If each of the cross-sectional areas obtained from Equation (9) is smaller than the area of the corresponding finite element, then the value of the cross-sectional area of the retained magnetic particles (A_i) is recorded to the database of the finite element. At this step the simulation loop is terminated. The total sum of the recorded areas ($\sum A_i$) of magnetic particles in the finite elements around a defect indicates the estimated volume of accumulated magnetic particles in the defect.

If any of the areas of the retained magnetic particles is larger than or equal to the area of the corresponding finite element, then the material property of this finite element is changed from air to magnetic particles. That is, the magnetic particles are fully occupied in the area of the finite element region. The next step is rebuilding and solving a new MPI problem given by Equation (2). This simulation loop is continued until the termination rule is satisfied. This is a generic algorithm to update material properties of finite elements by an interaction between the magnetic particles and the updated magnetic field conditions (H, ΔH, and ΔW).

Table 1 shows that the volume of the magnetic particles increases proportionally as the depth of the defect increases when the size of defect width is fixed. For the sensitivity analysis of defect width, the defect geometry was set at a fixed depth of 5-mm and variable widths of 1 mm, 3 mm, and 5 mm. The stack heights of magnetic particles inside defects were 1.175 mm, 0.748 mm, and 0.648 mm, respectively. Therefore, the height of the stack of particles inside the defect proportionally decreased as the width of defect increased.

TABLE 1. Simulation Results of FEM algorithm for MPI.

Defect Geometry (Depth x Width)	Cross-Section Area of Magnetic Particles inside Defect†				
	Sim.‡ Loop 1	Sim. Loop 2	Sim. Loop 3	Sim. Loop 4	Sim. Loop 5
1 mm x 1 mm	0.194 mm^2	N/A	N/A	N/A	N/A
3 mm x 1 mm	0.416 mm^2	N/A	N/A	N/A	N/A
5 mm x 1 mm	1.000 mm^2	1.175 mm^2	N/A	N/A	N/A
7 mm x 1 mm	1.000 mm^2	2.000 mm^2	3.000 mm^2	3.208 mm^2	N/A
9 mm x 1 mm	1.000 mm^2	2.000 mm^2	3.000 mm^2	4.000 mm^2	4.936 mm^2
5 mm x 3 mm	2.243 mm^2	N/A	N/A	N/A	N/A
5 mm x 5 mm	3.239 mm^2	N/A	N/A	N/A	N/A

† The current field is fixed at $2.0\times10^{+6}$ A/m^2.

‡ "Sim." means simulation.

CONCLUSIONS

Using the finite element method, the magnetic flux density, the magnetic field gradient, and the magnetic force on magnetic powder particles at the site of a defect were calculated. The calculation showed that the magnetic flux leakage field at the defect created a magnetic force, which attracted and retained the magnetic particles at the defect location. The magnetic particle inspection technique is more sensitive to the defect geometry than the magnetic flux leakage measurement technique, from which method it is difficult to predict the geometry of a defect. Reduction of the inspection design cost, time, and improvement of analysis of experimental data can be achieved by the use of FEM simulations combined with careful incorporation of MPI parameters such as magnetic field source, magnitude of the applied current, defect size, position of defect, and magnetic properties of both sample and magnetic particles.

ACKNOWLEDGEMENTS

This research was supported by the Federal Aviation Administration under Contract #DTFA03-98-D-00008, Delivery Order #IA051 and performed at Iowa State University's Center for NDE as part of the Center for Aviation Systems Reliability program.

REFERENCES

[1] Clark, W. G. and Junker, W. R., "Problems in the eddy current characterization of temper embrittlement," *Mater. Eval.* 43, 1985, pp. 1546-1552

[2] Grimberg, R., Savin, A., Radu, E., and Chifan, S.M., "Eddy current sensor for holographic visualization of material discontinuities," *Sens. Actuators A*, 81, 2000, pp. 251-253.

[3] Hastings, C. H., "Recording magnetic detector locates flaws in ferrous metals," *Product Eng.*, 18(4), 1947, pp. 110-112.

[4] Atherton, D. L., "Stress-shadow magnetic inspection technique for far-side anomalies in steel pipe," *NDT International* 16(3), 1983, p. 145.

[5] Tiitto, S., "On the influence of microstructure on magnetization transitions in steel," *Acta Polytechnica Scand. in Appl. Phys. Ser.*, 119, 1977, p. 80.

[6] Sundström, O. and Törrönen, K., "The use of Barkhausen noise analysis in nondestructive testing," *Mater. Eval.* 37(3), 1979, pp. 51-56.

[7] Betz, C. E., *Principles of Magnetic Particle Testing*, Magnaflux Corporation, Hardwood Heights, Illinois, 1997.

[8] Lovejoy, D., *Magnetic Particle Inspection: A Practical Guide*, Chapman & Hall, London, 1993.

[9] Edwards, C. and Palmer, S. B., "The magnetic leakage field of surface-breaking cracks," *J. Phys. D: Appl. Phys.* 19, 1986, pp. 657-673.

[10] Zeng, Z., Xuan, L., Upda, L., and Upda, S., "Modeling of current excitation waveforms for magnetic particle inspection," *QNDE*, edited by D. O. Thompson, Plenum, New York, 21B, 2002, pp. 1984-1990.

[11] Palanisamy, R., *Finite Element Modeling of Eddy Current Nondestructive Testing Phenomena,* Ph.D. Thesis, Colorado State University, 1980.

[12] Jiles, D. C., *Magnetism and Magnetic Materials, 2nd Ed.*, Chapman & Hall, New York, 1998.

ACKNOWLEDGMENTS

I wish to express sincere appreciation to Professor David Jiles. Also I wish to thank to Dr. Satish Udpa and Dr. Lalita Udpa, who sincerely supported me for such a long time until I accomplish my works. Thanks also to the members of the school council for their valuable input. Also I specially thank to Dr. Seong-Jae Lee who supported and helped me for my works like his ones.

Personally I thank my wife, Minkyoung Song, and my daughter, Lucia, for believing me without any doubt or complaint, so that I could keep studying my own research. I also wish to appreciate our parents' belief in my long abroad studies. I always have a lot of debts for my family and friends. According to the oriental philosophy, parents, teachers, and lords are identical.

In my memory, there were a lot of sincere friends at Iowa State University, and they are all going on the way of their success. I wish that those whom I knew here at Iowa State University will be happier and happier every day.

These works were supported in part by the Federal Aviation Administration under Contract #DTFA03-98-D-00008, Delivery Order #IA051 at Iowa State University's Center for NDE as part of the Center for Aviation Systems Reliability. I also thank to Mike Garton, Rick Lopez, and Lisa Brasche who are working with me at the Center for Aviation Systems Reliability, Iowa State University, Ames, Iowa 50011.

This work was performed at Ames Laboratory under Contract No. W-7405-Eng-82 with the U.S. Department of Energy. The United States government has assigned the DOE Report number IS-T 2337 to this thesis.